Spring 1-1-2012

Impact of Tropical Cyclones on the Ocean Heat Budget and Upper Ocean Dynamics in the Bay of Bengal during 1999

Jih-Wang Wang
University of Colorado at Boulder, jihwang@colorado.edu

Impact of Tropical Cyclones on the Ocean Heat Budget and Upper Ocean Dynamics in the Bay of Bengal during 1999

by

Jih-Wang (Aaron) Wang

B.S., National Taiwan University, 2000

M.S., Colorado State University, 2005

A thesis submitted to the

Faculty of the Graduate School of the

University of Colorado in partial fulfillment

of the requirements for the degree of

Doctor of Philosophy

Department of Atmospheric and Oceanic Sciences

2012

This thesis entitled:
Impact of Tropical Cyclones on the Ocean Heat Budget and Upper Ocean Dynamics in the Bay of Bengal during 1999
written by Jih-Wang (Aaron) Wang
has been approved for the Department of Atmospheric and Oceanic Sciences

_____

Dr. Weiqing Han

_____

Dr. Jeffrey Weiss

Date_____

The final copy of this thesis has been examined by the signatories, and we find that both the content and the form meet acceptable presentation standards of scholarly work in the above mentioned discipline.

Wang, Jih-Wang (Ph.D., Atmospheric and Oceanic Sciences)

Impact of Tropical Cyclones on the Ocean Heat Budget and Upper Ocean Dynamics in the Bay of Bengal during 1999

Thesis directed by Associate Professor Weiqing Han

The impacts of two consecutive, strong tropical cyclones (TCs) – 04B (10/15-10/19) and 05B (10/25-11/3) in 1999 (hereafter, TC1 and TC2) – on the Bay of Bengal (BoB) heat budget and upper ocean dynamics are examined using the Hybrid Coordinate Ocean Model. A series of diagnostic experiments are conducted to isolate the model's response to the individual TC-associated forcings by comparing their model results.

During the TCs, the BoB ocean heat content (OHC) is reduced, primarily due to TC-wind induced southward ocean heat transport (OHT) and a reduction in surface downward radiation due to increased cloudiness. BoB OHC is largely restored in the following months via enhanced surface heat fluxes, associated with cold wake restoration, and positive northward OHT. The TCs' downward heat pumping effect is estimated to be ~1.74×10^{18}J near the end of February 2000, which is less than estimates using previously published methods based on surface observations. The relatively weak heat pumping results from freshwater input by intense monsoon rainfall and river discharge in the BoB, which stabilizes stratification, forms a barrier layer, and generates temperature inversions during seasonal surface cooling. As a result, early stage TC winds entrain the warm barrier layer water and enhance enthalpy loss in the southeastern Bay, while mature stage TC winds erode the barrier layer, decrease SST through upwelling and entrainment of deeper cold water and reduce enthalpy loss in the northwestern Bay. Our findings suggest TC winds may significantly alter the interseasonal BoB heat budget

through OHT and surface heat fluxes.

Background southwesterly and TC winds produce positive sea surface height anomalies (SSHAs) along the northern and eastern BoB boundary via Ekman transport and direct seawater pile-up, and produce negative SSHAs along the TC tracks with rightward bias via Ekman divergence and surface cooling. The wind-induced turbulent mixing and upwelling are the primary causes for surface cooling, and the latter does not induce downward heat pumping. The oscillations of top layer currents and temperatures on the right of the TC tracks have period near inertial oscillation (~1.5 days), and the near-inertial currents have strong influence on horizontal temperature advection.

Dedication

To my wife, Yushiuan Chen, whom I can never thank enough.

Acknowledgements

My life endured significant changes since I met my wife, Yushiuan Chen. She brought faith to my life and re-shaped my way of thinking. Without her, I probably would have floated with the currents and got drifted away. Her encouragement and company were the main reason why I could persist to the last. I can not thank enough for her support. Yushiuan's family, especially her parents and grandmother, always provide very useful advice and sincere care, and I'd also like to thank them.

I am very lucky to have benefited from the guidance of my advisor, Dr. Weiqing Han. Her generosity, patience, and honesty all helped me to face the difficulties in the past four years. Our discussions planted my feet on the solid ground of science. Acknowledgement also goes to the members of my thesis committee: Dr. Jeffrey Weiss, Dr. Gerald Meehl, Dr. Robert Leben, Dr. William Emery, and Dr. Rajagopalan Balaji. They have always been willing to share their thoughts and experiences, and their questions improved my work. Fellow members of Dr. Han's research group, Laurie Trenary, Benet Duncan, Richard Bateman, and Jian Zheng, have provided their precious feedback to my work, and my research benefited from the discussions with them.

My family continues to support me unconditionally, encourage me, and offer me a worry-free environment. I appreciate them more than I can ever fully express.

Funding for this work was provided by NSF CAREER award 0847605, NASA OSTST award NNX08AR62G, and NOAA NA11OAR4310100. I also thank CISL of NCAR for computer resources and technical support, Dr. Luc Bujold for buoy and cruise observation data, Dr. Allan Wallcraft for HYCOM consultation, ECMWF and NCAR for the ERA-Interim fields, CCMP team for satellite-observed winds, and TRMM team for the precipitation data.

Contents

Chapter

1 Introduction 1

1.1 Background.....1

1.2 TC Impacts on Ocean Heat Pumping and Heat Transport.....3

1.3 Impacts of Tropical Cyclones (TCs) in the Indian Ocean.....6

1.4 Present research about the TC effects on the BoB heat budget.....8

2 Description of Cyclone Cases, Ocean Model and Experiments 12

2.1 Description of the TCs.....12

2.2 The HYbrid Coordinate Ocean Model (HYCOM) and Forcing Fields.....13

2.2.1 Indian Ocean Configuration.....14

2.2.2 Surface and lateral boundary forcing fields.....16

2.2.2.1 The ERA-Interim (ERAI) fields.....16

2.2.2.2 TRMM precipitation.....18

2.2.2.3 CCMP Wind.....18

2.2.2.4 Lateral boundary forcing: Bay of Bengal River Discharge 19

2.3 Reconstructed TC Winds.....20

2.4 Experiment Design and TC Signal Removal.....22

2.4.1 Experiment Design.....22

2.4.2 TC Signal Removal.....25

2.5 Processes that Affect the BoB OHC.....27

2.6 Summary.....30

3 Model/Data Comparisons 32

3.1 Sea Surface Temperature…….....32

3.2 Sea Surface Height…….35

3.3 Drifting Buoys and Cruise Profiles……....37

3.4 Summary and Discussion…….....40

4 Impacts of the Orissa TCs on the BoB heat budget: Processes 42

4.1 Impacts of TCs on the BoB OHC Budget: Relative Importance of Wind, Precipitation and Radiation Forcing…….....42

4.1.1 Seasonal cycle of BoB OHC……..42

4.1.2 TC-induced OHC change……...43

4.1.3 Contribution of TC-induced OHT to OHC……45

4.1.4 Contribution of TC-induced NetHF to OHC…….46

4.2 Estimated DOHP based on SST before/after the TCs….....53

4.3 Penetration of TCs' Impacts in the Upper Ocean……..…55

4.4 Impacts of TCs on Ocean Heat Potential……...61

4.5 Summary and Discussion……...……63

5 Upper Ocean Dynamical Response to TC Forcings 67

5.1 Impacts of TC1……..67

5.1.1 Upper ocean dynamical response and processes……...67

5.1.2 Northwestern BoB Cooling: Processes……..71

5.1.3 Effects Inertial Oscillation on Upper Ocean Temperature…….77

5.2 Impacts of TC2….....79

5.2.1 Upper ocean dynamical response……...79

5.2.2 Northwestern BoB Cooling: Processes……..83

5.2.3 Effects of Inertial Oscillation on Upper Ocean Temperature….87

5.2.4 Coastal Kelvin Waves and Rossby Waves…….90

5.3 Summary and Discussion…….....92

6 Summary and Future Work 95

6.1 Summary…….....95

6.1.1 Background and Research Question – Downward Ocean Heat Pumping and Climate……..……...95

6.1.2 Experiment Design and Model Results……..95

6.1.3 Processes and Interpretations…….97

6.1.4 Upper Ocean Dynamical Response…….100

6.2 Future Work….....101

6.2.1 Rationale……..102

6.2.2 Objectives……103

6.2.3 Research Plan……...103

6.2.4 Expected Outcomes and impacts…….106

Bibliography 108

Tables

Table

2.1 The largest three rivers in the model domain based on Dai *et al.* [2009]……..……20

2.2 The suite of HYCOM experiments performed for assessing the TCs' impacts. The abbreviation "WIND" stands for wind speed and wind stress, "RAIN" for rain rate, "RAD" for radiation, "WSTR" for wind stress, "WSPD" for wind speed, "No" for filtered, and "Rc" for reconstructed. See text for detailed description of each experiment……..……..23

4.1 The TC effects on oceanic heat convergence (see text) using the method of Sriver and Huber [2007] and Sriver *et al.* [2008] and the data from NCEP, TMI, and HYCOM……...54

Figures

Figure

1.1 Northward OHT for the Atlantic Ocean (top and middle) and the World Ocean (bottom). Three types of OHT are plotted: 1) derived northward OHT estimates based on atmospheric reanalyses from the National Centers for Environmental Prediction and National Center for Atmospheric Research (NCEP/NCAR; red) and the European Centre for Medium-Range Weather Forecasts (ECMWF; blue), 2) simulated northward OHT from the coupled models – the NCAR Community Climate System Model (CCSM; black curves) and the Hadley Centre Climate Model 3 (HADCM3; green), and 3) direct northward OHT observations (black symbols with error bars). The dashed curves represent the ±1 standard error for the derived OHT. Image taken from Trenberth and Caron [2001]……....3

1.2 Schematic diagram showing the three stages of DOHP by TCs. Stage (a) shows the upper ocean temperature homogenization, which lowers the ML temperature and raises the temperature of the upper thermocline layer, Stage (b) shows restoration of the ML temperature via enhanced downward surface heat flux and advection, and Stage (c) shows that the additional heat in the upper thermocline layer is carried away by lateral advection. In Stage (a), the warm anomaly in the upper thermocline layer (striped) compensates the cold anomaly in the ML (dotted), and thus there is no net column heating in this stage. Image taken from Emanuel [2001]……..5

2.1 The three-day mean TRMM 3B42 rain rate (top panels), the three-day mean ERAI rain rate (middle panels), and maximum sustainable wind (MSW) speed and translation speed (bottom panels) for the two TC cases. For TC1, the rain rate averaging period is 10/15-10/17, while for TC2, 10/27-10/29. The black lines are the cyclone tracks from IBTrACs (top panels) and determined from ERAI lowest mean sea level pressure (middle panels), while the crosses are the cyclone centers every six hours during the three-day period. Missing values and zero precipitation in TRMM data are shown as white background. Note that TC1 center from ERAI at 10/15 00Z is ambiguous……..……14

2.2 Topography map of the domain for the HYCOM experiments. South China Sea is masked out as land, while the temperature and salinity of the remaining eastern boundary along 120° E and southern boundary along 35°S is relaxed to monthly ocean objective analysis product from the Meteorology Office of the UK……15

2.3 Wind speed (contours; 5 m/s interval) and wind velocity (arrows) for the products from (a) CCMP, (b) filtered CCMP, (c) modified Rankine vortex plus Coriolis effect and translation velocity, and (d) the blended. The blended wind (d) is made of (a) and (c)……..21

2.4 Examples for (top) shortwave radiative flux and (bottom) total precipitation rate before (solid) and after (dotted) 8-day low-pass Lanczos filtering for the region of 85°E-86°E, 18° N-19°N. The filtering for shortwave radiative flux is exerted on the percentage of solar radiation that is deducted by the clouds. See text for details…….27

2.5 Transfer coefficients (solid) and THF (dashed) curves for SST being 4°C, 3°C, 2°C, 1°C, 0°C, and -1°C (from dark to light) warmer than the air temperature with wind speed from 5m/s to 40m/s and above, assuming 2m air temperature as 26°C, relative humidity as 80% and pressure as 1013mb. The curves are produced based on COARE 3.0 algorithm [Fairall *et al.*, 2003]……....29

3.1 SST differences between 10/12-10/14 mean and 10/19-10/21 mean (TC1 effect) from (a) Tropical Rainfall Measuring Mission (TRMM) – Microwave Imager (TMI), (b) the RcWIND run, and (c) the MR, and between 11/3-11/5 mean and 10/22-10/24 mean (TC2 effect) from (d) TMI, (e) RcWIND, and (f) the MR. The superimposed black lines are the tracks of TC1 (left column) and TC2 (right column). The winds near the strongest stage (10/17 00Z for TC1 and 10/29 00Z for TC2) of the TCs are also plotted (vectors in the middle and bottom panels). The black contour is for 0°C SST…….33

3.2 Sea surface height anomaly at three different times from AVISO (left column) and the RcWIND experiment (right column) during the TCs' period. The reconstructed winds for RcWIND are also shown as vectors in the right column……...…36

3.3 The buoy and cruise sampling locations from October to December, 1999. Red and blue dots represent good quality temperature data by drifting buoys, while brown dots are "unchecked" temperature data. Black diamonds represent cruise campaigns that collect not only surface but also subsurface temperature data. Blue dots are the drifting buoys measurements in the region of 80°E – 82.7°E, 0°N – 5°N after 11/16 in 1999. See text for more description for the purpose of separating blue from red……...37

3.4 SST comparisons between the MR results and drifting buoy observations. Blue triangles are for the data in the region of 80°E – 82.7°E, 0°N – 5°N after 11/16 in 1999, red crosses are for the data when measurements have good quality and not classified as blue (see text for explanations), and brown crosses for "unchecked" measurements. The numbers shown on the lower right portion of the Figure are standard errors. The RcWIND results are very similar to those of the MR…….38

3.5 Temperature profiles from cruise observations (red) and from HYCOM RcWIND (black). The MR and RcWIND have almost identical temperature profiles from the equator to 10°N. Only 12 out of 47 temperature profiles are shown to demonstrate the model skill from 76°E to 96°E at every 2° interval (Fig. 3.3, black diamonds) during October – November, 1999……39

4.1 a) Temporal variations of the BoB OHC, which is the OHC integrated over the region north of 10°N for the entire water column, together with the temporarily accumulated NetHF and meridional OHT from the MR; b) the differences of OHC between the MR and EXPs for the BoB; c) same as b) but for the differences of meridional OHT accumulations; d) same as b) but for the differences of NetHF accumulations. OHT is defined as the meridional heat transport across 10°N into the BoB, and is calculated as the residual of OHC change subtracting NetHF accumulation……...44

4.2 a) SST difference between the MR and NoWIND for 11/3 mean; b), c), d), e) and f) are similar to a), but for the differences between RcWIND and NoWIND, between the MR and NoRAD, between RcWSTR and NoWSTR, between the MR and NoTC, and between RcWIND and NoTC, respectively…….49

4.3 The potential temperature (solid lines) and salinity (dashed lines) profiles during and after TC1 and TC2 for top 100m of Region A (top row), for the top 100m of Region B (middle row), and for the top 80m of the BoB to the north of 10°N. The thin black curves are the potential temperature and salinity profiles at 10/11 00Z, four days before TC1, and thus all the model runs share identical potential temperature and salinity profiles according to the experiment design. The dotted lines show the mixed layer depth for the MR (black), NoWIND (green) and RcWIND (red)……...52

4.4 The OHC differences between the MR and a series of EXPs for the top a) 10m, b) 50m, c), 100m, d) 200m and e) 400m in the BoB (north of 10°N)……..…57

4.5 Areal-averaged ML depth (solid) and temperature (dotted) differences between the MR and EXPs……..60

4.6 Areal-averaged heat potential of the BoB between the MR and EXPs……..…62

5.1 Daily-averaged SSH (color shades) and 10m wind stress (vectors) for RcWIND (left), the differences between RcWIND and NoWSTR (middle), and the differences between RcWIND and NoTC (right) for 10/14, 10/17, 10/18, and 10/21 of 1999. The black line represent TC1's track, and the black crosses represent the locations of TC1 centers every 6 hours from 00Z to 24Z of the day. TC1's strongest stage occurs on 10/17……...69

5.2 Daily-averaged SSH (color shades) and current velocity in the top 30m (vectors) for RcWIND (left), the differences between RcWIND and NoWSTR (middle), and the differences between RcWIND and NoTC (right) for 10/14, 10/17, 10/18, and 10/21 of 1999. The black line represent TC1's track, and the black crosses represent the locations of TC1 centers every 6 hours from 00Z to 24Z of the day. TC1's strongest stage occurs on 10/17……..70

5.3 (left) Ekman transport (vectors) and Ekman pumping velocity (color shades), and (right) top 30m-averaged temperature tendency by vertical mixing (black contours for neutral and cooling, and red contours for warming; interval: 0.4K/day) and by horizontal OHT (color patches; definition is given in the text) from RcWIND. Temperature tendency between -0.4K/day and 0.4K/day by horizontal OHT in the right column is suppressed. TC1's track is superimposed on the map (black line), and the crosses represent the locations of the TC centers every 6 hours from 00Z to 24Z of the day……..…73

5.4 Vertical potential temperature profile at 85.375°E, 18.125°N from RcWIND for a) 10/16 12Z, b) 10/17 06Z, c) 10/18 00Z, d) 10/19 00Z and e) 10/20 00Z of 1999. The thick lines with triangle symbols are the potential temperature at the time, while thin black lines without

symbols are the potential temperature in panel a (the earliest profile that is being shown). The triangle symbols are located at the center of each model layer, whose thickness may vary with time. The 30m depth and 26°C isotherm are also shown as thin black lines for reference purpose……...…76

5.5 An example of $T_{0\text{-}30m}$ (color shades) and currents in the top 30m (vectors) near the landfall location of TC1 from RcWIND experiment. The fields shown here are 6-hourly average centered at 03Z, 09Z, 15Z and 21Z on 10/18 of 1999……...78

5.6 Time Series of potential temperature from RcWIND at 85.375E, 18.125N for 15m, 30m, 50m, 100m, 150m, and 200m……79

5.7 (left) Differences of daily-averaged SSH (color shades) and 10m wind stress (vectors) between RcWIND and NoTC, and (right) differences of daily-averaged SSH (color shades) and current velocity in the top 30m (vectors) between RcWIND and NoTC for 10/27of 1999. The black line represent TC1's track, and the black crosses represent the locations of TC1 centers every 6 hours from 00Z to 24Z of the day…….80

5.8 Similar to Fig. 5.1, but for TC2 and 10/28, 10/29, 10/30, and 11/3……...82

5.9 Similar to Fig. 5.2, but for TC2 and 10/28, 10/29, 10/30, and 11/3……...83

5.10 Similar to Fig. 5.3, but for TC2 and for 10/28, 10/29, 10/30, and 11/3. The presenting domain is also enlarged and shifted……...…85

5.11 Similar to Fig. 5.4, but at 87.875°E, 18.625°N and for 10/28 00Z, 10/28 18Z, 10/29 00Z, 10/29 12Z……...……87

5.12 Similar to Fig. 5.5, but for TC2 and 6-hour time-averaged centered at 03Z, 09Z, 15Z and 21Z for the period from 10/28 12Z to 10/30 12Z…….….88

5.13 Similar to Fig. 5.5, but at 85.625E, 18.375N for 15m, 30m, 50m, 100m, 150m, 200m, and 250m……..90

5.14 Satellite-observed (left; AVISO) and model-simulated (right; RcWIND) SSHAs (color shades) at 00Z 11/17 of 1999, and at 00Z 1/5 and 2/23 of 2000. The ML current velocities from RcWIND are shown as arrows on the right column……91

6.1 The flow chart for producing ocean surface forcing fields for HYCOM and producing SST for HWRF. *H* represents hurricane states, *O* ocean states, *OSF* ocean surface forcing fields, and *CP* TC central pressure. The black thick arrows indicate the data stream flow, and thin long arrows show the OSF and SST extracted from *H* and *O* from one step feeding into the next. The reanalysis data and other observations in the diamonds are used to nudge the model runs……105

Acronyms

BoB: Bay of Bengal

CCMP: Cross-Calibrated Multi-Platform

COARE: Coupled Ocean-Atmosphere Response Experiment

CSM: NCAR Climate System Model

DOHP: Downward Ocean Heat Pumping

ECMWF: European Centre for Medium-Range Weather Forecasts

ERAI: ECMWF Re-analysis Interim

EXP: Experiment Run, including NoWIND, RcWIND, NoRAIN, NoRAD, NoTC, NoWSTR, and RcWSTR

GODAS: Global Ocean Data Assimilation System

HadCM3: Hadley Centre Climate Model 3

HWRF: Hurricane Weather Research and Forecasting Model

HYCOM: Hybrid Coordinate Ocean Model

IBTrACS: International Best Track Archive for Climate Stewardship

KPP: K-profile Parameterization

ML: Mixed Layer

MR: Main Run

MSW: Maximum Sustainable Wind

NCAR: National Center for Atmospheric Research

NCEP: National Centers for Environmental Prediction

NetHF: Net Surface Heat Flux – sum of net radiative flux and net turbulent heat flux

NRL: Naval Research Laboratory

OGCM: Ocean General Circulation Model

OHC: Ocean Heat Content

OHT: Ocean Heat Transport

SST: Sea Surface Temperature

SSH: Sea Surface Height

TC: Tropical Cyclone

THF: Turbulent Heat Flux

TRMM: Tropical Rainfall Measuring Mission

Chapter 1

Introduction

1.1 Background

Quantifying oceanic meridional heat transport has important implications for climate research. The equator-to-pole transport of heat by the ocean-atmosphere system buffers temperature extremes, allowing the climate system to reach radiative equilibrium and thus regulating climate. Using an inverse approach, MacDonald and Wunsch [1996] estimated that the world's oceans transport roughly half of the heat that moves from the tropics to the poles, while the atmosphere carries the other half. Moreover, the ocean is considered the primary contributor in the tropics [e.g., Held, 2001]. The ocean's capability to store and transport heat may also be linked to the sequestration of the global warming signal [Meehl *et al.*, 2005 and 2011]. Estimating meridional ocean heat transport (OHT), however, remains challenging, and significant discrepancies exist among different estimates [Trenberth and Caron, 2001; see also Gordon, 2000 and Held, 2001]. Trenberth and Caron [2001] compared 1) derived northward OHT estimates based on atmospheric reanalysis data, 2) simulated northward OHT from the coupled models, and 3) direct northward OHT observations for the Atlantic Ocean and the World Ocean (Fig. 1.1). To the south of 40°N in the Atlantic Ocean, the derived northward OHT estimate based on the atmospheric reanalysis data of National Centers for Environmental Prediction and National Center for Atmospheric Research (NCEP/NCAR) generally differ from that based on the atmospheric reanalysis data of European Centre for Medium-Range Weather Forecasts (ECMWF) by 0.25 PW or more. Several direct observational estimates of northward

OHT have large error bars that lie outside of ±1 standard errors of OHT estimated from NCEP/NCAR and ECMWF atmospheric reanalysis data (Fig. 1.1; top panel). The discrepancy of the Northern Hemisphere peak northward OHT (near 20°N) between the simulation from the NCAR's Community Climate System Model (CCSM) and ECMWF reanalysis data estimate is ~0.4PW in the Atlantic Ocean (Fig. 1.1; middle panel), while the discrepancy of the Southern Hemisphere peak northward OHT for the World Ocean (near 15°S) between the two reanalysis estimates is larger than the NCAR CCSM simulated value (Fig. 1.1; bottom panel).

The OHT from the tropics to the poles consists of three major components: a) downward diapycnal heat transfer into the ocean in the tropics, b) poleward OHT into the high latitudes, and c) heat release back to the atmosphere. In addition to the aforementioned significant discrepancies among the meridional OHT estimates, observed diapycnal diffusivities in the lower latitudes are also typically found too low to account for the required downward heat flux inferred from budget analyses [e.g., Ledwell *et al.*, 1993; Gregg *et al.*, 2003]. The measurements of Ledwell *et al.* and Gregg *et al.* were primarily made under low wind conditions, because it is very difficult to avoid the interference of turbulence under high wind conditions. Consequently, diapycnal turbulent mixing induced by strong winds, such as those associated with tropical cyclones (TCs), has been shown to be an important mechanism for vertical ocean mixing budgets in the tropics [Sriver and Huber, 2007; Sriver *et al.*, 2008], and it has been hypothesized that these events may contribute substantially to oceanic meridional heat transport [Emanuel, 2001].

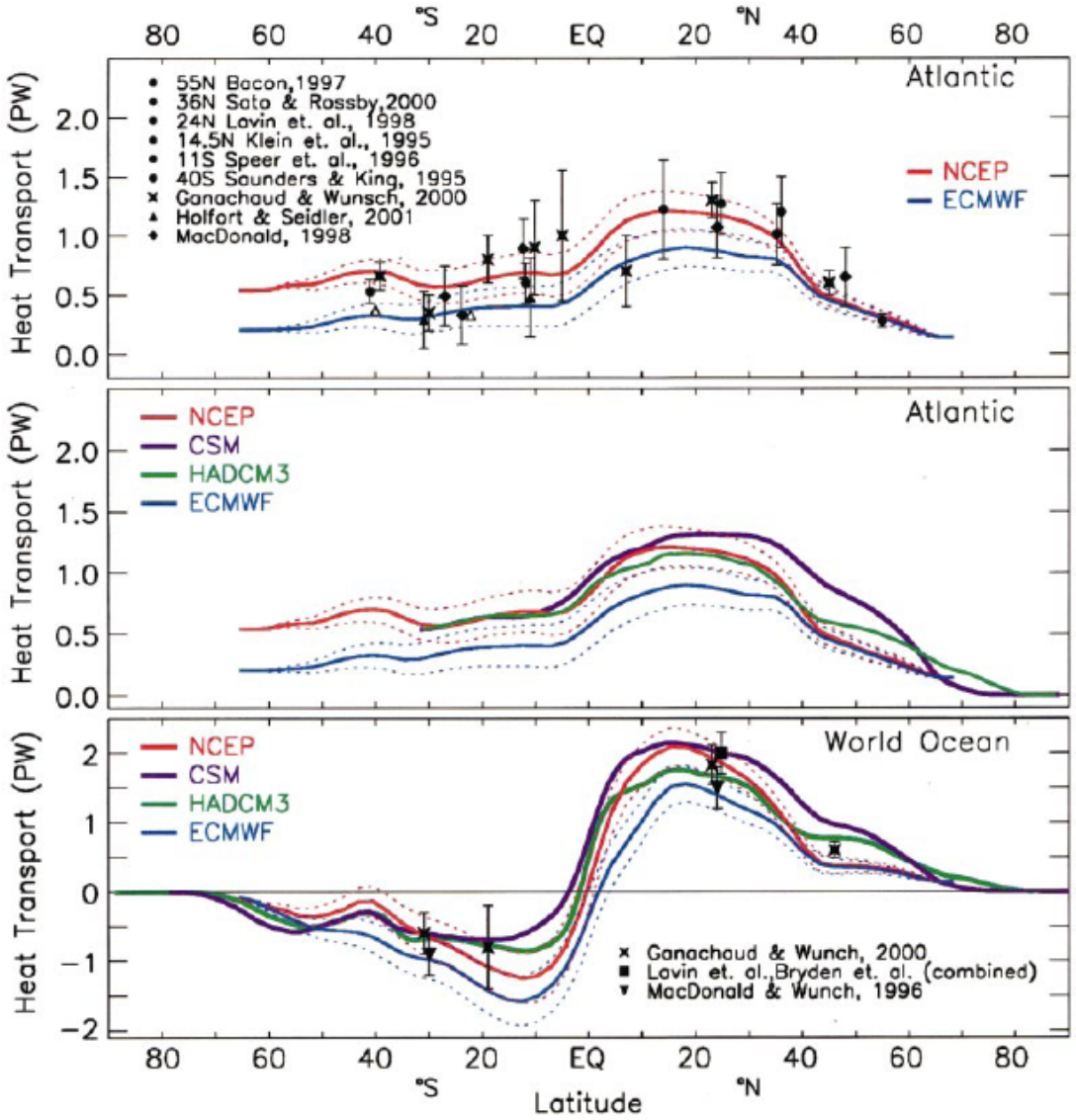

Fig. 1.1: Northward OHT for the Atlantic Ocean (top and middle) and the World Ocean (bottom). Three types of OHT are plotted: 1) derived northward OHT estimates based on atmospheric reanalyses from the National Centers for Environmental Prediction and National Center for Atmospheric Research (NCEP/NCAR; red) and the European Centre for Medium-Range Weather Forecasts (ECMWF; blue), 2) simulated northward OHT from the coupled models – the NCAR Community Climate System Model (CCSM; black curves) and the Hadley Centre Climate Model 3 (HADCM3; green), and 3) direct northward OHT observations (black symbols with error bars). The dashed curves represent the ±1 standard error for the derived OHT. Image taken from Trenberth and Caron [2001].

1.2 TC Impacts on Ocean Heat Pumping and Heat Transport

Price [1981] showed that the cyclonic rotation of the wind field associated with moving TCs

causes near-inertial oscillations in the wake, which increases shear instability at the bottom of the mixed layer (ML) and induces strong upper ocean mixing. Because the tropical oceans are stably stratified, vertical mixing leads to reduction in sea surface temperature (SST) by mixing with the colder water from below. Black [1983] suggested that cold water entrainment at the bottom of the ML, which is induced by direct stirring of TC winds and shear instability that is associated with near-inertial oscillation afterwards, may account for over 80% of the observed SST decreases in the wake of a TC. Emanuel [2001] hypothesized that turbulent mixing induced by TCs' winds could homogenize the upper ocean temperature, thus lowering SST, warming the upper thermocline, and potentially causing a net oceanic heat convergence through restoration of cold anomalies via enhanced surface fluxes (Fig. 1.2). This net oceanic heat convergence, or downward ocean heat pumping (DOHP), measures the amount of heat that is pumped down from the ML into the thermocline by the TC winds-induced turbulent mixing process. In steady state, this additional heat would be later carried away from storm-affected regions by lateral advection and has been hypothesized to be important for the ocean's heat budget and transport. Emanuel [2001] used a simple coupled ocean-hurricane model to estimate the net ocean heating induced by global TC activities during 1996. He concluded that the TC-related heating is approximately 1.4±0.7 PW (1 PW=10^{15}W), which may account for a substantial portion of the OHT carried by the meridional overturning circulation.

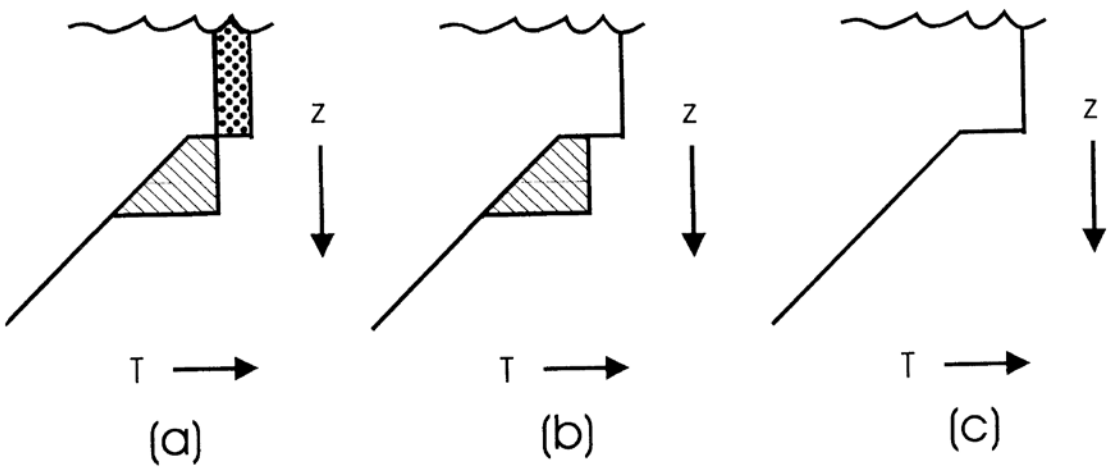

Fig. 1.2 Schematic diagram showing the three stages of DOHP by TCs. Stage (a) shows the upper ocean temperature homogenization, which lowers the ML temperature and raises the temperature of the upper thermocline layer, Stage (b) shows restoration of the ML temperature via enhanced downward surface heat flux and advection, and Stage (c) shows that the additional heat in the upper thermocline layer is carried away by lateral advection. In Stage (a), the warm anomaly in the upper thermocline layer (striped) compensates the cold anomaly in the ML (dotted), and thus there is no net column heating in this stage. Image taken from Emanuel [2001].

As more *in situ* and satellite observations become available, advancements have been made to improve our understanding of hurricane- and typhoon-induced upper ocean variability in the Atlantic and Pacific Oceans through both observational and modeling studies [e.g., Jacob and Shay, 2003; Black *et al.,* 2007; D'Asaro *et al.,* 2007; Yin *et al.,* 2007; Siswanto *et al.,* 2008; Huang *et al.,* 2009; Lin *et al.,* 2009; Wada *et al.,* 2009; Jiang *et al.,* 2009; Tseng *et al.,* 2010; Zheng *et al.,* 2010]. In an effort to improve the estimate of TC impacts on upper ocean heat budget, Jacob and Shay [2003] produced improved forcing fields by blending field observations for Hurricane Gilbert of 1988 with reanalysis data, and then used the forcing fields to drive an oceanic general circulation model (OGCM). Sriver and Huber [2007] used the observed SST before and after TCs to calculate the global heat exchange due to TCs, based on the hypothesis of Emanuel [2001]. Their estimate suggests that TCs contribute ~0.26 PW to OHT, which is considerably smaller than the Emanuel's [2001] original 1.4±0.7 PW estimate. Furthermore,

Sriver *et al.* [2008] showed that adopting seasonally and spatially varying upper ocean temperature profiles and using different SST products can result in ~60% change in DOHP estimates. It also appears that there are several factors that modulate the oceanic response to TCs, such as regional differences in the background state, timing of the TC occurrence, and size, intensity and translation speed of the TC event [e.g. Sriver and Huber, 2010; Sriver *et al.*, 2010]. Several other observational [e.g., Jansen *et al.*, 2010] and modeling [e.g., Jansen and Ferrari, 2009; Sriver and Huber, 2010; Sriver *et al.*, 2010; Fedorov *et al.*, 2010; Manucharyan *et al.*, 2011] studies have been conducted to investigate the DOHP effect and the impacts of TCs on global ocean heat budget and transport, and yielded mixed results. For instance, while some model simulations show that TCs induce substantial changes in ocean and atmosphere circulation and heat transports [Manucharyan *et al.*, 2011], others show that ocean heat is carried back to the equatorial thermocline when TC-induced ocean mixing occurs outside 30° of the equator [Jansen and Ferrari, 2009]. The discrepancies among different estimates demonstrate the need for an improved understanding and quantification of how and why the upper ocean heat content (OHC) is altered and redistributed by TCs.

1.3 Impacts of Tropical Cyclones (TCs) in the Indian Ocean

Compared to the Pacific and Atlantic Oceans, fewer studies of TC-induced upper ocean variability have been done in the Indian Ocean. Gopala Krishna *et al.* [1993] showed the oceanic thermal response to a severe cyclonic storm in May, 1999 and recognized the importance of upper ocean mixing and upwelling in determining the subsequent air-sea heat exchange. Murty *et al.* [1996] provided a good background hydrographic description of the Bay of Bengal (BoB) and discussed the effect of a deep depression in August, 1990 on the upper ocean heat content.

Attention also has been paid to the devastating societal and economical impacts of the TCs, such as the very severe TC Nargis in May 2008 [e.g., Webster, 2008; Fritz *et al.,* 2009]. In the BoB, cyclones are often active during spring (pre-monsoon season) and fall (post-monsoon season). By analyzing satellite and *in situ* observations, existing studies have documented the ocean-atmosphere conditions and their co-variability associated with TC Nargis [e.g., Shi and Wang, 2008; Kikuchi *et al.,* 2009; Yu and McPhaden, 2011]. It has been shown that SST dropped by over 2-3°C, wave heights were 3-4 meters to the right of the cyclone, and oceanic biological activity and suspended matter apparently increased after Nargis' passage, indicating that Nargis caused strong oceanic mixing.

In this dissertation, the author focuses on two Indian Ocean TCs in 1999 that landed at Orissa, India: 04B (hereafter TC1) and 05B (hereafter TC2). A few studies have investigated the influence of SST on the intensity and track of TC2, and vice versa. It is suggested that better-resolved SST spatial and temporal variations may improve TC2 intensity and track prediction in the model [Mandal *et al.,* 2007; Bongirwar *et al.,* 2011], and the region of maximum surface cooling shifted to the left of the cyclone track when the TC translated over the coastal waters [Mahapatra *et al.,* 2007]. Chinthalue *et al.* [2001] showed vigorous temperature and salinity anomalies induced by TC2, and Subrahmanyam *et al.* [2005] described the history of TC1 and TC2 and attempted a regression relationship between the outgoing longwave radiation, which represents tropical deep convection, and ocean surface response. To date, studies on TCs' effects on DOHP and OHT in the BoB have not yet been done. How does the upper ocean respond to TCs in the BoB, and how is the response compared with similar events in Atlantic and Pacific Oceans? Due to the large amount of freshwater input from monsoon rainfall and river runoff into the BoB, the upper ocean is strongly stratified and the barrier layer persists [e.g., Han

et al., 2001; Howden and Murtugudde, 2001; Masson *et al.*, 2002; Vinayachandran *et al.*, 2002; for barrier layer definition see Lukas and Lindstrom, 1991 and Sprintall and Tomczak, 1992]. Sengupta *et al.* [2008] suggested that post-monsoon TCs have lesser effect on SST cooling as revealed by satellite observations, likely because freshwater input from river runoff and monsoon rainfall leads to temperature inversion, where warmer water resides below the surface and forms a barrier layer. Mixing due to strong TC winds entrains warmer water into the surface layer, and thus produces less cooling.

1.4 Present research about the TC effects on the BoB heat budget

The BoB is geographically unique in that it is a semi-enclosed basin, which is bounded by continents to the north, east and west but is open to the warm Indian Ocean SST in the south. As a result, this region is subject to strong forcing from the seasonally reversing monsoon winds and precipitation. The strong rainfall associated with the summer monsoon, together with a large amount of freshwater discharged from the Ganges-Brahmaputra, Irrawaddy, and other smaller rivers into the Bay, make the BoB one of the freshest parts of the world's oceans. This seasonal freshening increases the stratification and limits vertical mixing. On the other hand, strong monsoon and TC winds may overcome the strong stratification and mix heat downward. Due to its semi-enclosed nature, excessive heat accumulated in the BoB has to be transported southward out of the Bay.

Most of the previous studies that investigated the impacts of TCs on the upper ocean heat budget focused on the effects of winds [e.g., Jacob *et al.*, 2000; Emanuel, 2001]; however, other processes may also be important. For example, a recent modeling study by Hu and Meehl [2009] suggested that the effect of hurricane rainfall could counteract the effect of hurricane winds.

While the hurricane winds enhance northward heat transport of the Atlantic meridional overturning circulation, the precipitation reduces it through meridional redistribution of freshwater originating in the tropics. Thus, the overall effect on OHT depends on the relative magnitude of these two competing processes. Jansen *et al.* [2010], on the other hand, suggested that the TC effects on DOHP may be greatly reduced due to the seasonal ML deepening and ocean heat release back to the atmosphere. While these recent studies have broken important new ground related to the relationship between TCs and climate lined to upper ocean processes and air-sea interactions, the use of high-resolution ocean models could provide a useful tool for developing a better understanding and quantification of the processes associated with TC-climate impacts via strong winds, precipitation, surface turbulent heat fluxes, and shortwave and longwave radiation.

The goal of this study is to understand how the upper ocean in the BoB responded to the two TCs that landed at Orissa in 1999, with special emphasis on the upper ocean heat budget, including DOHP and OHT. A series of experiments are conducted using an OGCM – the HYbrid Coordinate Ocean Model (HYCOM), to assess the processes by which the two TCs caused the upper ocean heat change. The DOHP effect is quantified from the perspective of air-sea heat exchange, by estimating the difference of ocean surface heat gain between the model simulations with and without TCs, which avoids the assumption of negligible surface heat flux during the TCs and SST cooling induced entirely by vertical mixing [e.g., Emanuel, 2001; Sriver and Huber, 2007; Sriver *et al.*, 2008].

Most of the previous numerical studies that investigated TCs' impact on the ocean concentrated on the ocean state change [e.g., Jacob and Shay, 2003; Black *et al.*, 2007; Wada *et al.*, 2009; Tseng *et al.*, 2010]; however, a lot fewer quantified the TC effect on DOHP and OHT

[e.g., Emanuel, 2001; Jansen and Ferrari, 2009; Sriver and Huber, 2010; Sriver *et al.*, 2010; Fedorov *et al.*, 2010; Manucharyan *et al.*, 2011]. Also, to the best knowledge of the author of this dissertation, there has not been any numerical study before this one that quantifies TCs' impact on the Indian Ocean heat budget. In addition to the new research location, this study consists of three other unique features: 1) the TCs' impact is quantified as the difference between the simulations with and without TC signals in the forcing fields, instead of "before-vs.-after" method that is prevalently used by previous studies, in which TCs' impact is estimated as the differences of ocean states between before and after TCs; 2) the effect of the individual TC-associated forcings is quantified and assessed in terms of physical processes and ocean heat budget, compared to the entangled response to the combination of all the TC-associated forcings in the previous works; 3) this research investigates the ocean response to two consecutive TCs and the following seasonal change, which will later be shown to be weaker than the sum of the response to two stand-alone TCs before or in the middle of summer season. The unique experiment deign of this study will be elaborated in Chapter 2.

The rest of the thesis is organized as follows: Chapter 2 describes the TC cases, model configurations, and ocean surface driving forces. TC winds reconstruction and the wind stress calculation are also described. To demonstrate the contrasts of model results with and without certain TC forcings, the experiment design and the method of removing individual TC forcing signals are presented in this chapter. Chapter 3 reports our results on the comparison between the model simulations and observations. The model output is evaluated against satellite-observed SST and sea surface height, as well as against buoy and cruise observations. Chapter 4 examines the TCs impacts on the BoB heat budget and associated processes by contrasting the model results with and without certain TC-associated forcings. Chapter 5 assesses the TCs impacts on

sea level and upper ocean circulation. Chapter 6 provides a summary of general conclusions and discusses future work. The materials in Chapter 1-4 have been published in two companion papers [Wang *et al.*, 2012a and 2012b]. The first paper, whose major content can also be found in Chapter 1-3 of this dissertation, discusses study purpose (Chapter 1), model setup and forcing fields (Chapter 2), and model evaluation (Chapter 3); the second paper, whose major content can be found in Chapter 1, 2, and 4 of this dissertation, discusses the concept of TCs' impact on ocean heat budget (Chapter 1), experiment design and TC signals in the forcing fields (Chapter 2), and quantification of TCs' impact (Chapter 4).

Chapter 2

Description of Cyclone Cases, Ocean Model and Experiments

2.1 Description of the TCs

In this study, two consecutive TC cases – 04B (10/15 00Z – 10/19 06Z) and 05B (10/25 00Z – 11/3 06Z) – that occurred in 1999 are chosen to demonstrate TCs' impacts on the ocean. Cyclone 04B (TC1) formed over the center of the BoB on 10/15 and traveled west-northwestward across the BoB. After explosive intensification on 10/16, TC1 was classified as category 4 at 10/17 00Z and turned northward before it made landfall on the same day at Orissa, India (see Fig. 2.1, top-left panel for its track and bottom-left for the maximum sustainable wind speed).

Within a week after TC1 dissipated, a tropical depression crossed the Malay Peninsula on 10/25 and then intensified into a cyclone on 10/27 while it traveled northwestward. Cyclone 05B (TC2) reached category-5 strength at 10/28 18Z and made landfall to the northeast of the landfall location of TC1 after a rapid intensification (Fig. 2.1, top-right and bottom-right panels). It stalled inland and weakened to a tropical storm. The tropical storm turned southward and re-entered the BoB on 10/30 and turned in a south-southwestward direction. TC2, also known as the 1999 Orissa cyclone, was one of the deadliest TCs in the twentieth century and resulted in more than 10,000 casualties [International Federation of Red Cross and Red Crescent Societies, 2001]. The cyclone winds reached ~72 m/s (~140 knots) with an estimated minimum central pressure of lower than 912 hPa before it hit Orissa, India. The rainfall over southeast India caused record flooding in the low-lying areas [U.S. Navy 1999 Annual Tropical Cyclone Report],

partly due to the soil saturated by TC1 rainfall and the topographical stalling of TC2 over land. The total effect of storm surge, tide and local topography on sea level elevation at Paradip, Orissa was reported to be 5-6 meters [Latha and Rao, 2007]. The occurrence of these two intense TCs during a short time span offers a unique opportunity to examine how surface heat fluxes and ocean heat transport within the BoB were modified by their passage.

2.2 The HYbrid Coordinate Ocean Model (HYCOM) and Forcing Fields

The OGCM used to examine the TCs' impact is HYCOM. HYCOM utilizes terrain-following sigma coordinates in coastal regions, isopycnic coordinates in the open ocean interior, and z coordinates in very shallow waters and near the surface. The details of the model dynamics and physics are documented in Bleck [2002] and Halliwell [1998 and 2004]. HYCOM has been applied in a wide range of studies with various timescales and regions, including the Indian Ocean [Han, 2005; Han *et al.,* 2006a,b; Yuan and Han, 2006; Han *et al.,* 2007], the Atlantic Ocean [Han *et al.,* 2008], the Black Sea [Kara *et al.,* 2005a,b], the tropical Pacific Ocean [Shaji *et al.,* 2005], and the Gulf of Mexico [Prasad and Hogan, 2007].

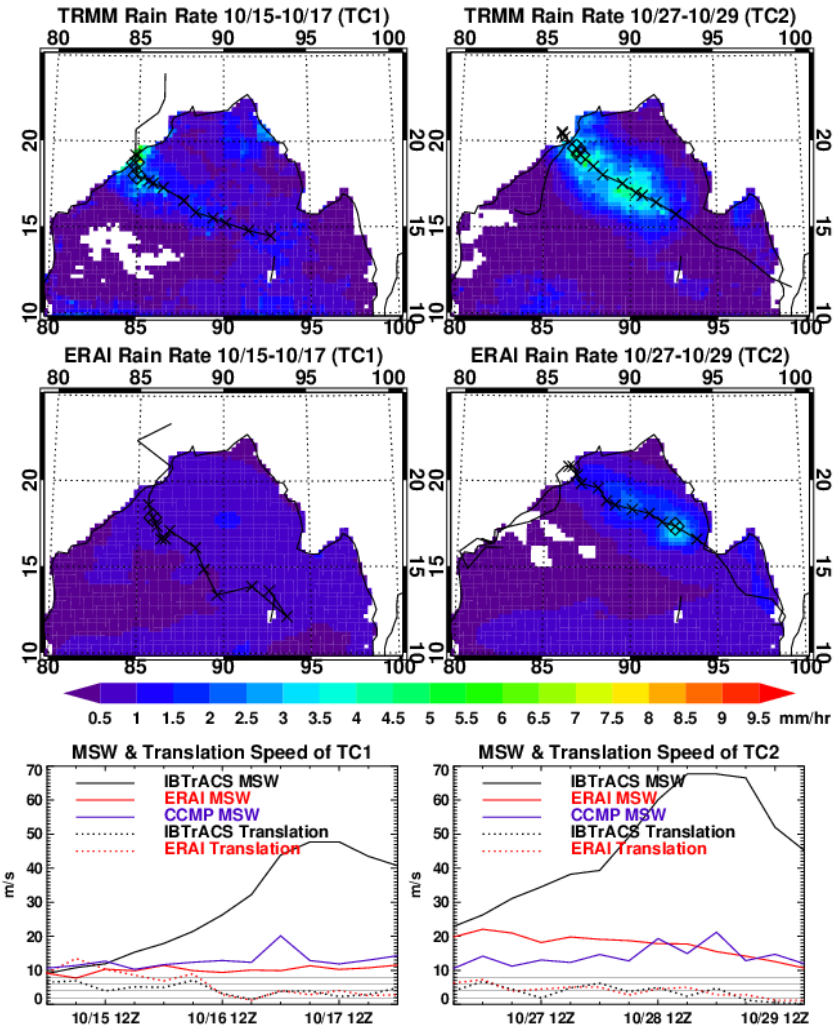

Fig. 2.1: The three-day mean TRMM 3B42 rain rate (top panels), the three-day mean ERAI rain rate (middle panels), and maximum sustainable wind (MSW) speed and translation speed (bottom panels) for the two TC cases. For TC1, the rain rate averaging period is 10/15-10/17, while for TC2, 10/27-10/29. The black lines are the cyclone tracks from IBTrACs (top panels) and determined from ERAI lowest mean sea level pressure (middle panels), while the crosses are the cyclone centers every six hours during the three-day period. Missing values and zero precipitation in TRMM data are shown as white background. Note that TC1 center from ERAI at 10/15 00Z is ambiguous.

2.2.1 Indian Ocean Configuration

The model is configured to the Indian Ocean (35ºS-30ºN, 20ºE-120ºE) with a horizontal resolution of 0.25º×0.25º. This resolution is eddy permitting and can reasonably resolve the impacts of TC forcings on the upper ocean, given that the radii of 18m/s (~35-kt) winds in TC1

and TC2 sometimes exceeded 220 km (~120 nautical miles) and the radii of 51m/s (~100-kt) wind (if any) were always at least 28 km (~15 nautical miles), as shown in US NRL (Naval Research Laboratory) TC warnings. Vertically, 30 hybrid layers are chosen with fine resolution in the upper ocean to better resolve the vertical structures of upper ocean currents, temperature, and salinity. The first layer is set to be 3m deep, and the thickness of the following layers increases as an exponent of 1.125 (i.e., layer n thickness $H_n=3\times1.125^n$) until the coordinate transforms to isopycnal coordinate. With the choice of the aforementioned hybrid coordinates and potential density (sigma) values, the number of layers for the top 50m ranges from three layers near Burma's coast to 10 layers in the southwest corner of the BoB. Realistic bottom topography from the National Geophysical Data Center 2'×2' digital bathymetry is used with 2°×2° smoothing.

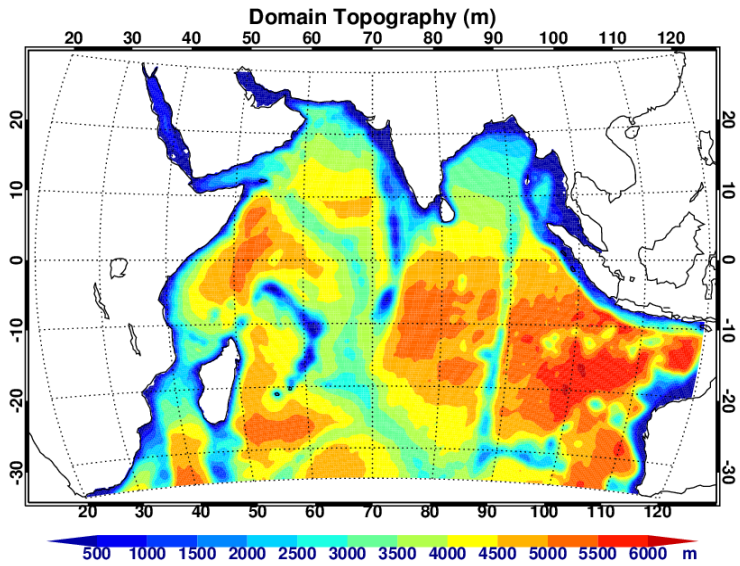

Fig. 2.2: Topography map of the domain for the HYCOM experiments. South China Sea is masked out as land, while the temperature and salinity of the remaining eastern boundary along 120°E and southern boundary along 35°S is relaxed to monthly ocean objective analysis product from the Meteorology Office of the UK.

A reference pressure at sea level is adopted because we focus on upper ocean processes. Nonlocal K-profile parameterization (KPP) is used for the boundary layer mixing scheme [Large

et al., 1994 and 1997]. Background diffusivity for internal wave mixing is set to $5x10^{-6}$ m^2/s [Gregg *et al.*, 2003], and viscosity is set to be an order of magnitude larger ($5x10^{-5}$ m^2/s; Large *et al.*, 1994]. The diapycnal mixing coefficient is 1×10^{-7} m^2s^{-2}/N, where N is the buoyancy frequency. Isopycnal momentum dissipation values are formulated as u_dx, where x is the local horizontal mesh size and u_d is set to be 0.015 m/s for Laplacian dissipation and 0.005 m/s for biharmonic dissipation. A similar method is used for temperature and salinity diffusion, with u_d=0.001 m/s for Laplacian diffusion. Near the southern boundary and the Indonesian Throughflow region, sponge layers of five degrees are applied to relax the model temperature and salinity to the monthly ocean objective analysis product from the Meteorology Office of the UK [Ingleby and Huddleston, 2007].

2.2.2 Surface and lateral boundary forcing fields

The HYCOM surface forcing fields include 2m air temperature, 2m humidity, surface net solar radiative flux and net radiative flux (shortwave plus longwave), precipitation, wind speed and wind stress. The sea surface latent and sensible heat fluxes are determined by HYCOM SST, wind speed, air temperature and specific humidity, following the Coupled Ocean-Atmosphere Response Experiment (COARE 3.0) algorithm [Fairall *et al.*, 2003]. This algorithm allows medium to strong wind conditions with a wind speed of ~40 m/s. To obtain the best available forcing fields, both reanalysis products and satellite observations are used to force HYCOM, as discussed below.

2.2.2.1 The ERA-Interim (ERAI) fields and TC records

The 6-hourly ECMWF (European Centre for Medium-Range Weather Forecasts)

Re-analysis Interim (ERAI) products [Simmons *et al.*, 2007; Dee *et al.*, 2011] for the period of 1989-2008 are used to force HYCOM. The ERAI data assimilation uses 12-hour 4D-Var at T255 horizontal resolution (~0.7031252º). The 6-hourly surface analysis fields, including 2m air temperature, 2m humidity, 10m wind velocity, and 6-hourly surface accumulated fields, including wind stress, precipitation, surface net longwave radiation, and surface net solar radiation, are extracted for HYCOM forcing fields. All fields are interpolated onto HYCOM grids. The ERAI sea level pressure fields are also used to track the TC center positions (middle panels of Fig. 2.1), while the ERAI maximum wind speeds at 10m near the TC centers are shown only for comparison purpose (bottom panel of Fig. 2.1). The center positions from ERAI differ by up to 2° central angle compared to International Best Track Archive for Climate Stewardship (IBTrACS) data during the strengthening stage (compare top and middle panels of Fig. 2.1).

IBTrACS is endorsed by the World Meteorological Organization Tropical Cyclone Program (data from http://www.ncdc.noaa.gov/oa/ibtracs/), and the project combines the best available storm track records from all the regional specialized meteorological centers to provide the public with the information for storm position, maximum sustainable wind (MSW), minimum central pressure, storm name, radius of RSW, etc. at 6-hourly frequency. When there is a tropical cyclone, the nearby regional specialized meteorological center as well as other TC centers will issue their warning reports, in which the storm location and strength based on satellite images (Dvorak technique; Dvorak, 1975 and 1984) or radar images (if available) are recorded.

Note that the 2.5ºx2.5º International Satellite Cloud Climatology Project flux data (ISCCP-FD; Zhang et al. 2004) shortwave and longwave fluxes are also used to force HYCOM. Due to their coarse resolution, however, they cannot reasonably resolve the TC effects. HYCOM solutions forced by ERAI shortwave and longwave fluxes agree better with the observations than

forced by the ISCCP data (not shown).

2.2.2.2 TRMM precipitation

The Tropical Rainfall Measuring Mission (TRMM) [Kummerow *et al.,* 1998 and 2000] Multi-Satellite Precipitation Analysis (TMPA) intercalibrates and combines TRMM 2A-12, SSMI, AMSR and AMSU precipitation estimates from different orbiting satellites, referred to as high quality estimates. Rain rate estimates by the geostationary satellites' infrared band observations are then also made by fitting the infrared brightness temperatures to the high quality estimates. The infrared rain rate estimates have 3-hourly or higher temporal resolution. Both the rain rates are scaled to match the monthly satellite/rain gauge analyses. The TRMM 3B42 product (0.25°×0.25°, 3-hourly and 50°S-50°N) is used to force HYCOM. Its retrieval algorithm can be found in Huffman *et al.* [1995 and 1997] and Huffman [1997]. For HYCOM experiments, the 3-hourly product is averaged onto a 6-hourly interval to be consistent with other forcing fields.

TRMM precipitation data provide stronger rainfall estimates and more accurate TC locations than the ERAI precipitation data (Fig. 2.1). The TRMM rain rate averaged over the time frame of the two TC cases and the TC tracks from IBTrACS are shown in the top panels of Fig. 2.1. The rainy area during 10/15 – 10/17 covers most of the BoB, and its strongest rate happens after the explosive intensification of TC1 (10/17). For TC2, the strong rainy area is more concentrated along its track.

2.2.2.3 CCMP Wind

The global (78.375°S to 78.375°N) 6-hourly Cross-Calibrated Multi-Platform (CCMP)

ocean surface winds on 0.25°×0.25° grids [Atlas *et al.*, 2008 and 2009] are also used to force HYCOM (see section 2.3). The CCMP winds are derived from cross-calibrating ocean surface wind data from SSM/I, TMI, AMSR-E, SeaWinds on QuikSCAT, and SeaWinds on ADEOS-II. These datasets are combined with conventional observations and ECMWF wind field (as a starting/background estimate of wind field), by using a variational analysis method. The CCMP winds more accurately depict the TCs' locations than the ERAI winds (not shown). Although CCMP TC wind speeds are not always higher than ERAI in our cases, the former is more accurate in the timing of strongest stage than the latter (bottom panels of Fig. 2.1).

Powell *et al.* [2003] and Oey [2007] showed that the drag coefficient (C_{10}) increases with the increase of 10m wind speed (V) up to about 34 m/s (also see Large and Pond, 1981), but then levels off and declines at even stronger wind speeds. In this study, wind stress (τ_x and τ_y) is determined from V and air density (ρ) by the formula suggested by Sanford *et al.* [2007] and Zedler *et al.* [2009]:

$$10^3 C_{10} = \begin{cases} 1.2 & \mathrm{V} < 11\mathrm{m/s} \\ [1.2\,1.7\,2.0\,1.8\,1.5] & \mathrm{V} = [11\,28\,34\,40\,50]\,\mathrm{m/s}, \\ 1.5 & \mathrm{V} > 50\mathrm{m/s} \end{cases} \qquad (2.1)$$

$$\tau_x = \rho C_{10} V u\,, \qquad (2.2)$$

$$\tau_y = \rho C_{10} V v\,.$$

The drag coefficient for wind speed between 11, 28, 34, 40, and 50m/s is linearly interpolated accordingly.

2.2.2.4 Lateral boundary forcing: Bay of Bengal River Discharge

The three largest rivers that run into the BoB are the Brahmaputra, Ganges, and Irrawaddy (Table 2.1). Instead of relaxing the salinity in the northern BoB toward climatological values

[e.g., Duncan and Han, 2009], the monthly river discharge data from Dai *et al.* [2009] are utilized as freshwater input to force HYCOM. The discharge data are based on the gauge records at the farthest downstream stations for the world's 925 largest ocean-reaching rivers, and the data gaps in the records are filled through linear regression between the observed streamflow and the streamflow simulated by Community Land Model version 3. For the Brahmaputra and Ganges, the discharge data are better covered by the gauge records for the period of our HYCOM simulations, while for the Irrawaddy, the discharge data for the same period are all from model simulation results (see Table 2.1 for observation coverage time frame).

Table 2.1: The largest three rivers in the model domain based on Dai *et al.* [2009].

River Name	Annual Flow Volume (Sv)	Observation Start	Observation End
Brahmaputra	2.179×10^{-2}	1956/01	2000/12
Ganges	1.273×10^{-2}	1949/01	1996/12
Irrawaddy	1.240×10^{-2}	1978/01	1988/12

2.3 Reconstructed TC Winds

Quantitatively, neither the CCMP nor ERAI winds are able to represent the observed TCs' maximum sustainable wind speeds (Fig. 2.1, bottom panels), although the general cyclonic circulation patterns are captured. The winds from both CCMP and ERAI are too weak, even though sometimes CCMP winds show better agreement with the IBTrACS data. This is because TC's high winds are generally associated with strong precipitation, which contaminates satellite wind retrieval under high wind conditions. Although efforts are being made to tackle this problem, the issue exists for the best available CCMP winds. The underestimation of wind speed may underestimate the mixing and heat pumping effects of the TCs.

In order to investigate oceanic response to high wind conditions ($\geq$18 m/s), a modified Rankine vortex [Holland, 1980] is adopted for azimuthal wind velocity:

$$V = \begin{cases} \frac{V_{\max}}{R} \times r & \text{, for } r < R \\ V_{\max} \times \left(\frac{R}{r}\right)^{x} & \text{, for } r \geq R \end{cases} \qquad (2.3)$$

V_{max} is the maximum sustainable azimuthal wind speed of the TC, and R is the radius of MSW. The radial profile of wind is proportional to r within R and to $1/r^x$ beyond R. The parameter x is estimated to range from 0.4 to 0.6 [Holland, 1980], and 0.5 is used for this research. To account for the Coriolis effect, V is further adjusted so that the absolute angular momentum ($rV+fr^2/2$) is conserved at the same r, where the Coriolis parameter f changes with latitudes. The radial velocity is assumed to be -0.3V [Zedler *et al.*, 2002] within R and decrease at 1/12 of the rate of decrease of the tangential wind speed outside R, similar to Hurricane Eloise in Price [1981].

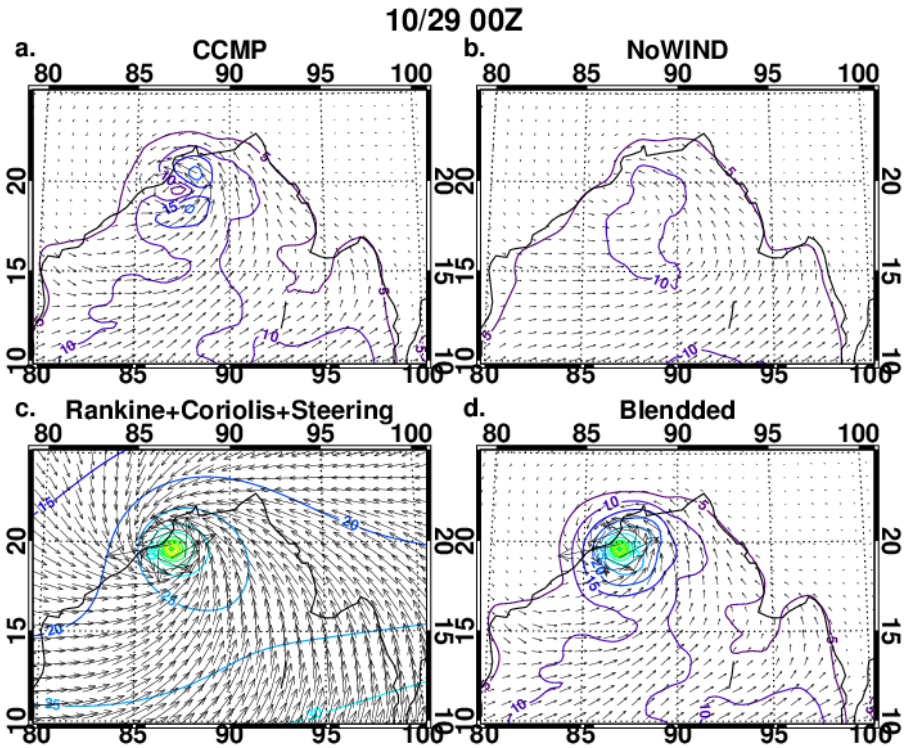

Fig. 2.3: Wind speed (contours; 5 m/s interval) and wind velocity (arrows) for the products from (a) CCMP, (b) filtered CCMP, (c) modified Rankine vortex plus Coriolis effect and translation velocity, and (d) the blended. The blended wind (d) is made of (a) and (c).

An example of implementation of modified Rankine vortex, considering the Coriolis effect and translation velocity and its blending with the CCMP wind field at 10/29 00Z, when TC2 wind speed peaked, is shown in Fig. 2.3c and 2.3d. Linear ramping has been applied in space for the blending to ensure the smooth transition from the centers of the TCs to two times of 35-kt radii of the TCs. Note that to conserve absolute angular momentum, the modified Rankine vortices have the greatest wind speed in the lower latitudes, and only half of the storm translation velocity is added to the modified Rankine vortices, as recommended by NOAA [1979]**.**

2.4 Experiment Design and TC Signal Removal

2.4.1 Experiment Design

In many existing studies (see Section 1.1), the TC effect on OHC and SST is estimated by comparing the sea state before and after a TC event. The “before-vs.-after” method, however, is not able to isolate the processes through which TCs affect the ocean. For example, does the effect of TC rainfall counteract the effect of TC wind on OHT, as suggested by Hu and Meehl [2009]? The experiments in this study improve previous works by using a high-resolution ocean model capable of resolving the processes important for TC-induced changes in OHC and OHT on intraseasonal and seasonal timescales. In this section, the author will describe the experiment design that is used to isolate the impacts of individual TC signals from the forcing fields by comparing HYCOM simulations with and without these signals. This methodology is not restricted by previous assumptions, such as those related to post-storm SST recovery and assumed mixing depths.

HYCOM is first spun up for 20 years using the 1989-2008 monthly climatologies of ERAI forcing fields (Section 2.2.2.1). Restarting from the spin-up solution, HYCOM is integrated

forward in time for the period of 1989-2000 using the 6-hourly CCMP winds (Section 2.2.2.3), and 6-hourly ERAI data for other forcing fields. The 6-hourly (integrated from original 3-hourly data) TRMM 3B42 precipitation (Section 2.2.2.2) replaces the ERAI precipitation to drive the model starting in 1998. This run is driven by the original forcing fields, and is referred to as Main Run (MR). The model results for 1989-1991 are not analyzed, because they contain transient features that result from the transition of the spin-up (monthly climatological driving forces) to the simulation driven by the 6-hourly forcing fields.

Table 2.2: The suite of HYCOM experiments performed for assessing the TCs' impacts. The abbreviation "WIND" stands for wind speed and wind stress, "RAIN" for rain rate, "RAD" for radiation, "WSTR" for wind stress, "WSPD" for wind speed, "No" for filtered, and "Rc" for reconstructed. See text for detailed description of each experiment.

Group	Model Runs	Forcings	Space Ramping	Time Ramping	Study Purpose
A	MR	air temperature, radiative flux, and humidity from ERAI; wind from CCMP; rain rate from ERAI before 1998, from TRMM since 1998	None	None	Model/data comparison
A & B	RcWIND	wind speed and stress re-constructed for high wind period of TC1 and TC2	2 times of 35-kt radius	None	Model/data comparison and effect of wind
B	NoWIND	wind speed and stress filtered for TC1 and TC2	70°E-75°E, 105°E-110°E, 0°-5°N.	Before TC1 and after TC2	Wind processes (mixing, transport, fluxes, etc.)
B	NoRAIN	precipitation filtered for TC1 and TC2	70°E-75°E, 105°E-110°E, 0°-5°N	before and after TC2	Effect of rain
B	NoRAD	radiative fluxes filtered for TC1 and TC2	70°E-75°E, 105°E-110°E, 0°-5°N	before and after TC2	Effect of radiation
B	NoTC	all the forcings filtered for TC1 and TC2	70°E-75°E, 105°E-110°E, 0°-5°N	before and after TC2	Total TC effects
C	NoWSTR	wind stress filtered for TC1 and TC2	70°E-75°E, 105°E-110°E,	Before TC1 and	Wind processes (mixing, transport,

			0°-5°N.	after TC2	etc.)
C	NoWSPD	wind speed filtered for TC1 and TC2	70°E-75°E, 105°E-110°E, 0°-5°N.	Before TC1 and after TC2	Wind effect on surface heat flux

An experimental run, referred to as RcWIND, is performed branching from the MR solution on 10/11, 1999 by forcing HYCOM with the reconstructed winds (Section 2.3), because the maximum wind speed in CCMP and ERAI products is only ~20 m/s during TC1 and TC2 and may significantly underestimate the TC effects on mixing, entrainment and advection. The RcWIND experiment is the same as in the MR, except that RcWIND is forced by the reconstructed wind field for TC1 and TC2. To further quantify the effects of winds and other forcings (i.e., radiation, precipitation, air temperature and humidity), another suite of diagnostic experiments (EXPs) is performed branching from the MR solution also on 10/11, 1999 by forcing HYCOM with the TC-removed forcing fields (see Section 2.4.2 below) during the two TCs' periods (Table 2.2). While the seven EXPs and MR have the same values before 10/11 in 1999, the differences between the MR and EXPs solutions afterwards provide quantitative estimates of the effects of TC-associated forcing fields.

The model runs are divided into three groups, according to their purposes. Group A (MR and RcWIND) contains control runs and is used to compare with the observations (see Chapter 3) and other experiment results. Group B (NoWIND, RcWIND, NoRAIN, NoRAD and NoTC) is designed to examine the effects of wind, rain, radiation, and other forcings on surface heat flux and OHT. Group C (NoWSTR and RcWSTR) is specifically designed to investigate the effects of wind stress. Each of the EXPs has certain filtered or reconstructed forcing fields (Table 2.2). In EXP NoWIND, NoRAIN, NoRAD, NoWSTR and NoTC, HYCOM is forced by 8-day

low-pass filtered wind (wind stress and wind speed), filtered rain, filtered radiation, filtered wind stress, and the whole set of filtered surface forcings, respectively, during the 10/11 00Z-11/7 06Z period in 1999. All the surface forcings in the EXPs are the same as in the MR otherwise. Note that NoWIND and RcWIND represent the experiments in which HYCOM is forced by filtered wind fields and reconstructed wind fields, respectively, for TC1 and TC2.

2.4.2 TC Signal Removal

TC signals can be filtered out from the forcing fields (i.e., wind, precipitation, shortwave radiation, longwave radiation, air temperature, and air humidity) using a low-pass Lanczos digital filter [Duchon, 1979]. Based on the radii of 18-m/s (~35-kt) winds and translation speeds of the two TCs, the changes in wind direction and strength associated with the storms are found to have a period within 7.5 days over the ocean. Thus, 8 days are chosen to be as the half power point cutoff period for the low-pass filtering to remove the TCs. The filtered forcing fields from 9/22 18Z to 11/25 12Z in 1999 are used to force HYCOM in the experimental runs. Linear ramping is used in time and space to ensure the smooth transition from the unfiltered to filtered fields. For space ramping, the ramping weight is defined as

$$ramp_{space} = \begin{cases} 0 & \text{, if inside the BoB} \\ (x - x_{in})/(x_{out} - x_{in}) & \text{, if in the ramping area} \\ 1 & \text{, otherwise} \end{cases}$$

x_{out} is the outer boundary of the ramping area, and x_{in} the inner boundary. In our study, the ramping area is set to 5 degrees. A similar concept is applied to time ramping, with the ramping time zone set to 4 days. The total ramping weight is

$$weigth = (1 - ramp_{space}) \times (1 - ramp_{time})$$

The surface wind speed (U) in the ramping area and period, for instance, is then defined as

$$U^* = weight \times U' + (1 - weight) \times U$$

The filtering method is successful in removing the vortex wind structure (compare Fig. 2.3a and 2.3b), although there is still minor vortex-like circulation near the TC center after the filtering, which can be largely attributed to the steering flow. The outer most 5-degree ramping area along the lateral boundaries has very little vortex-like circulation (not shown). Surface net solar radiation (SRnet) is treated differently from the other forcing fields to retain the diurnal cycle in solar radiation in the filtered time series. The regular 8-day low-pass filtering normally removes the diurnal cycle in solar radiation, which is *not* a property of a TC; therefore, the targeted time series for filtering should be the percentage of solar radiation that is deducted by the TC. ΔSRnet is defined as the difference between SRnet and the maximum possible SRnet (MaxSRnet) at the time of the day during the filtering period. That is, MaxSRnet has four values, which correspond to the maximum possible SRnet at 00Z, 06Z, 12Z, and 18Z during the period of 9/22 18Z - 11/25 12Z in 1999. The ratio of ΔSRnet to MaxSRnet is then filtered, similar to the other forcings. The filtered time series multiplied by MaxSRnet according to the time of the day forms the new SRnet time series that represents the surface net solar radiation without a TC. By doing this, the TC signal at diurnal frequency is still filtered, because the TC signal is reflected in the ratio of ΔSRnet to MaxSRnet; meanwhile, the solar diurnal cycle is retained so as not to interfere with our analysis when isolating the effect of TC-associated radiation reduction.

Fig. 2.4 shows the examples for shortwave radiative flux and total precipitation rate before and after 8-day low-pass Lanczos filtering for the region of 85°E-86°E, 18°N-19°N. From the top panel, it is clear that the filtering for the percentage of solar radiation that is deducted by the clouds does not suppress the diurnal cycle (dotted line for NoRAD). Instead, it increases the

daily peak values (at 06Z for the BoB) on several days of the filtering period, especially 10/16, 10/17, and 10/29. On the other hand, Lanczos filtering suppresses the abrupt changes of total precipitation rate (bottom panel of Fig. 2.4) and in general decreases the total amount of precipitation during the filtering period. Lanczos filtering in rare conditions may cause the filtered time series of shortwave radiative flux and total precipitation rate to be negative, which is false signal in reality; therefore, a minimum constraint of 0 is imposed on such conditions.

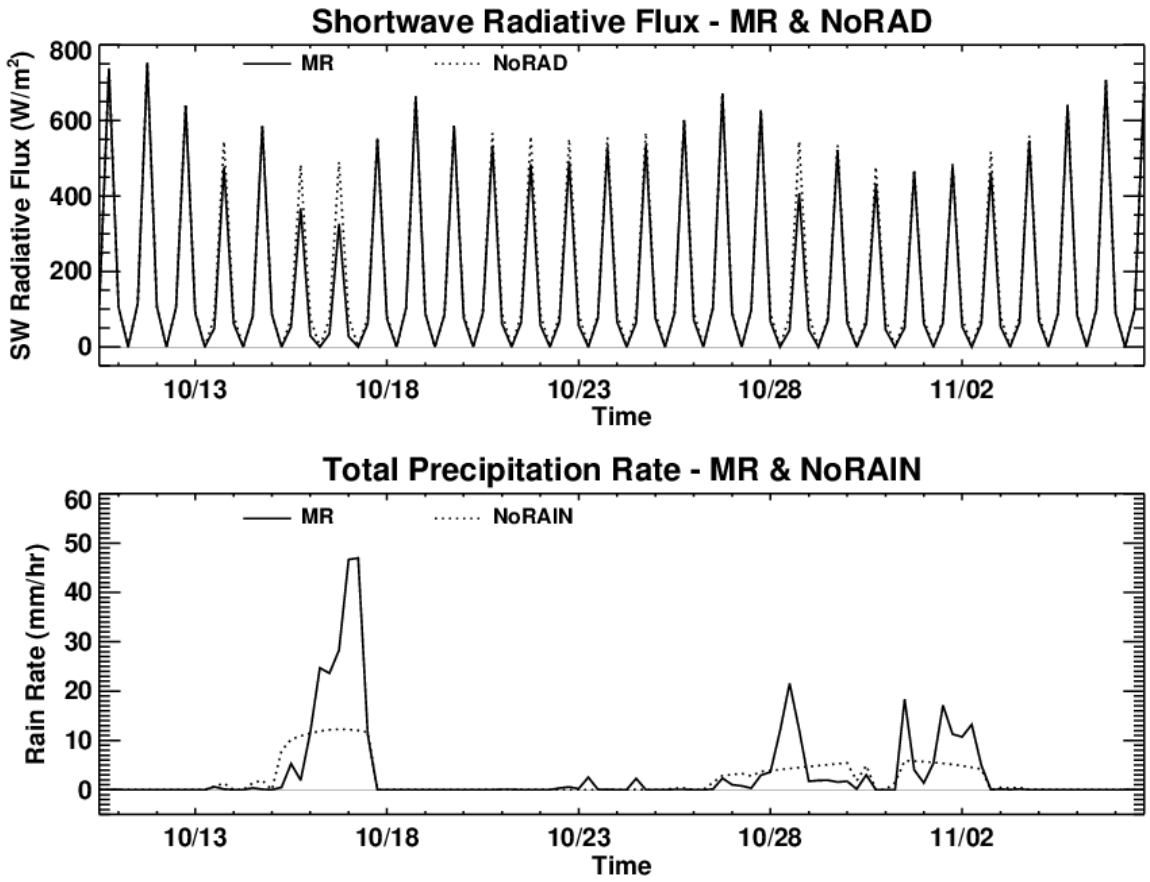

Fig. 2.4: Examples for (top) shortwave radiative flux and (bottom) total precipitation rate before (solid) and after (dotted) 8-day low-pass Lanczos filtering for the region of 85°E-86°E, 18°N-19° N. The filtering for shortwave radiative flux is exerted on the percentage of solar radiation that is deducted by the clouds. See text for details.

2.5 Processes that Affect the BoB OHC

The OHC in our study is defined as OHC= $mC_p(\theta - 26)$, where m is seawater mass, Cp=3990J/K·kg specific heat, and ($\theta - 26$) potential temperature relative to 26°C. The reference temperature, 26°C, is chosen so that the OHC quantity in the upper ocean can reflect TC heat potential [Gray, 1979]. The processes that can change the total (from surface to bottom) OHC in the BoB include surface turbulent heat flux (THF), which is sensible heat flux plus latent heat flux, surface radiative fluxes (shortwave+longwave fluxes), and horizontal heat transport and mixing. The surface net heat flux (NetHF) is the sum of THF and radiative fluxes (NetHF = THF + radiative flux). In HYCOM, surface net radiative flux is a given surface forcing field and lateral boundary temperature is specified near the southern boundary and Indonesian Throughflow region; hence only THF, as an OHC budget component, is not pre-determined and needs to be computed in the simulations.

The sensible heat flux is parameterized in HYCOM with the equation:

$$H = C_{p_{air}}(0.9554E_x)(T_s - T_a), \tag{2.4}$$

where $C_{p_{air}}$ is specific heat of the air, T_s is SST, T_a is temperature in the atmospheric boundary layer, and E_x is an exchange coefficient. A similar equation is used for surface latent heat flux:

$$\varepsilon = E_x L(H_u - E_v), \tag{2.5}$$

where L is latent heat of vaporization, H_u is specific humidity, and E_v is 0.97 × saturated humidity with respect to SST. Exchange coefficient $E_x = \rho_a C_T W$, where ρ_a is air density, C_T is heat transfer coefficient, and W is wind speed. C_T follows the Coupled Ocean-Atmosphere Response Experiment (COARE 3.0) algorithm [Fairall *et al.*, 2003], which is a complex function of wind speed and atmospheric stability and increases with wind speed up to 40m/s. Thus, E_x and

THF both increase with wind speed, unless the temperature and humidity gradients between the sea and air are zero.

Strong winds associated with the TCs can affect THF and thus OHC. Fig. 2.5 shows the THF under both unstable (SST is 0.75°C warmer than the 2m air temperature) and stable (SST is 0.75°C colder than the 2m air temperature) conditions [Fairall *et al.*, 2003] for a wide range of wind speed. While wind speed appears to be the strongest factor for changing THF magnitude, lower SST can also significantly reduce the THF to the atmosphere.

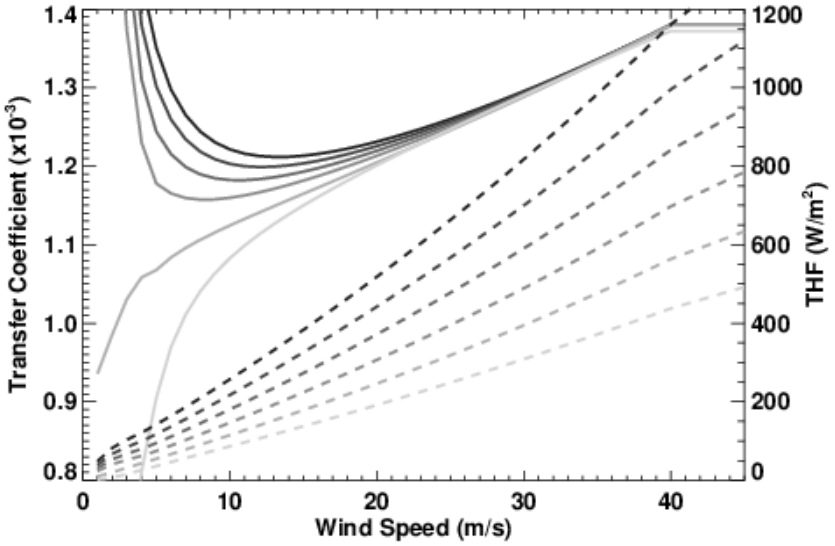

Fig. 2.5: Transfer coefficients (solid) and THF (dashed) curves for SST being 4°C, 3°C, 2°C, 1°C, 0°C, and -1°C (from dark to light) warmer than the air temperature with wind speed from 5m/s to 40m/s and above, assuming 2m air temperature as 26°C, relative humidity as 80% and pressure as 1013mb. The curves are produced based on COARE 3.0 algorithm [Fairall *et al.*, 2003].

TC-associated winds can induce upper-ocean mixing and DOHP, potentially altering ocean circulation and affecting OHT. Mixing in the ocean interior in HYCOM is represented by the K-Profile Parameterization (KPP) scheme. Mixing is triggered when gradient Richardson number $Ri_g < 0.7$, which is defined as

$$Ri_g = \frac{N^2}{\left(\frac{\partial \overline{u}}{\partial z}\right)^2 + \left(\frac{\partial \overline{v}}{\partial z}\right)^2},$$

where N is Brunt-Väisälä frequency. Mixing in the surface boundary layer is active from the surface to the depth where bulk Richardson number $Ri_b < 0.15$, which is defined as

$$Ri_b = \frac{(B_r - B)d}{(\overline{V}_r - \overline{V})^2 + V_t^2},$$

where B is buoyancy, d is the depth of the boundary layer, the subscript r denotes reference values, and the two terms in the denominator represent the influence of resolved vertical shear and unresolved turbulent velocity shear, respectively. For the upper Indian Ocean, the velocities that appear in the denominators of both the Richardson numbers are mostly driven by winds. In HYCOM, there is an option of choosing wind speed or wind stress to determine frictional velocity (u*), which in turn determines unresolved turbulent velocity shear. The author chooses the latter, and hence the mixing in KPP scheme mainly depends on wind stress. Strong wind stress transfers momentum to the ocean surface, changes current velocities, and thus may induce vertical shear instability and mixing in the upper ocean.

2.6 Summary

The HYCOM simulations, including the MR and seven diagnostic experimental runs, are designed and performed for the Indian Ocean using 0.25°x0.25° grids and 30 vertical layers. COARE 3.0 algorithm and KPP scheme are used in the HYCOM simulations for THF calculation and vertical mixing implementation, respectively. Near the southern boundary and the Indonesian Throughflow region, the model temperature and salinity are relaxed to the monthly ocean objective analysis product from the Meteorology Office of the UK (Section 2.2.1).

Freshwater inputs from medium to large rivers surrounding the BoB are also included. (Section 2.2.2.4). The MR is driven by satellite-observed winds from CCMP, and radiative flux, air temperature, air humidity, and precipitation from ERAI reanalysis data from 1989-1997, and is continued to February, 2000, with precipitation replaced by the satellite-observed TRMM rain rate (Section 2.2). The above forcing fields are able to capture the observed TC1 and TC2 identified by the IBTrACS data, although the CCMP winds significantly underestimate the maximum wind speeds associated with the TCs (Section 2.1; Fig. 2.1). To overcome this underestimation, the experimental run – RCWIND is performed branching from the MR solution on 10/11, 1999 by forcing HYCOM with the reconstructed winds based on the modified Rankine vortex as in Holland [1980; Section 2.3; Fig. 2.3]. The other six experimental runs are also performed branching from the MR solution on 10/11 by driving HYCOM with the forcings in which TC signals may be retained or removed by Lanczos 8-day low-pass filtering. The model result differences between the MR and EXPs represent the effects of individual TC forcings on the BoB, and will be discussed in Chapter 4 and 5.

Chapter 3

Model/Data Comparisons

3.1 Sea Surface Temperature

The SST changes during TC1 and TC2 from TRMM data show a general "Bay-wide" cooling for TC1 and cooling in the western and eastern Bay for TC2, with the maximum cooling (~ -3°C) occurring at three locations for both TC1 and TC2 (Fig. 3.1, top panels): near the Orissa seashore along the tracks, in the southwestern BoB (10ºN-15ºN 80ºE-85ºE), and in the eastern BoB (east of 94ºN). The spatial patterns of TC-associated cooling are basically simulated by RcWIND (driven by the modified Rankine vortex; Fig. 3.1b and 3.1e) and the MR (driven by the CCMP winds; Fig. 3.1c and 3.1f), albeit with significant differences in some regions. The well-documented rightward skew in the SST response relative to the TC track [e.g., Price, 1981; Jacob *et al.*, 2000] near offshore Orissa can be seen for TC1 in the observations, the RcWIND run and MR (Fig. 3.1a-3.1c). The CCMP winds that include the TCs are much weaker than the best estimates in the IBTrACS or NRL warnings, and therefore the SST decrease near Orissa is much weaker in the MR than in RcWIND, especially for TC1. Evidently, TC2 cools the SST less than TC1 (category 4), even though TC2 (category 5) is stronger (see Section 2.1), which is likely due to the initial SST depression by the occurrence of TC1.

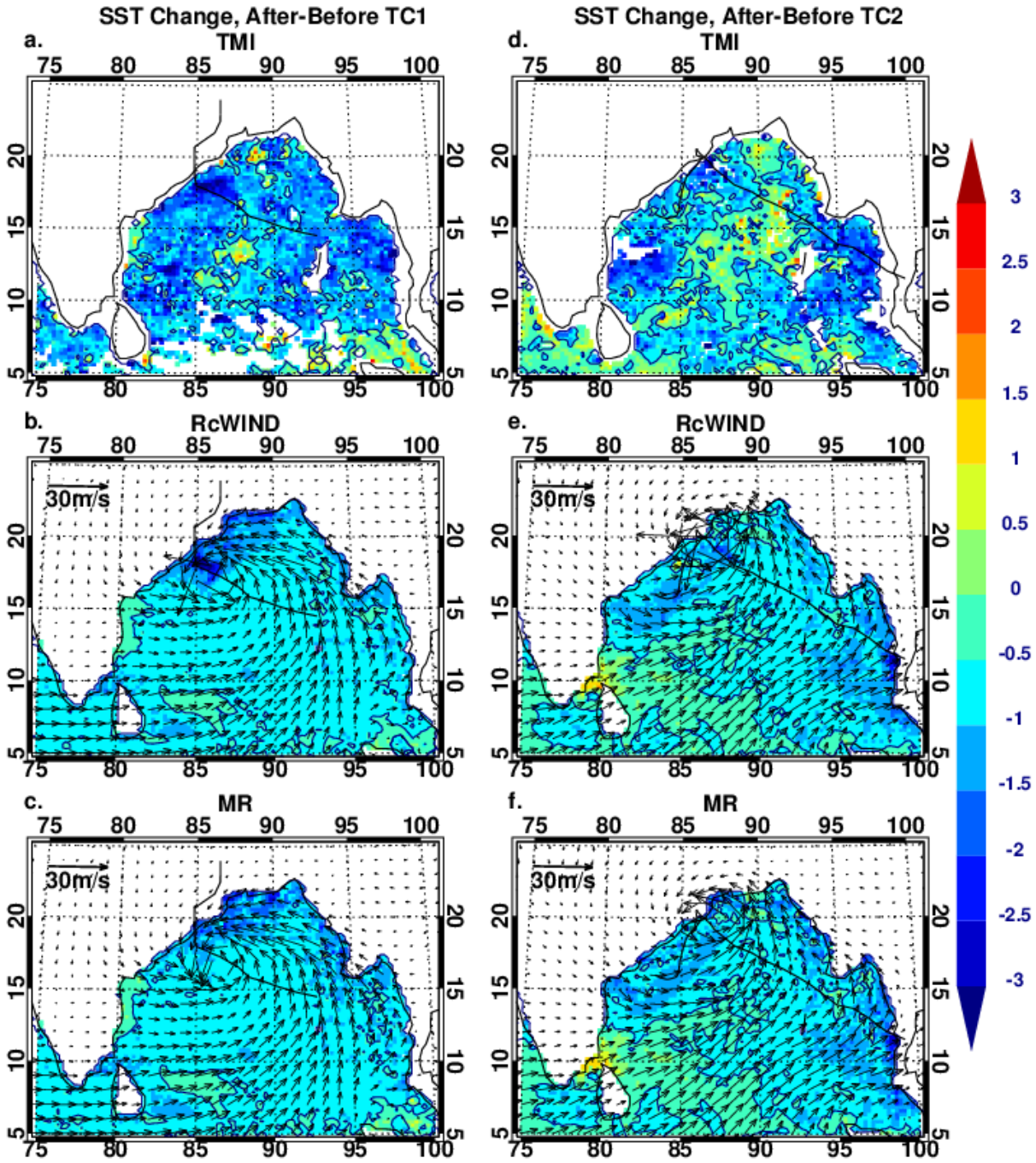

Fig. 3.1: SST differences between 10/12-10/14 mean and 10/19-10/21 mean (TC1 effect) from (a) Tropical Rainfall Measuring Mission (TRMM) – Microwave Imager (TMI), (b) the RcWIND run, and (c) the MR, and between 11/3-11/5 mean and 10/22-10/24 mean (TC2 effect) from (d) TMI, (e) RcWIND, and (f) the MR. The superimposed black lines are the tracks of TC1 (left column) and TC2 (right column). The winds near the strongest stage (10/17 00Z for TC1 and 10/29 00Z for TC2) of the TCs are also plotted (vectors in the middle and bottom panels). The black contour is for 0°C SST.

Quantitatively, the simulated cooling by the MR and RcWIND is much weaker than the observed cooling in the southwestern and eastern BoB for both of the TC cases, and the weak warming in the central BoB, especially for TC2, is not shown in the model. Several possible reasons may account for the model/data differences. First, TMI measures sea skin temperature, whereas HYCOM SST is from the top slab layer (3m thick), which may partly explain the lesser sensitivity of HYCOM solutions to the TC forcings. Secondly, errors in HYCOM forcing fields will cause errors in the simulated SST. For example, ERAI data may not adequately resolve the spatial variations and amplitude of the radiative fluxes, air temperature and/or specific humidity near the TC centers; the reconstructed winds, although much stronger than the CCMP winds, may not always be physically consistent with other forcing fields. Thirdly, HYCOM's limitations may also contribute to its less sensitive SST response.

Neither the MR nor RcWIND captures the strong SST reduction in the southwestern BoB. Before TC1, TMI shows relatively warm SST (≥31°C) in the southwestern BoB, in contrast to the relatively cool SST (≤28°C) in the south central BoB. TMI data suggest that the low SST in the south central BoB may originate from the mini-cold pool south of the India-Sri Lanka channel (not shown), which is consistent with the findings of Rao *et al.* [2006a, 2006b]. During TC1, the SST in the southwestern BoB is reduced partly by the enhanced surface heat loss caused by the strengthened wind, and partly by the cold advection from the south central BoB. The SST contrast between the two regions is not as obvious in HYCOM as in TMI before TC1; therefore, the cold advection during TC1 is not as strong in HYCOM. The SST decrease in the southwestern BoB during TC2 is caused by a different process. TMI data show that TC2 cools SST along its track before its landfall location and along Orissa shore after it reenters the Bay by strong mixing and upwelling (see Chapter 4 for discussions). The cold seawater is then advected

to the southwestern BoB by the strong counterclockwise current along the coast. HYCOM does not capture the full strength of the SST decrease along the Orissa shore after 10/29 due to the early termination of wind reconstruction period, and therefore does not reduce SST as much in the southwestern BoB by advection as in TMI observations.

3.2 Sea Surface Height

Atmospheric background winds of southwesterly and the strong winds associated with the two TCs along the northern BoB boundary (Fig. 3.2, middle and bottom panels) directly pile up seawater against the coasts and/or cause onshore Ekman transport (direction: 90° to the right of the winds) and thus onshore mass convergence, raising the sea level near the coasts by as much as >18cm in some regions, as shown by the AVISO satellite observed sea surface height (SSH; Fig. 3.2, left column). This sea level signal can propagate counter-clockwise around the perimeter of the Bay, increasing the SSH along the western BoB boundary. Meanwhile, the onshore mass convergence induces mass divergence and sea level fall in the central Bay. In addition, positive Ekman pumping velocity

$$w_e = \frac{\partial}{\partial x}\left(\frac{\tau^y}{\rho f}\right) - \frac{\partial}{\partial y}\left(\frac{\tau^x}{\rho f}\right)$$

associated with the TC winds also favors Ekman divergence and thus sea level fall (see Chapter 5 for details). The observed sea level rise along the coasts and fall in the Bay interior are reasonably simulated by the MR and RcWIND, although the simulated SSH is weaker in amplitude especially in the eastern BoB (right column of Fig. 3.2). Along the TC tracks before they arrive at Orissa, both of the TCs are reaching their strongest stages. The cold SST induced by TC-associated wind near Orissa may also contribute to the sea level fall there.

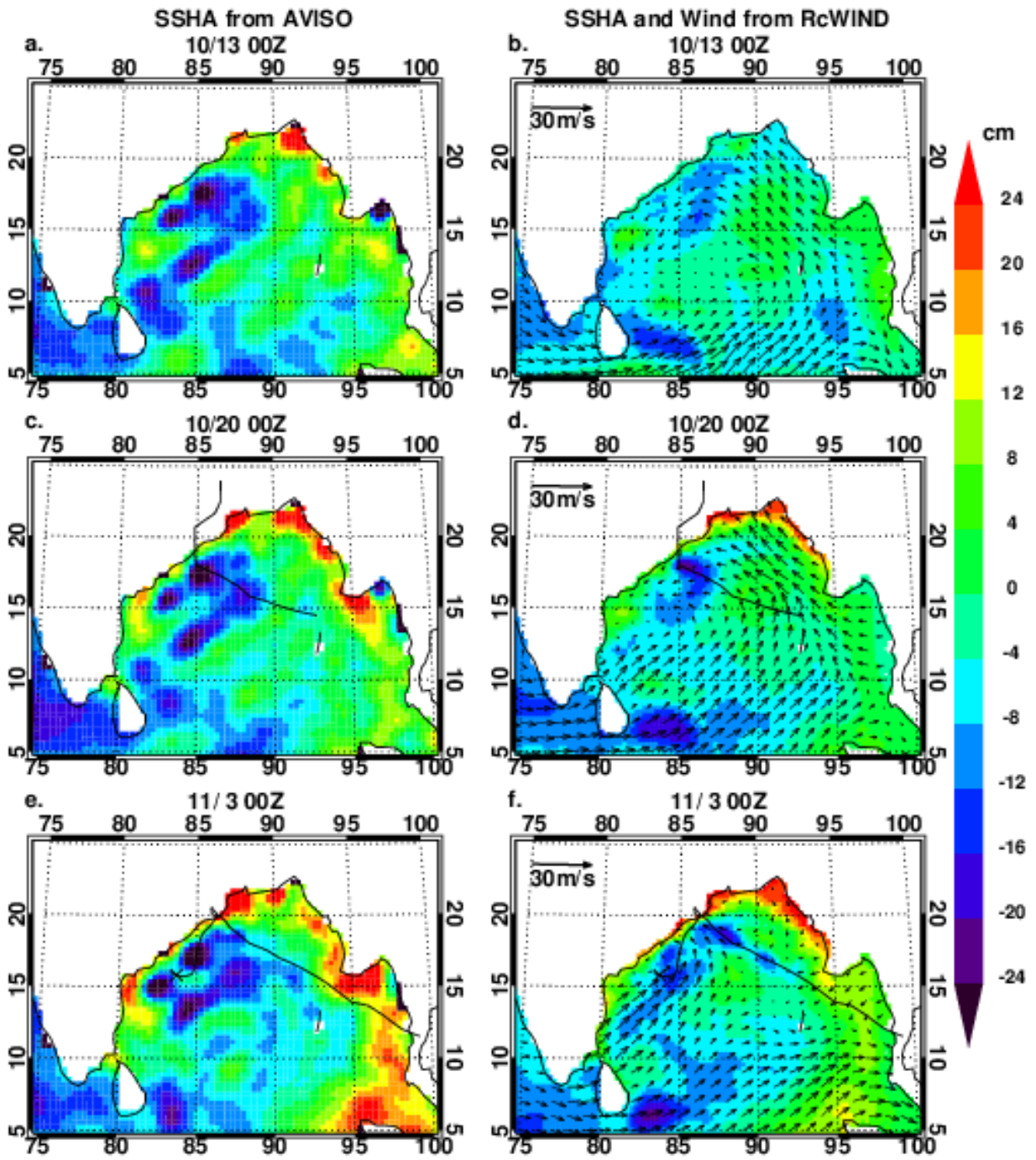

Fig. 3.2: Sea surface height anomaly at three different times from AVISO (left column) and the RcWIND experiment (right column) during the TCs' period. The reconstructed winds for RcWIND are also shown as vectors in the right column.

TC1 exhibits larger SST impacts than TC2, as discussed in section 3.1, whereas TC2 exhibits larger SSH impacts than TC1. TC2 has higher winds and lingers over the ocean longer

than TC1, and hence the onshore Ekman transport and mass convergence induced by TC2 cyclonic wind is more prominent.

3.3 Drifting Buoys and Cruise Profiles

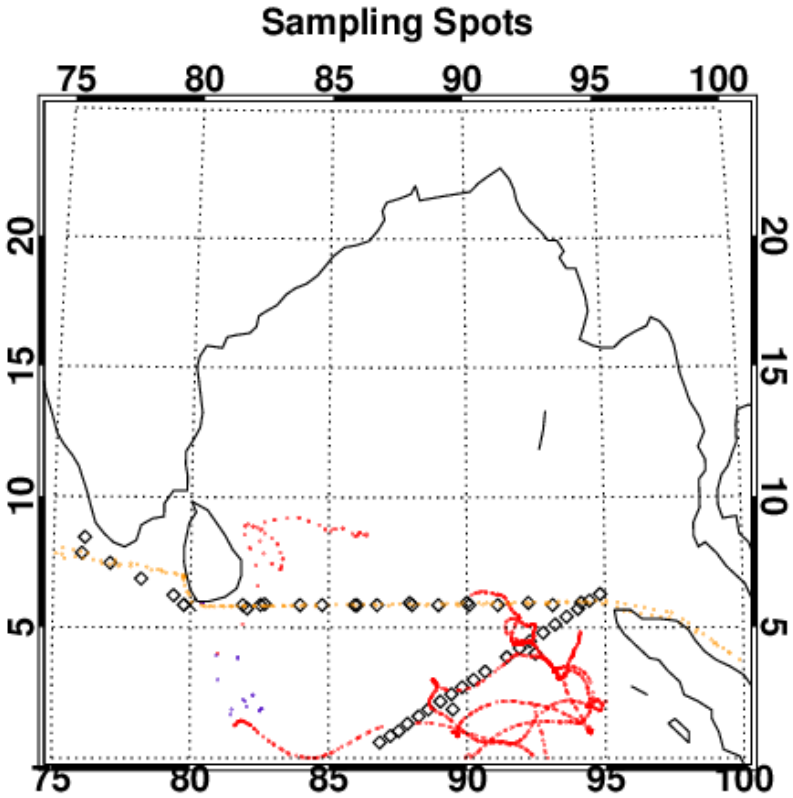

Fig. 3.3: The buoy and cruise sampling locations from October to December, 1999. Red and blue dots represent good quality temperature data by drifting buoys, while brown dots are "unchecked" temperature data. Black diamonds represent cruise campaigns that collect not only surface but also subsurface temperature data. Blue dots are the drifting buoys measurements in the region of 80°E – 82.7°E, 0°N – 5°N after 11/16 in 1999. See text for more description for the purpose of separating blue from red.

The model's skill in reproducing surface and subsurface variability is also evaluated against surface measurements using drifting buoys and surface and subsurface measurements by cruises from October to December, 1999 (Data Source: Department of Fisheries and Oceans Canada, Science Sector, Integrated Science Data Management). Since the sampling locations (Fig. 3.3)

are generally located between the equator and 10°N, the data are used to evaluate HYCOM results along the BoB southern boundary. Unfortunately, there are no *in situ* measurements north of 10°N from October to December, 1999. Argo floats were not yet deployed in the BoB at that time.

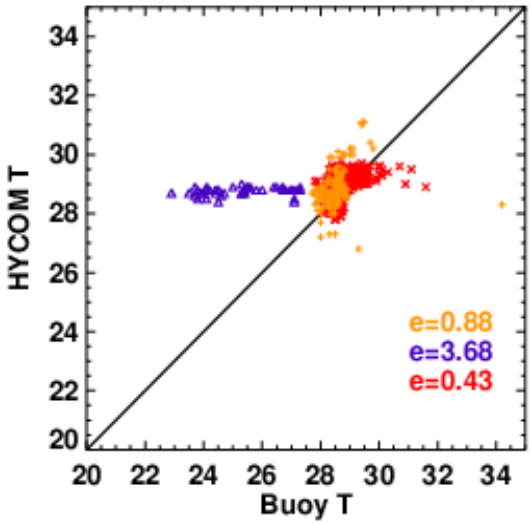

Fig. 3.4: SST comparisons between the MR results and drifting buoy observations. Blue triangles are for the data in the region of 80°E – 82.7°E, 0°N – 5°N after 11/16 in 1999, red crosses are for the data when measurements have good quality and not classified as blue (see text for explanations), and brown crosses for "unchecked" measurements. The numbers shown on the lower right portion of the Figure are standard errors. The RcWIND results are very similar to those of the MR.

The MR SST compare favorably with the high quality buoy observations (standard error=0.43°C), with SST values from 27°C to 30°C (red crosses in Fig. 3.4). The SST and subsurface temperature from RcWIND are similar to those of the MR, indicating that the reconstructed high wind speeds near the center of the TCs, which are used to drive RcWIND, do not have strong influence on upper ocean thermal structure outside the BoB. In the region of 80°E – 82.7°E, 0°N – 5°N during 11/16 – 12/31 in 1999, the MR SST (blue dots in Fig. 3.3 and blue triangles in Fig. 3.4) and TMI observed 3-day mean SST are both generally above 27°C,

much higher than the buoy observations; by comparing with TMI SST, the author has less confidence in the buoy data quality for this location and time.

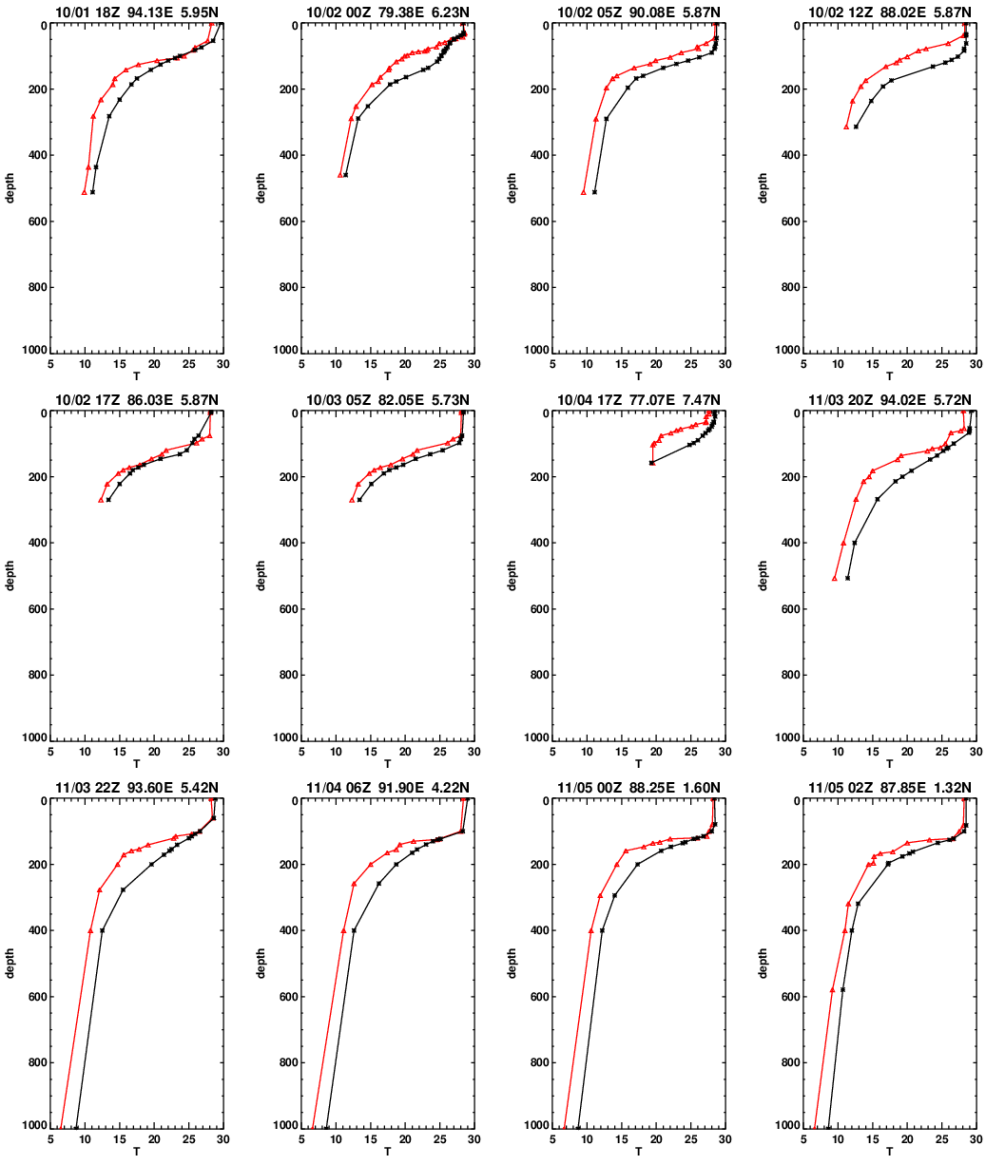

Fig. 3.5: Temperature profiles from cruise observations (red) and from HYCOM RcWIND (black). The MR and RcWIND have almost identical temperature profiles from the equator to 10°N. Only 12 out of 47 temperature profiles are shown to demonstrate the model skill from 76°E to 96°E at every 2° interval (Fig. 3.3, black diamonds) during October – November, 1999.

HYCOM reasonably simulates the ML temperature and depth except for a few locations in

early October 1999 (Fig. 3.5). TC1 starts from 10/15 and ends on 10/19, while TC2 starts from 10/25 and ends on 11/3. Therefore, the profiles in Fig. 3.5 show comparisons before, during and after the TC events. ML temperatures and depths in HYCOM generally agree with the observations very well. HYCOM simulations, however, have weaker vertical temperature gradient in the thermocline layer, suggesting that HYCOM produces a more diffusive thermocline than the observations. Indeed, if the number of vertical layers is increased from 22 to 30, the simulated thermocline is improved (not shown). The ML depth is generally shallower than or near 100m, depending on locations and seasons, while the thermocline layer is usually between 100m to 300m.

3.4 Summary and Discussion

In this chapter, the experiment results using an eddy-permitting ocean general circulation model – HYCOM for examining the impacts of two consecutive TCs on the BoB upper ocean during October-November 1999, are compared with available satellite and in situ observations. The implications of these results for the BoB heat budget will be examined in Chapter 4.

Solutions from the HYCOM MR and RcWIND run with enhanced TC winds reasonably reproduce the upper ocean thermal structure and SSH in the BoB compared with cruise and satellite observations, albeit with quantitative model/data differences. HYCOM simulations, however, exhibit weaker vertical temperature gradients in the thermocline layer, suggesting a more diffusive thermocline in the model than in the observations. The strong SST reduction (~ -3°C) near the Orissa seashore along the tracks and on the right is shown in RcWIND. Compared to the TMI observations, the contrast between the high SST in the southwestern BoB and low SST in the south central BoB during TC1 is less evident in RcWIND and results in weaker cold

advection from the south central BoB to the southwestern BoB. Also, RcWIND produces weaker SST reduction in the eastern and southwestern BoB during TC2, possibly due to the lack of enough information for TC wind reconstruction in the two regions. TC2 (category 5) generally cools the “Bay-wide” SST less than TC1 (category 4) likely due to the initial SST depression by TC1. On the other hand, the onshore Ekman transport and mass convergence induced by TC2 cyclonic wind is more prominent because of the stronger winds and longer lifetime than TC1 over the ocean.

Chapter 4

Impacts of the Orissa TCs on the BoB heat budget: Processes

The impacts of the two 1999 TCs on the BoB DOHP, OHT and the associated physical processes are examined in Section 4.1. The DOHP estimated from the existing methods and from HYCOM simulations for TC1 and TC2 are compared in Section 4.2. Finally, the downward penetration of the two TCs effects and their impacts on the BoB heat potential are discussed in Sections 4.3 and 4.4.

4.1 Impacts of TCs on the BoB OHC Budget: Relative Importance of Wind, Precipitation and Radiation Forcing

4.1.1 Seasonal cycle of BoB OHC

Before analyzing the TC effects on the BoB OHC budget, it is essential to examine the seasonal cycle of the BoB OHC as the background variability. The total OHC of the BoB from the MR experiences relatively small perturbation ($< 150\times10^{18}$J) from mid-October to early November in 1999 that covers the durations of TC1 and TC2, and a major increase ($> 1{,}100\times10^{18}$J) from early November to late December after the TCs (Fig. 4.1a). The total OHC stays high during January and February of year 2000. The NetHF accumulation (i.e., integration over time) north of 10°N acts to reduce the OHC rather than increase it, as shown by the quick decrease of NetHF from mid-November to mid-January. This is because the warm SST and cool air temperature associated with the winter monsoon cause turbulent heat loss, which exceeds the declining net radiative flux (not shown), resulting in negative NetHF. The OHC increase, therefore, results primarily from the seasonal, northward meridional OHT accumulation across

10°N integrated from the surface to bottom, a result that is consistent with previous studies [Wacongne and Pacanowski, 1996; Lee and Marotzke 1998; Webster *et al.,* 2002]. The meridional OHT accumulation across 10°N rapidly increases from 0 to ~1,600×10^{18}J from early November to late December in 1999.

4.1.2 TC-induced OHC change

The total OHC differences between the MR and the series of EXP runs isolate the impacts of wind, precipitation, radiation and other forcings associated with TC1 and TC2 on OHC variations (Fig. 4.1b). The TCs dramatically reduce the BoB OHC from 10/15-11/5 when they pass the BoB, and the BoB OHC slowly recovers afterwards (MR–NoTC and RcWIND–NoTC; purple and black curves). The reduction of the OHC results primarily from TC-associated wind (MR-NoWIND and RcWIND-NoWIND; green and red curves) and radiation (MR-NoRAD; gray curve). The effect of precipitation (MR-NoRAIN; yellow curve) is small, compared to wind and radiation. The total effects of TC1+TC2 are comparable to OHC seasonal variations before mid-November, 1999, when the seasonal variations are weak (compare Fig. 4.1a and 4.1b). Although gradually recovering, the BoB OHC loss due to the TCs remains about -37×10^{18}J from MR-NoTC and about -30×10^{18}J from RcWIND-NoTC by the end of February, 2000. By examining the purple line (MR-NoTC) in Fig. 4.1b, TC1 (10/15-10/19) is shown to reduce the OHC by ~70×10^{18}J before TC2's (10/25-11/3) emergence, while TC1+TC2 reduces the OHC by ~145×10^{18}J three days after TC2's dissipation. Both TCs are responsible for the negative OHC anomalies in early November.

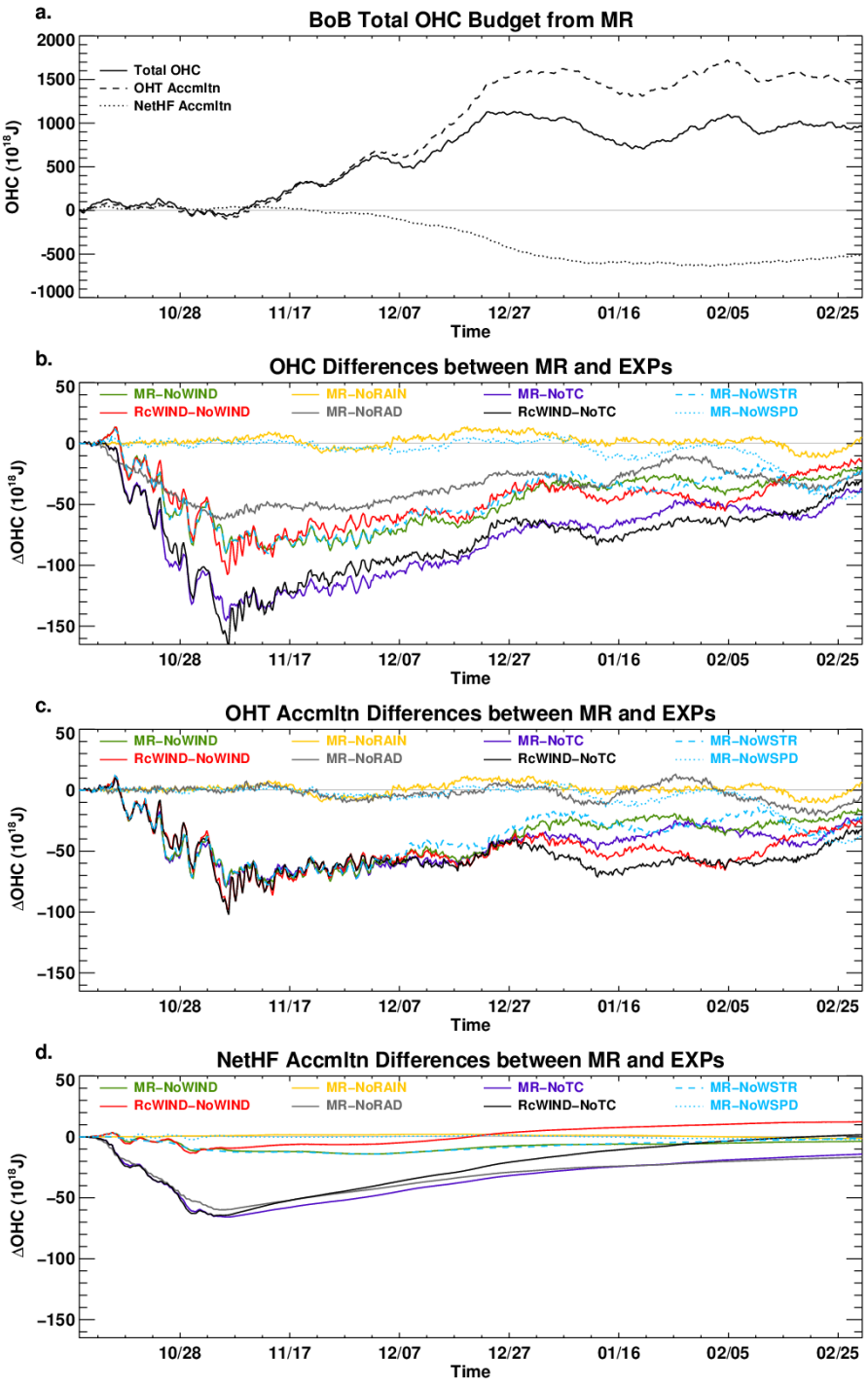

Fig. 4.1: a) Temporal variations of the BoB OHC, which is the OHC integrated over the region north of 10°N for the entire water column, together with the temporarily accumulated NetHF and meridional OHT from the MR; b) the differences of OHC between the MR and EXPs for the BoB; c) same as b) but for the differences of meridional OHT accumulations; d) same as b) but for the differences of NetHF accumulations. OHT is defined as the meridional heat transport across 10°N into the BoB, and is calculated as the residual of OHC change subtracting NetHF accumulation.

4.1.3 Contribution of TC-induced OHT to OHC

The BoB OHC loss results from both the NetHF loss and southward OHT anomalies induced by TCs (Fig. 4.1c and 4.1d). The model results show that the TC-associated winds are the dominant factor that affects the OHT (Fig. 4.1c, compare the green and red with purple and black curves). Of particular interest is that instead of producing a northward OHT anomaly that compensates the NetHF loss, the TCs induce a southward OHT anomaly, which significantly contributes to the OHC loss. This is because the CCMP winds for the MR alter the currents, which transport the warmer ML water southward out of the BoB along the western boundary and transport the cooler ML water northward into the southeastern BoB (not shown). The background seasonal OHT from mid-October to early November is usually positive northward, and the effect of the TCs on the OHT is a transient phenomenon during the transition period from summer to winter.

Previous model results have shown that TC-induced vertical mixing leads to DOHP into the thermocline, which can influence transports and energetics of circulation patterns, such as the subtropical cells and gyres [Jansen *et al.*, 2010; Sriver *et al.*, 2010; Sriver and Huber, 2010; Fedorov *et al.*, 2010; Manucharyan *et al.*, 2011]. The HYCOM results suggest that in the BoB, TC winds can directly influence the wind-driven circulation, leading to increased southward OHT out of the BoB on relatively short (e.g. weeks to months) time scales via changes in the near-surface currents. The implications for longer time-scale background circulation patterns in the BoB remain unclear and require further investigation.

After the TCs pass the BoB, the accumulated (i.e., time-integrated) southward OHT anomaly induced by the TCs start to weaken after mid-November (Fig. 4.1c), consistent with

previous studies. However, the TC-induced anomalous OHT does not completely disappear even during February 2000, indicating that the two TCs induce BoB net heat loss. Surprisingly, the reconstructed strong winds (RcWIND) do not have an apparent additional impact on the accumulated OHT, compared to the CCMP winds in the MR throughout the period of interest. The 18-m/s (35-kt) radii of TC1 and TC2 are usually smaller than 220km (~120 nautical miles), and the effective range of the reconstructed wind only reaches 2 times of the radii (see Table 2.2 and Section 2.4.2 for space ramping). Given that the TC winds are reconstructed only when the TC centers are located to the north of 14°N, the reconstruction does *not* alter the wind pattern near 10°N (see Fig. 2.3 and Fig. 3.1). Thus the meridional OHT across 10°N of RcWIND has similar strength and variability as that of the MR.

The effects of TC-associated precipitation and radiation on the accumulated meridional OHT across 10°N are small (MR-NoRAIN and MR-NoRAD; yellow and gray curves in Fig. 4.1c). The weak precipitation effect differs from the Hu and Meehl [2009], likely due to the persistently strong stratification in the BoB where strong monsoon precipitation and fresh water input from surrounding rivers make the BoB one of the freshest places in the world's oceans. Consequently, TC-associated precipitation may not alter the stratification much, which may be a unique feature of the BoB, in contrast to Hu and Meehl [2009] who examined the Atlantic Ocean.

4.1.4 Contribution of TC-induced NetHF to OHC

The TC-induced accumulated NetHF differences (Fig. 4.1d) represent the impacts of the TC-associated forcing fields on air-sea heat exchange. Post-storm surface fluxes are important, because they contribute to restoring cold wakes caused by the TCs (via mixing and surface

cooling in the BoB). Here the modeled NetHF is used to estimate the amount of DOHP associated with TC1 and TC2, by examining surface heat flux differences during and in the months following the TC events. As discussed in Section 1.2, DOHP is defined as the amount of heat mixed irreversibly into the thermocline, thus representing a net oceanic heat convergence. Previous efforts have attempted to quantify DOHP by examining cold wakes using surface observations and assuming they represent homogenized cold anomalies compared to pre-storm conditions, which enables estimation of the amount of heat lost from the upper ocean through vertical mixing [Sriver and Huber, 2007; Sriver *et al.*, 2008]. This technique neglects the heat flux to the atmosphere during the TCs, which is suggested to contribute 15~20% of TC-induced SST reduction [e.g., Price, 1981; Black, 1983]. In this dissertation, the DOHP effect is estimated by analyzing post-storm accumulated NetHF that acts to restore the storm-induced upper-ocean cold anomaly. The accumulated NetHF differences among the model simulations are directly calculated (see Table 2.2) to diagnose the effect of TC-associated forcing fields on ocean surface heat budget. By analyzing the post-storm accumulated flux differences between HYCOM simulations, rather than comparing post-storm versus pre-storm conditions, the previous inherent assumptions about the dominance of mixing over surface heat fluxes in cooling the SST are avoided. Moreover, it allows us to estimate the significance of post-storm surface fluxes for cold wake restoration for the TCs and the seasonal variation of atmospheric and oceanic conditions following the TCs., which has been hypothesized to be important for understanding how TCs impact oceanic heat budgets. The accumulated NetHF difference between RcWIND and NoTC will then represent the best estimate of DOHP effect in this research.

The accumulated NetHF in the BoB from the different solutions, MR-NoTC and RcWIND-NoTC, have comparable magnitudes to those of OHT (compare Fig. 4.1c and 4.1d).

The TCs induce oceanic heat loss when they pass the BoB from mid-October to early November, and then cause gradual heat gain in the following few months. By the end of February 2000, the NetHF from RcWIND-NoTC (best estimate of total DOHP effect of TC1 and TC2) is approximately 1.74×10^{18}J into the ocean (Fig. 4.1d, black curve). While the net surface heat gain after the TCs is consistent with the DOHP effect proposed by previous studies, the strong heat loss during the TCs is not negligible in the BoB, which is in contrast to assumptions made in previous studies analyzing surface observations. In solution MR–NoTC (Fig. 4.1d, purple curve) the NetHF is still negative and does not completely recover by February 2000. This evident difference demonstrates that the underestimation of TC-associated winds by the CCMP product in the MR underestimates the DOHP effects, as is clearly shown by solutions RcWIND–NoWIND and MR–NoWIND (Fig. 4.1d, red and green curves). Interestingly, the NetHF loss during the TCs are dominated by the radiative flux forcing, whereas the strong TC winds play an important role in generating the eventual net heat gain near the end of February (compare the black, gray and purple curves in Fig. 4.1d). Convective clouds associated with the TCs reduce the shortwave flux (not shown) and induce the negative NetHF anomaly, cooling the ocean when they pass the BoB. This cooling gradually recovers after the TCs' passage, because the colder SST (Fig. 4.2c) reduces the THF loss. By the end of February, the accumulated NetHF due to radiative flux forcing is approximately -17×10^{18}J.

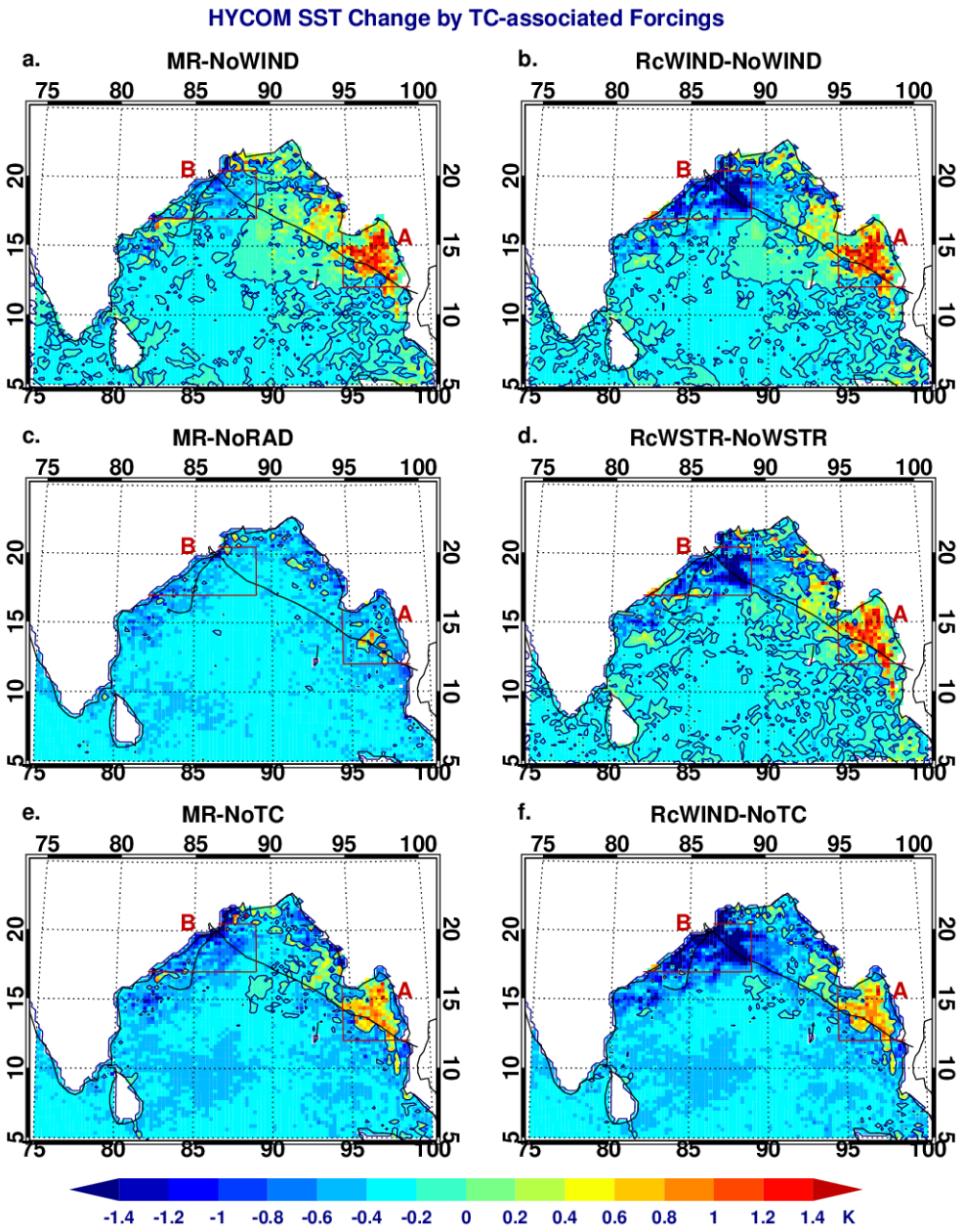

Fig. 4.2: a) SST difference between the MR and NoWIND for 11/3 mean; b), c), d), e) and f) are similar to a), but for the differences between RcWIND and NoWIND, between the MR and NoRAD, between RcWSTR and NoWSTR, between the MR and NoTC, and between RcWIND and NoTC, respectively.

Compared to the radiative flux, effects of TC-winds on the BoB-averaged NetHF are weak (Fig. 4.1d, green and red curves). In the HYCOM simulations, wind stress is the major cause for the accumulated THF reduction during the recovery after the TCs, with wind-speed induced THF

being negligible (Fig. 4.1d, compare the green, blue dashed and blue dotted curves). The CCMP wind stress is used in the MR for the entire BoB and in the RcWIND run to the east of 95°E and south of 14°N. The TC-wind stress entrains the warm water below the temperature inversion layer and warms up the SST in the southeastern BoB (see later in this subsection for temperature inversion) in Region A (Fig. 4.2). As a result, THF loss increases in the MR and RcWIND (Eq. (2.4) and (2.5); Fig. 2.5). When the TCs approach Orissa, strong TC winds (~20m/s in the MR and ~60m/s in RcWIND in region B) cool the SST significantly via wind stress, as is seen by the similar SST anomaly patterns and magnitudes in solutions RcWIND–NoWIND and RcWSTR–NoWSTR. The strong wind stress enhances vertical mixing and the cyclonic wind circulation induces upwelling cooling in Region B, resulting in cold SST anomalies. The dominant effects of wind stress and weaker effects of THF due to wind speed on cooling the SST during the TCs' active stages are consistent with previous studies. After the TCs pass the BoB, accumulated NetHF of RcWIND-NoWIND begins to increase because the strong cooling of RcWIND in the northwestern BoB induces a downward THF anomaly, resulting in a net heat gain of $>12\times10^{18}$J at the end of February (Fig. 4.1d, red curve). This effect is counteracted by the warm SST anomaly in the southeastern Bay (Fig. 4.2). These results, combined with the discussion on OHT, demonstrate that TCs indeed have the DOHP effect in the BoB due to both radiative fluxes and strong winds, when the strong TC winds are realistically represented. The pumped heat is transported southward out of the BoB by the oceanic circulation, which itself is enhanced by the TC winds and thus affects the OHT and OHC.

To understand further why the MR-NoTC does not produce the net surface heat gain in February whereas the RcWIND-NoTC run does, the hierarchy of HYCOM solutions is analyzed. While the fresh ocean surface favors barrier layer formation [Lukas and Lindstrom, 1991 and

Sprintall and Tomczak, 1992] and seasonal surface cooling favors the formation of shallow temperature inversion [e.g., Shetye *et al.*, 1996; Han *et al.* 2001; Howden and Murtugudde, 2001; Masson *et al.*, 2002; Vinayachandran *et al.*, 2002; Sengupta *et al.*, 2008] in Region A, which is <25m (green lines in panel A1-A4 of Fig. 4.3), vertical mixing caused by the CCMP winds in both the MR and RcWIND deepens the ML (red and black lines in panel A1-A4 of Fig. 4.3, and Fig. 4.5) and erodes the temperature inversion. Note that the winds are the same for the MR and RcWIND run in Region A. The deeper ML and mixing with the warm water from below in the MR and RcWIND keep the SST in Region A from decreasing, producing the positive SST anomalies, compared to the NoWIND and NoTC experiments (Fig. 4.2). The warm SST anomalies increase the THF loss, which balances or even exceeds the reduced THF loss associated with TC-induced cold SST in other regions (Fig. 4.2), producing a negative accumulated NetHF in solution for MR-NoWIND and impedes DOHP. The strong stratification and temperature inversions make the BoB a place that has weaker DOHP effects associated with TCs. Nevertheless, the model results suggest TCs can still substantially alter OHT in the BoB region through wind-induced changes in the near-surface circulations.

In contrast, in the northwestern BoB the SST is considerably lower in the RcWIND experiment than the MR. This is because the CCMP winds exceed 20m/s in Region B for both TC1 and TC2, while the reconstructed winds exceed 45m/s for TC1 and 65m/s for TC2. The much stronger winds in RcWIND enhance vertical mixing (see the crossing of the red lines and black lines in Fig. 4.3, panel B1 and B2) as well as upwelling (Fig. 4.3, panel B1-B4), and thus cause much colder SST in a large area in the northwestern Bay. The decreased SST reduces THF loss in the following months, which exceeds the increased THF in region A, producing a positive NetHF anomaly in the BoB and DOHP in the RcWIND run.

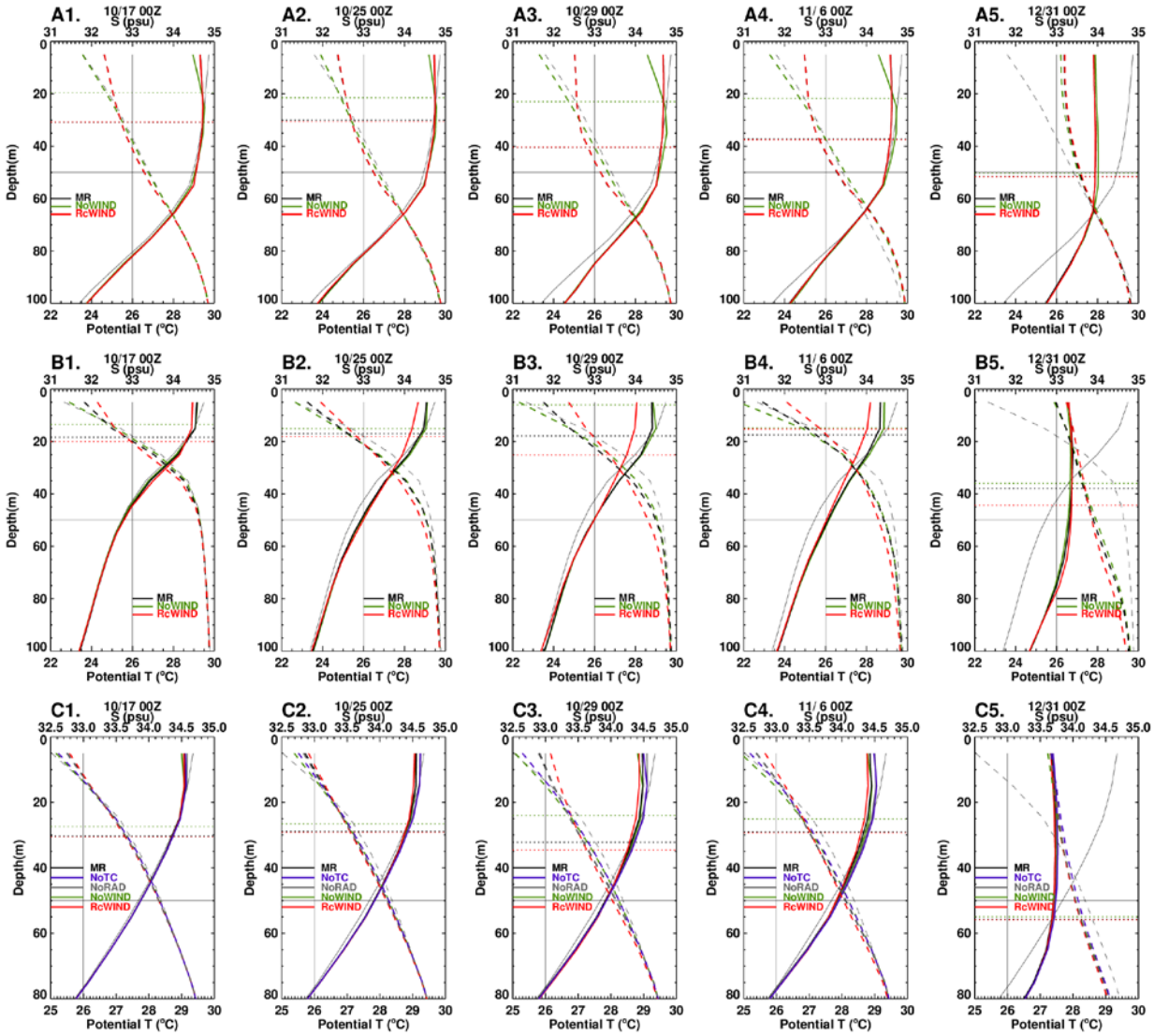

Fig. 4.3: The potential temperature (solid lines) and salinity (dashed lines) profiles during and after TC1 and TC2 for top 100m of Region A (top row), for the top 100m of Region B (middle row), and for the top 80m of the BoB to the north of 10°N. The thin black curves are the potential temperature and salinity profiles at 10/11 00Z, four days before TC1, and thus all the model runs share identical potential temperature and salinity profiles according to the experiment design. The dotted lines show the mixed layer depth for the MR (black), NoWIND (green) and RcWIND (red).

As pointed out in Section 4.1.1, seasonal surface cooling begins in November, when the BoB experiences transition from the summer to winter monsoon. The THF loss is enhanced by the cold and dry air associated with winter monsoon. Meanwhile, the downward solar radiation

declines. Therefore, the temperature in the upper 35m of the BoB dramatically decreases for all the model runs by the end of 1999 (panel A5, B5 and C5 of Fig. 4.3; Fig. 4.1a). After TC2 decreases the BoB SST, the SST actually keeps decreasing in November and December, 1999 and never recovers to its pre-storm value. As a result, one may need to take into account the effect of seasonal cycle, if he/she intends to quantify the TC effects on DOHP using SST values before and after TCs.

To summarize, Section 4.1.3 and 4.1.4 show that the strengthened winds and reduced solar radiation due to TC1 and TC2 are the two dominant forcings that change the BoB OHC. While the reduced solar radiation directly decreases the heat input into the ocean, the strengthened winds enhance southward Ekman transport that carries additional OHC out of the domain. Due to the transition from the summer to winter monsoon starting from November, seasonal surface cooling places a cap on the SST recovery from the TCs' impacts through THF.

4.2 Estimated DOHP based on SST before/after the TCs

Section 4.1.4 shows the estimates of DOHP effect (~1.74×10^{18}J for RcWIND-NoTC in four months) by contrasting the accumulated NetHF from different model runs. In order to better demonstrate the discrepancy between the new method and the previous research works, the oceanic heat convergences by TC1 and TC2 are computed based on the methods described in Sriver and Huber [2007] and Sriver *et al.* [2008] using the mixing depth and SST from RcWIND and compared with observation-based estimates using the same methodology (Table 4.1). Specifically, the oceanic heat convergence is defined using the difference between conditions before and after TCs along the wakes, assuming a uniform mixing depth of 50m [Sriver and Huber, 2007] and climatological mixing depth [Sriver *et al.*, 2008] for the observation-based

estimates.

Table 4.1: The TC effects on oceanic heat convergence (see text) using the method of Sriver and Huber [2007] and Sriver *et al.* [2008] and the data from NCEP, TMI, and HYCOM.

Estimate heat convergence	TC1	TC2
NCEP SST/50m mixing depth [Sriver and Huber, 2007]	1.18×10^{20}J	7.76×10^{19}J
RcWIND SST/50m mixing depth	1.03×10^{20}J	1.24×10^{20}J
TMI SST/climatological mixing depth [Sriver *et al.*, 2008]	8.53×10^{19}J	1.18×10^{20}J
RcWIND SST/RcWIND mixing depth	6.86×10^{19}J	1.16×10^{20}J

The SST from RcWIND and NCEP [Kalnay *et al.*, 1996] estimates roughly equivalent oceanic heat convergence, when mixing depth is presumed to be 50m and footprint is set to $6^{\circ}\times6^{\circ}$ surrounding the TC centers. The oceanic heat convergence estimated by the simulated SST from the RcWIND run is 1.03×10^{20}J for TC1, which is close to the 1.18×10^{20}J estimated from the observed SST as in Sriver and Huber [2007]. For TC2, the heat convergence estimated by the simulated SST is 1.24×10^{20}J, which is 60% larger than the estimate of 7.76×10^{19}J based on the observed SST. In Sriver *et al.* [2008], the mixing depth is set to the depth to where the SST change corresponds to the climatological vertical temperature difference. In other words, the mixing depth is the level from which upwelling must occur to achieve a SST response based on the local climatological vertical temperature profiles. In addition, the NCEP SST is replaced by the TMI SST. Using the same concept, the mixing depth is estimated using the RcWIND run and obtain the oceanic heat convergence to be 6.86×10^{19}J for TC1, which decreases by ~33%, and 1.16×10^{20}J for TC2, which reduces by 6.8%. The new mixing depth on average appears to be shallower than 50m for TC1 in the RcWIND experiment and produces less oceanic heat

convergence. These values are comparable to the Sriver *et al.* [2008] estimates of 8.53×10^{19}J and 1.18×10^{20}J for TC1 and TC2, respectively.

Although using the SST and mixing depth from RcWIND would produce the oceanic heat convergence similar to Sriver and Huber [2007] and Sriver *et al.* [2008], the estimates of oceanic heat convergence for both TC1 and TC2 are much larger than the accumulated NetHF differences at the end of February, 1999 shown in Fig. 4.1d. This is because a) Sriver *et al.* assume that the SST reduction after TCs is caused solely by turbulent vertical mixing, and b) in HYCOM the additional NetHF due to lower SST is not sufficient for full SST restoration back to the pre-storm values. As discussed in the previous section, the reduced downward radiative flux during TC1 and TC2 results in significant decrease of NetHF accumulation and thus decrease of SST, and also cancels out most of the increases of NetHF accumulations that result from the TC-induced low SST after the TCs. Furthermore, the SST cooling induced by TC1 and TC2 never fully recovers to the pre-storm values under the scenarios because of the seasonal transition into winter capping the SST restoration. Also note that the role of OHT in SST variations is not clear and needs more investigation.

The model results demonstrate that the assumption of "negligible NetHF influence during the TCs" appears to be invalid for the BoB. Consequently, the estimated DOHP using observed SST before/after the TCs may significantly overestimate the DOHP effects. While the NetHF influence during the TCs may be minor in other ocean basins [e.g., Price, 1981; Black, 1983], the author suggests considering the global DOHP effect estimate based on the methods of Sriver and Huber [2007] and Sriver *et al.* [2008] as the upper bound of the actual DOHP effect.

4.3 Penetration of TCs' Impacts in the Upper Ocean

To demonstrate the “penetration” of the TC effects into the ocean, the OHC differences between the MR and EXPs are compared for the upper 10m, 50m, 100m, 200m and 400m of the BoB (Fig. 4.4). Note that the 50m depth is used by Sriver and Huber [2007] for estimating the DOHP effects of TCs. In the top 10m (Fig. 4.4a) within the ML (Fig. 4.3), the ocean immediately feels the radiative flux and THF. The OHC differences between the MR and EXPs are small, and are essentially zero at the end of February 2000, indicating that the TCs’ cooling during the TCs can be recovered by the reduced THF loss after TC2.

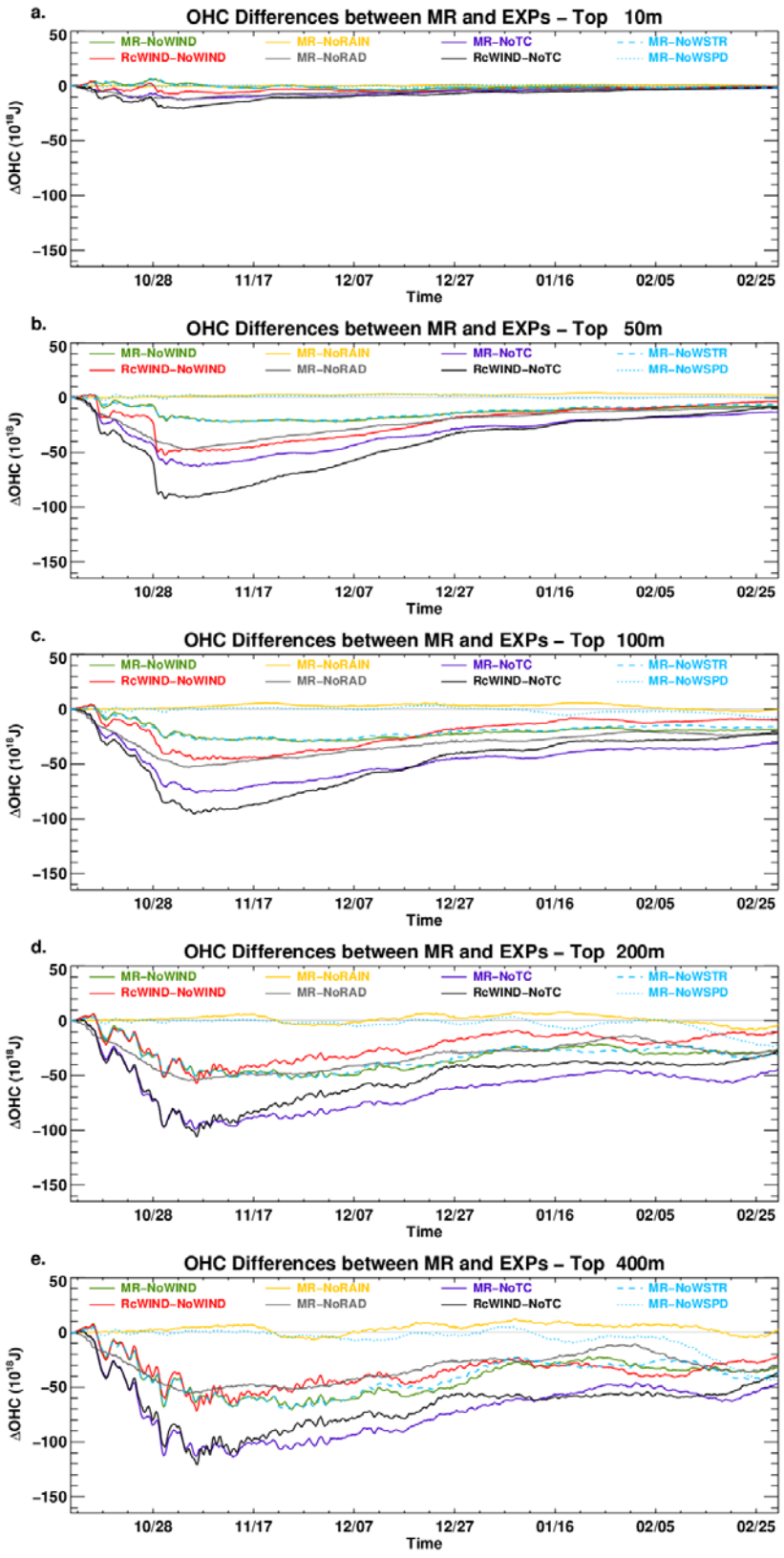

Fig. 4.4: The OHC differences between the MR and a series of EXPs for the top a) 10m, b) 50m, c), 100m, d) 200m and e) 400m in the BoB (north of 10°N).

In the upper 50m of the BoB, the TC-associated wind and radiative fluxes have comparable influences on the OHC (Fig. 4.4b). The wind has direct impact on the top 50m OHC via cooling the upper ocean (bottom row of Fig. 4.3) due to wind-induced mixing and upwelling, which is estimated by the effect of TC-associated wind stress (blue dashed line in Fig. 4.4b). The BoB-averaged ML depth of the MR and EXPs are less than 35m during the TCs (dotted lines, bottom panel of Fig. 4.3), while the penetration of TC-wind effect in the upper 80m is clearly shown in the temperature and salinity profiles (solid and dashed lines in the bottom row of Fig. 4.3). The ML and the thermocline layer exchange mass and heat through mixing and entrainment at the ML bottom, which deepens the ML and thins the deeper layer. The OHC exchanges between the ML and the deeper ocean (below ML) can be identified by the opposite signs and comparable magnitudes of the ML OHC anomalies and their deeper OHC anomalies counterparts (not shown). In the top 80m, vertical mixing induced by wind stress redistributes the OHC vertically.

The CCMP winds in the MR during TC1 (10/15-10/19) and TC2 (10/25-11/3) are stronger than the winds that exclude the TCs in the NoWIND experiment, and hence induce more effective mixing in the upper layer and exchange relatively warmer water in the top 50m with colder water from below (green line in Fig. 4.4b; see also dashed blue line in Fig. 4.4b for wind stress effect), as well as deepen the ML (Fig. 4.5; green solid line for MR-NoWIND) and induce the heat exchange at the bottom of the ML. According to Emanuel [2001], the wind-induced mixing at the bottom of the ML entrains colder water into the ML and at the same time increases the column mass of the ML and warms up the upper thermocline layer. The total column-integrated (surface to bottom) OHC is not changed by TCs if neglecting TC-induced

surface heat fluxes, because OHC is only redistributed vertically. The strong mixing tends to cool and deepen the ML. This process is examined by observing the negative correlation between the ML depth and ML temperature (Fig. 4.5). The MR, however, has higher ML temperature than NoWIND during TC1 and TC2 due to the formation of temperature inversion in the surface boundary layer in NoWIND. The deeper ML in the MR is caused by the TC-wind induced entrainment, and its warmer ML temperature results from entraining the warmer barrier-layer water from below. In the NoWIND run, winds are weaker, SST is lower and temperature inversion forms. The stronger winds in the RcWIND experiment decrease the top 50m OHC even more than the CCMP winds in the MR during TC1 and TC2 (Fig. 4.4b, red line for RcWIND-NoWIND) primarily by reducing the upper-ocean temperature further through entrainment and upwelling (compare the red lines with black lines in panel C1-C3 of Fig. 4.3), reaching a peak value of ~-52×10^{18}J. During TC2, the strong winds in RcWIND also deepen the ML and cool the SST more than the MR (compare red and black dotted lines in the bottom row of Fig. 4.3). The mixing and upwelling signals are induced by wind stress and can be identified by the sudden drops of OHC at the strongest stage of TC1 (10/17 00Z) and TC2 (10/29 00Z) for MR-NoWIND (green), MR-NoWSTR (dashed blue) and RcWIND-NoWIND (red) in Fig. 6b for the top 50m. The reduced OHC gradually recovers. By the end of February 2000, the OHC differences between RcWIND and NoWIND is approximately -3.8×10^{18}J.

The wind effect is also evident in the upper 100m, 200m, and 400m (Fig. 4.4c-4.4e) during TC1 and TC2. The recovery after the TCs at these depths, however, becomes increasingly slower as depth increases, and the TC-induced OHC change near the end of February becomes increasingly negative. The impacts of TCs on temperature and salinity profiles, however, do not have apparent changes below 80m (Fig. 4.3), suggesting the importance of TC-induced

circulation change on OHT and thus OHC in deeper layers. These results, combined with Fig. 4.1, further demonstrate that the total BoB OHC induced by TCs results from both the DOHP in the near-surface layer and storm-induced circulation changes, enhancing the southward OHT below the ML. The similarity of the OHC anomalies in the top 200m and 400m (Fig. 4.4d and 4.4e) suggests that impacts of the TCs on OHC via vertical mixing, upwelling and NetHF are mainly confined to the upper 200m. The TC-induced OHT changes however, can penetrate down to sea floor (not shown) with minor change below 400m.

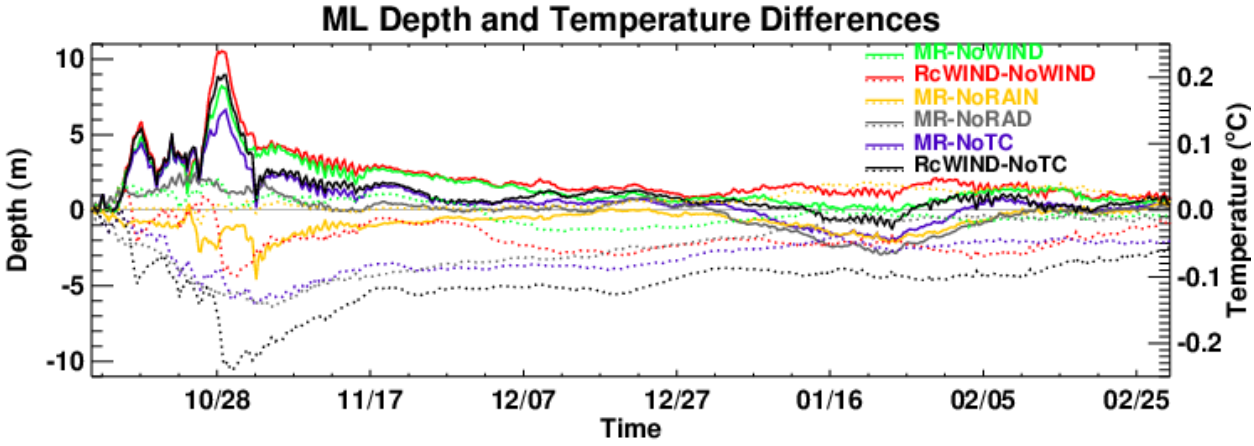

Fig. 4.5: Areal-averaged ML depth (solid) and temperature (dotted) differences between the MR and EXPs.

Comparing Fig. 4.4e with 4.1b and 4.1d, one can see that when considering only wind effect (MR-NoWIND and RcWIND-NoWIND), the TC-induced OHC changes are primarily caused by the anomalous OHT, with wind-induced NetHF playing a minor role. The TC-induced radiative fluxes have comparable effects to winds on the upper-ocean heat content (Fig. 4.4). Although the contribution of the TC-associated radiation to the OHC variations remains identical in the upper 50m-400m, the effect of radiative fluxes on the upper OHC varies somewhat with depth. This is because radiative fluxes can affect SST, stratification and therefore mixing and horizontal

advection, inducing changes in temperature profile (Fig. 4.4 and the bottom row of Fig. 4.3). The combined effects of the TC-associated wind, radiation and precipitation on the OHC can reach ~114x10^{18}J (MR-NoTC) and ~121x10^{18}J (RcWIND-NoTC) in the upper 400m within three days after TC2, and it can reach ~145x10^{18}J (MR-NoTC) and ~166x10^{18}J (RcWIND-NoTC) for the total column at the same time. Consistent with the above analysis, the TC-associated precipitation has little effect on the OHC in the upper ocean. Note that the temperature of the rain is set to be the same as the SST in HYCOM, and hence the TC-associated precipitation does not directly alter NetHF. This may somewhat underestimate the precipitation effect on SST.

4.4 Impacts of TCs on Ocean Heat Potential

The heat potential is defined as the total OHC above the 26°C isotherm. Heat potential is being shown here because it is one of the most important factors for TC development and intensity. The heat potential anomalies can be strongly caused by surface radiative flux differences. The radiation effect (MR-NoRAD) can reach ~20×10^{18}J immediately after TC1 and reach ~53×10^{18}J immediately after TC2. This amount of heat is similar to the TC-induced accumulated NetHF between the MR and NoRAD at the same time (Fig. 4.1d). They also share similar decaying pattern. This indicates that the BoB heat potential is largely determined by the NetHF in the HYCOM simulations.

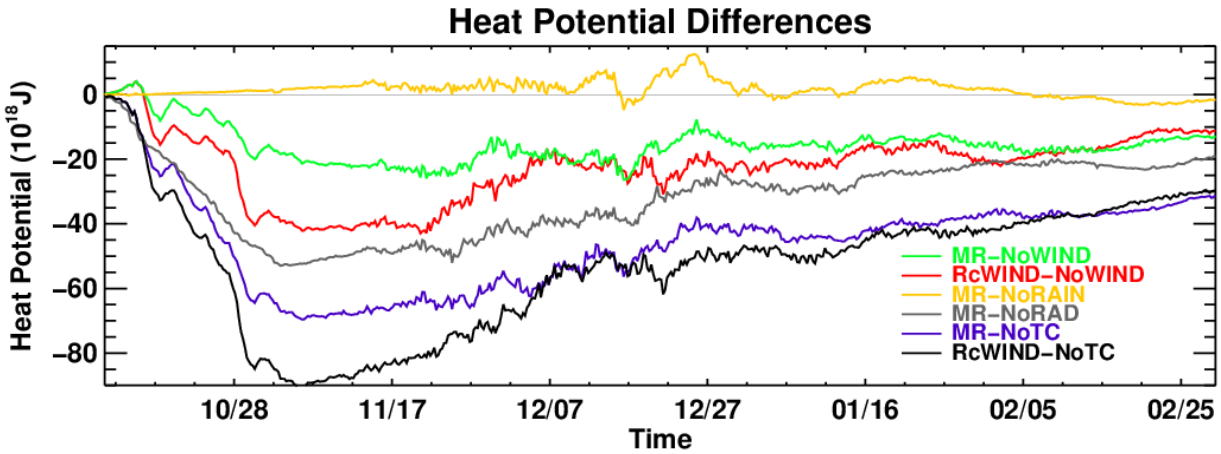

Fig. 4.6: Areal-averaged heat potential of the BoB between the MR and EXPs.

With regard to the wind effect, the BoB heat potential anomalies (Fig. 4.6) are roughly two times of the accumulated NetHF anomalies (Fig. 4.1d) for MR-NoWIND and three times of the accumulated NetHF anomalies for RcWIND–NoWIND immediately after TC2. The behavior of the BoB heat potential change between the three experiments is not similar to the accumulated NetHF in the following four months after TC2. The MR and RcWIND have more surface heat extraction through THF process due to their higher wind speed, compared to the NoWIND run. However, the enhanced THF and thus NetHF process can only partially explain the heat potential response. Vertical mixing is also found *not* to be the main cause for larger heat potential response, because the mixing averaged for the BoB generally happened above the 26°C isotherm (panel C1-C4 of Fig. 4.3). The ML depth in the MR averaged for the BoB approximately ranges from 20m to 35m before December, 1999, increases to ~56m by the end of December, 1999, and decreases to less than 40m by the end of February, 2000. Fig. 4.3 shows that the 26°C isotherm is generally between 75m and 90m and only slightly varies among the EXPs. Hence, the vertical redistribution of OHC caused by mixing does not penetrate to the depth of 26°C isotherm, and the BoB heat potential is only slightly altered by vertical mixing. These suggest that the OHT anomalies induced by the TC-associated wind play a major role in changing the BoB heat

potential.

4.5 Summary and Discussion

The two consecutive TCs (TC1 and TC2) significantly reduce the total BoB (north of 10°N) OHC when they pass the BoB, reaching a peak value of -160 x 10^{18}J in early November after TC2, and the reduced OHC slowly recovers in the following months. The value of OHC change induced by the two TCs is comparable to its seasonal variation from October to mid-November during the monsoon transition period when the seasonal variation is weak, but is only ~10% or less than the OHC seasonal increase during winter monsoon (Fig. 4.1a-4.1b). However, this implies that in a coarse-gridded ocean model that is unable to resolve the impact of TC1 and TC2, the total OHC may be overestimated and SSTs may be systematically too warm for the BoB, compared to that in a high-resolution OGCM.

The reduced BoB OHC during the TCs results from both the southward OHT and reduced downward NetHF anomalies, and both gradually recover in the following months (Fig. 4.1c-4.1d). TC winds are the deterministic factor for the OHT change, primarily by causing anomalous ocean circulation that transports heat out of the Bay. The TC-associated surface radiative flux and winds are the two most influential factors that determine the BoB surface NetHF during TC1 and TC2 and in the following months. The reduced radiative fluxes dominate the wind-induced THF during the TCs, due to the TC-associated clouds blocking downward solar radiation. The accumulated radiation effect quickly decays in November right after the TCs, but remains almost constant with a negative anomaly and never returns to zero from December to February 2000. It is the TC-wind effect that causes the recovery of NetHF to a positive value four months after the TCs. The NetHF input into the BoB facilitates the TCs' DOHP effect. Note that only the enhanced reconstructed TC winds are strong enough to produce the DOHP, by

causing stronger surface cooling during the TCs through mixing and upwelling processes (Fig. 4.1), and thus stronger recovery after the TCs via increased downward THF. Although the CCMP winds contain TC1 and TC2, the winds are too weak to produce realistic surface cooling. Hence the CCMP wind-induced SST reduction is not enough for enhanced downward THF to compensate for the surface heat loss during the TC events.

The weak upward THF induced by TC winds during the TCs, and the strong wind effect during the recovery after the TCs are consistent with previous studies for the Atlantic Ocean. Different from the Atlantic, the model results show large solar radiation effect during the TCs, which compensates for the NetHF recovery after the TCs, producing a weak downward NetHF for a few months after the TCs and making the DOHP effects weak in the BoB. In addition, the effect of TC precipitation has negligible effect of the BoB OHC. These new features are associated with the unique characteristics of the BoB, which is strongly stratified due to monsoon rainfall and large amounts of freshwater input from the BoB rivers. The strong stratification due to fresh waters favors the formation of barrier layer and temperature inversion (Fig. 4.3). As a result, the TC winds entrain warmer water from the barrier layer in the southeastern Bay and thus warm the SST (Fig. 4.2). The warmer SST counteracts the colder SST in the northwestern Bay, causing a weak BoB-averaged downward THF during the recovery period after the TCs.

The weak DOHP effect in the BoB is further investigated by comparing the model results with the estimates of oceanic heat convergence using observed SST based on the existing methods of Sriver and Huber [2007] and Sriver *et al.* [2008]. Using these methods (Section 4.2), the estimated oceanic heat convergence from both HYCOM SST and observed SST obtain similar magnitudes (Table 4.1). However, if including the NetHF loss during the TCs, which is

neglected by the previous studies, the HYCOM simulated time-integrated NetHF during the recovery period suggests a much weaker DOHP effect in the BoB than the observational estimates. In addition, when considering two consecutive TCs that are less than 6 days apart and the seasonal variations, the BoB temperature structure never recovers to its pre-storm condition between the TCs or after. Because the time between the two TCs is too short for the SST to recover via THF process, the impacts of TC2 on DOHP are not as strong as if TC1 did not exist. The seasonal transition from summer monsoon to winter monsoon immediately after TC2 very likely affects the DOHP estimates based on SST before/after the TCs. By observing climatological seasonal variations of SST in the western Pacific and northwestern Atlantic, which can be as strong as in the northern Indian Ocean, the SST recovery in the wakes of TCs in late fall is suspected to be less than storms occurring earlier in the season due to the seasonal cycle. While this point is important for understanding storm-induced changes in surface budgets, a more robust indicator of DOHP is likely to be the amount of heat mixed irreversible into the seasonal thermocline rather than in cold wake recovery. However, estimating the vertical redistribution of heat through vertical mixing is difficult due to the immediate response in the BoB heat transport and near-surface circulation caused by TC winds.

The effects of TCs can affect both the ML and the deeper ocean below. The entrainment at the bottom of the ML and upwelling induced by the wind stress curl are the primary process for OHC exchange between the ML and deeper ocean and cause mirrored changes in OHC. In the deeper ocean below 200m, mixing has little influence on OHC, and the TC wind-induced OHT variations dominates the OHC changes, primarily through causing anomalous ocean circulation. The contribution of the OHT to the OHC change is weak below 400m but keeps accumulating to the bottom of the BoB. The TC-associated rain causes a shallower ML by adding freshwater on

top, and therefore the ML temperature changes faster. In contrast, TC-associated radiation deepens the ML because the reduced solar radiation cools the surface and increases mixing. Regarding the BoB heat potential, TC-associated radiative flux and winds, which drive OHT variations and affect NetHF, are the major causes for the BoB heat potential change (Fig. 4.6).

Chapter 5

Upper Ocean Dynamical Response to TC Forcings

This chapter focuses on understanding the upper ocean dynamical response to TC1 and TC2. The TC winds in the RcWIND experiment induce significant changes in BoB SST (Section 3.1), OHC, OHT, and DOHP (Chapter 4). Apparently, the dynamic response of the BoB plays a major role in determining the BoB OHC budget. In addition, TC-induced sea level variations and surface currents directly impact the coasts. Consequently, it is important to understand the dynamical response of the upper ocean to TC1 and TC2's forcings and the associated processes.

5.1 Impacts of TC1

5.1.1 Upper ocean dynamical response and processes

Short-term SSH variations are almost exclusively determined by wind stress in the HYCOM simulations for TC1 and TC2 (Fig. 5.1; compare the middle column with the right column; middle column for the differences between RcWIND and NoWSTR, and right column for the differences between RcWIND and NoTC). Before TC1 is categorized as a TC (Fig. 5.1a), SSH is generally higher in the eastern half of the BoB, with a low-SSH area in the northwestern BoB offshore Orissa and northeastern Andhra Pradesh of India (83°E-88°E, 16°N-20°N), a relatively high-SSH area offshore eastern Andhra Pradesh (81°E-83°E, 13°N-16°N), and a low-SSH area east of Sri Lanka (81°E-86.5°E, 6°N-9.5°N). On 10/14, geostrophic currents – which flow along SSH contours - dominate surface currents in most of the northern BoB and near the low-SSH area east of Sri Lanka, while Ekman transports, whose directions are 90º to the right of the wind

stress, prevail east of 87°E between 5°N-8°N (Fig. 5.2a). A cyclonic flow appears in Andaman Sea on 10/11 and grows steadily until 10/14 (not shown). Note that the simulated SSH fields in NoTC are essentially the same as in NoWSTR because wind stress is the dominant factor for SSH variations.

The atmospheric background winds in the northern BoB on 10/17 is southeasterly (Fig. 5.1d), which induce Ekman convergence to the coasts and thus increase onshore SSH in the northeastern BoB. The cross-shore SSH gradients near the coastlines of southwestern Myanmar, Bangladesh and northeastern India generate the counterclockwise alongshore geostrophic currents (Fig. 5.2d). Meanwhile, TC1 approaches Orissa, India. The cyclonic wind stress near the TC center induces turbulent mixing and Ekman divergence and thus upwelling (left column of Fig. 5.3), causing cooling of near surface temperature (top 30m; $T_{0\text{-}30m}$). Both the mass divergence and cold temperature cause negative SSH anomaly (SSHA; Figs 5.2e and 5.2f). Because the reconstructed winds are stronger on the right of TC1's track due to the addition of translation velocity to the circular wind, and because TC1 changes its translation direction from west-northwestward to northward on 10/17, it exerts more effect somewhat to the right of the turning point, the areas of negative SSHA (Fig. 5.1d), and cools $T_{0\text{-}30m}$ there (Fig. 5.3d). The temporal evolution of upper ocean temperature and currents that show the effect of near-inertial oscillation [e.g., Price, 1981] will be discussed in Sections 5.1.3 and 5.2.3 below.

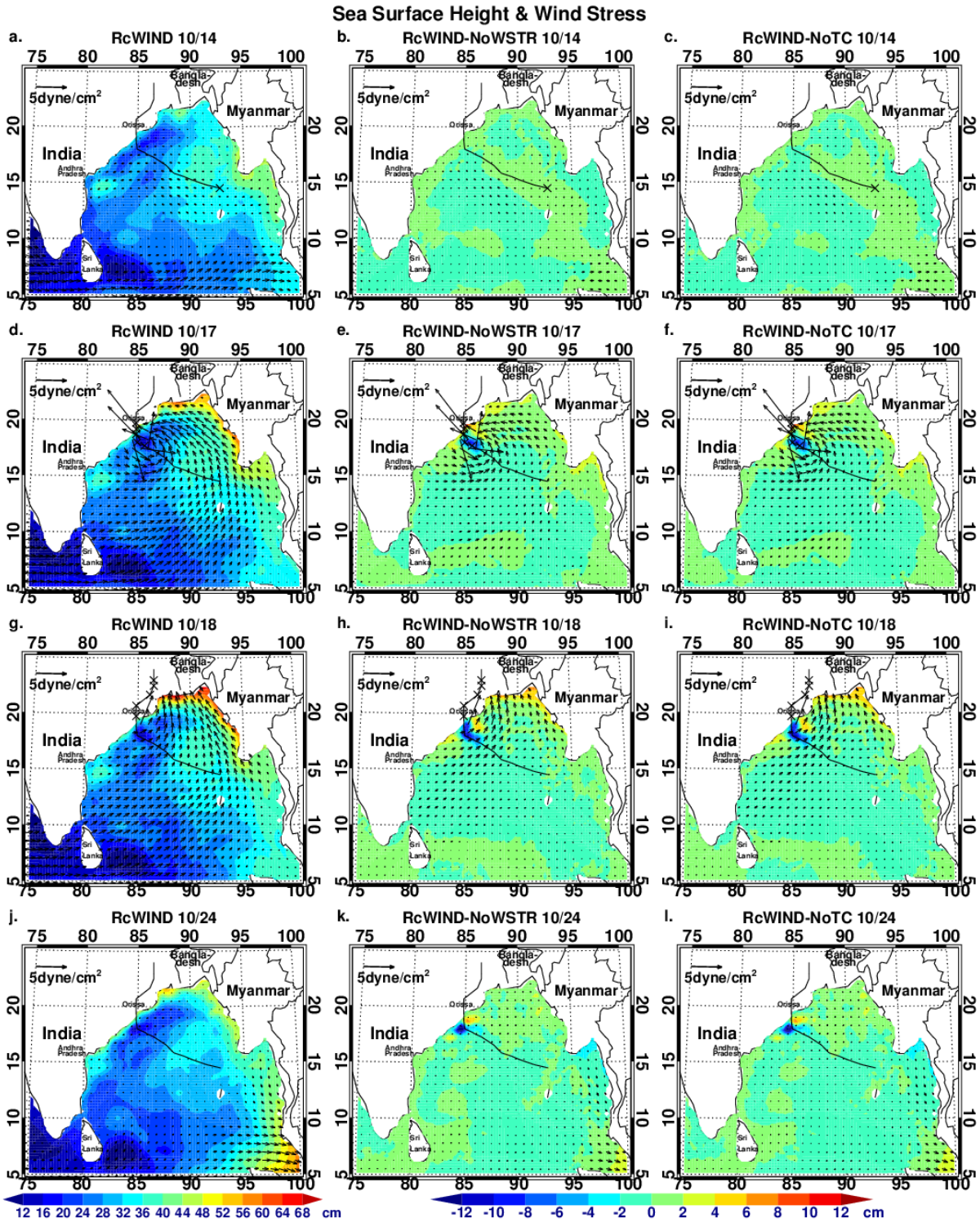

Fig. 5.1: Daily-averaged SSH (color shades) and 10m wind stress (vectors) for RcWIND (left), the differences between RcWIND and NoWSTR (middle), and the differences between RcWIND and NoTC (right) for 10/14, 10/17, 10/18, and 10/21 of 1999. The black line represent TC1's track, and the black crosses represent the locations of TC1 centers every 6 hours from 00Z to 24Z of the day. TC1's strongest stage occurs on 10/17.

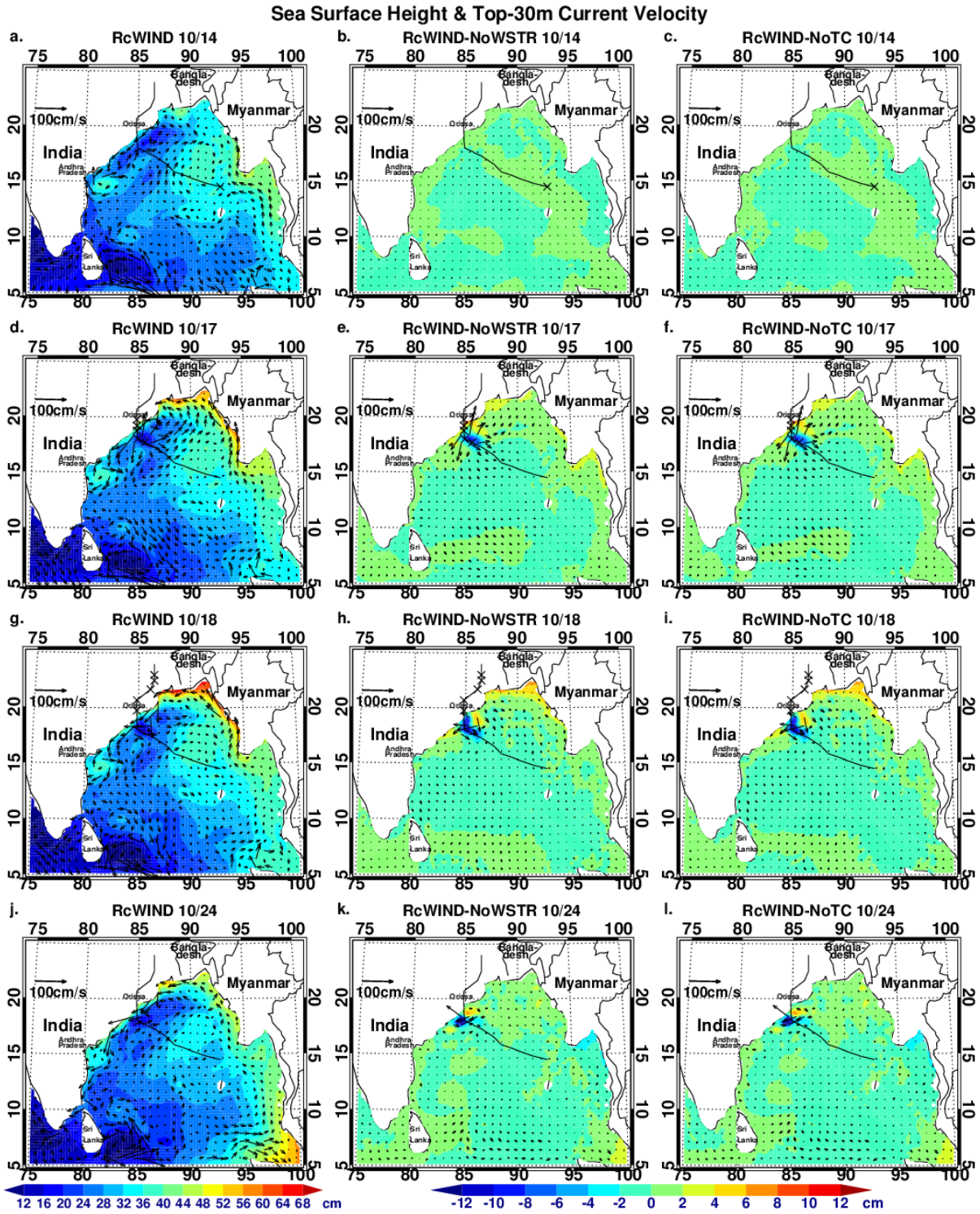

Fig. 5.2: Daily-averaged SSH (color shades) and current velocity in the top 30m (vectors) for RcWIND (left), the differences between RcWIND and NoWSTR (middle), and the differences between RcWIND and NoTC (right) for 10/14, 10/17, 10/18, and 10/21 of 1999. The black line represent TC1's track, and the black crosses represent the locations of TC1 centers every 6 hours from 00Z to 24Z of the day. TC1's strongest stage occurs on 10/17.

On 10/18, TC winds blow onto the northern boundary of the BoB, which directly pile up onshore and increase SSH (Figs 5.1 & 5.2, middle rows), and the shallower topography in this region may also contribute to the intensified SSH response. When TC1 travels inland on 10/18, the strong background north-northwestward winds in the northern BoB in RcWIND (Fig. 5.1g) continue to induce Ekman convergence toward the coast of northwestern Myanmar and accelerate the surface currents toward the coast of Bangladesh, both of which result in SSH rise (Fig. 5.2g). After TC1 leaves the BoB, the negative SSHAs in the northwestern BoB gradually recover (Figs 5.1g and 5.1j for 10/18 and 10/24, respectively). On 10/24, the SSHAs are weak except for near the landfall location, indicating that the effect of TC wind-induced SSH variations generally return to normal via oceanic adjustment (Figs 5.1k and 5.ll).

5.1.2 Northwestern BoB Cooling: Processes

Given that TC1 produces its largest cooling in the northwestern Bay, here we examine the processes that cause the strong cooling. In the BoB, Ekman layer depth ($H_E = \sqrt{2A/f}$, where A is viscosity and the maximum viscosity due to shear instability in HYCOM configuration is 50×10^{-4}m^2/s, and f is Coriolis parameter) is less than 19.87m at 10°N, 16.28m at 15°N, and 13.25m at 23°N. Zonal and meridional Ekman transports are defined as $\begin{cases} u_E = \dfrac{\tau^y}{\rho f} \\ v_E = -\dfrac{\tau^x}{\rho f} \end{cases}$, and Ekman pumping velocity is: $w_e = \dfrac{\partial}{\partial x}(\dfrac{\tau^y}{\rho f}) - \dfrac{\partial}{\partial y}(\dfrac{\tau^x}{\rho f})$.

The temperature tendency by vertical mixing is calculated as the time rate of change of

temperature accomplished by the KPP scheme in HYCOM, whereas the temperature tendency by OHT is calculated as the time rate of change of temperature accomplished by the continuity and advection scheme. Note that upwelling/downwelling may indirectly alter the strength of vertical mixing in the KPP scheme through changing vertical temperature gradient. The continuity equation in HYCOM calculates the mass change due to mass flux convergence/divergence, which alters the OHC essentially by upwelling process. The advection scheme in HYCOM calculates (1) Laplacian horizontal temperature diffusion, and (2) horizontal temperature advection by ocean currents; therefore, the temperature tendency calculated by the advection scheme in HYCOM actually represents the effect of both diffusion and advection. Nonetheless, the magnitude of diffusion is found typically ~1% of that of current-carried advection in the MR and EXPs (not shown). Therefore, the OHT in this study is defined as OHC change due to a combination of the effects of mass flux or upwelling, advection and diffusion.

Fig. 5.3 shows the Ekman transport and Ekman pumping velocity (left column) and the tendency of $T_{0\text{-}30m}$ by vertical mixing and by OHT (right column) in the northwestern BoB for 10/14, 10/17, 10/18, and 10/21. The analysis depth 0-30m is chosen because the mixed layer of the BoB is on average less than 30m without the impacts of TC1 and TC2 (Section 4.1), and the northwestern BoB (Region B in Figs 4.2 and 4.3) has the mixed layer shallower than 30m even after TC1 and TC2's disturbance. In addition, the estimated Ekman layer depth is only ~15m near the landfall locations of TC1 and TC2. Ekman transport and Ekman pumping velocity are weak before TC1 appears (Fig. 5.3a), even though a few small heating/cooling areas are shown (Fig. 5.3b). TC1 spans 10/15 00Z ~ 10/19 06Z.

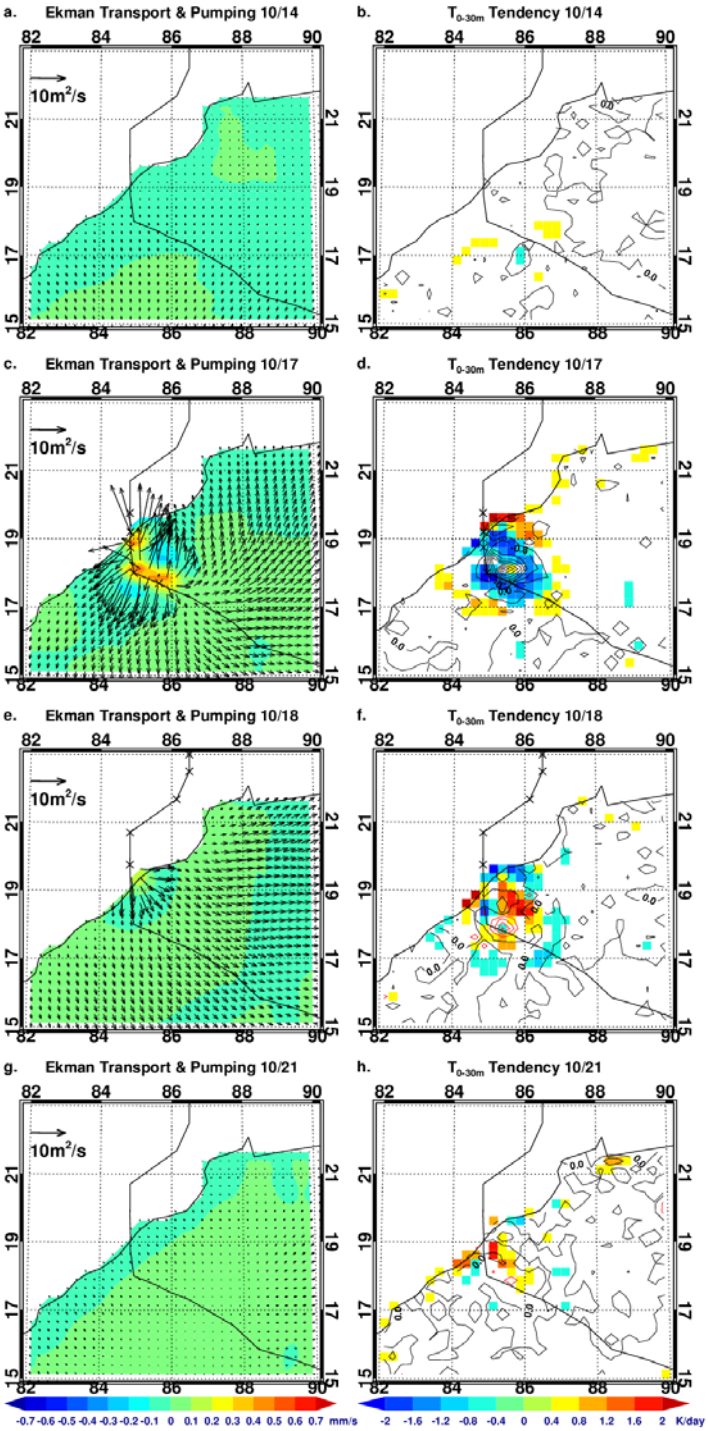

Fig. 5.3: (left) Ekman transport (vectors) and Ekman pumping velocity (color shades), and (right) top 30m-averaged temperature tendency by vertical mixing (black contours for neutral and cooling, and red contours for warming; interval: 0.4K/day) and by horizontal OHT (color patches; definition is given in the text) from RcWIND. Temperature tendency between -0.4K/day and 0.4K/day by horizontal OHT in the right column is suppressed. TC1's track is superimposed on the map (black line), and the crosses represent the locations of the TC centers every 6 hours from 00Z to 24Z of the day.

As TC1 travels near Orissa (Figs 5.3c and 5.3d for 10/17), the Ekman transport induced by TC1's cyclonic winds is directed outward from the TC centers, and the strength increases from the TC center to the radius of maximum sustainable wind (MSW) of TC1 and decreases beyond the radius of MSW. Within the radius of MSW of TC1, the surface Ekman divergence induces upwelling (yellow or red shades in Fig. 5.3c) and thus cools the upper ocean, as is shown by the OHT in Fig. 5.3d. Outside the radius of MSW of TC1, on the other hand, the decrease of Ekman transport *strength* in the radial direction causes surface Ekman convergence and thus downwelling (blue shades in Fig. 3c). This effect is more prominent on the right of the track because in that area the wind speed is stronger due to the addition of translation speed to the circular wind.

Both upwelling (color shades in the left column of Fig. 5.3) and oceanic vertical mixing (contours in the right column of Fig. 5.3) decrease $T_{0\text{-}30m}$ within the effective range of TC1, and horizontal advection spreads the cooling region (compare the positive Ekman pumping velocity in Fig. 5.3c with the negative OHT effect in Fig. 5.3d). On 10/17, there is a relatively strong upwelling zone (centered at 85.135°E, 18.125°N; Fig. 5.3b) on the right of the turning point of TC1's travel direction, while the strongest $T_{0\text{-}30m}$ cooling by vertical mixing during TC1 from RcWIND occurs 1/4 degree to the east of the upwelling center (centered at 85.375°E, 18.125°). The $T_{0\text{-}30m}$ cooling by upwelling and vertical mixing depends on the strength of wind stress and the time duration that wind stress acts on the ocean. The veering of travel direction and slow-down of travel speed on 10/17 (see black crosses in Fig. 5.3d for TC1 centers) prolong the effect of upwelling and turbulent mixing on the right of the track and thus reduces $T_{0\text{-}30m}$ considerably in that region. The divergent currents bring the cold water outward and result in

larger cooling area (-2.10K/day for 10/17 and -2.30K/day for 10/18; Figs 5.3d and 5.3f). After TC1 makes landfall, the cooling effect by vertical mixing significantly decreases. Meanwhile, the locations of $T_{0\text{-}30m}$ cooling or warming by OHT are basically reversed, with the low-$T_{0\text{-}30m}$ area shrinking and shifting to the northwest (Fig. 5.3f for 10/18).

Surprisingly, while the strong $T_{0\text{-}30m}$ cooling by vertical mixing mostly diminishes on 10/18 (Fig. 5.3f), a small $T_{0\text{-}30m}$ warming area by vertical mixing emerges with its center (85.375°E, 17.875°N) located 1/4 degree to the south of the cooling center for 10/17. The strongest warming effect by vertical mixing reaches ~1.72K/day at the warming center on 10/18 and then quickly shrinks on 10/19 (not shown). The heat source of the $T_{0\text{-}30m}$ warming by vertical mixing in this area mainly comes from horizontal warm advection in the deeper layer, given that on 10/18 upwelling/downwelling is weak there (Fig. 5.3e) and the warming by NetHF is less than 0.2K/day across the domain in Fig. 5.3 (not shown). The warming by OHT in the layer between 60m and 120m reaches ~1.97K/day beside the mixing warming center. The horizontal warm advection between 60m and 120m increases thermal instability; together with shear instability induced by inertial oscillation (see Section 5.1.3 below), it warms up the temperature above 60m. Note that the $T_{0\text{-}30m}$ warming by vertical mixing on 10/18 has short duration and limited to a small area, which does not conflict with the findings of upper ocean warming by NetHF over the BoB after the TCs in Chapter 4.

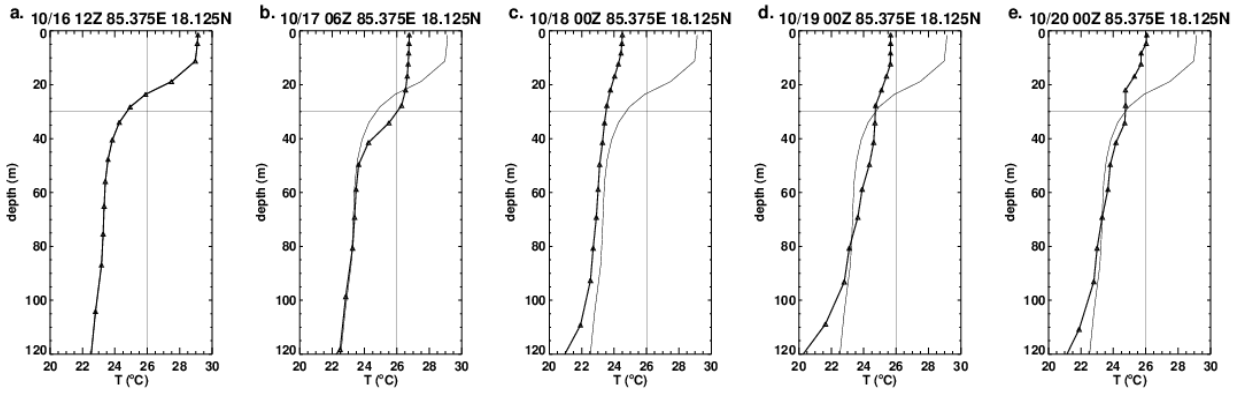

Fig. 5.4: Vertical potential temperature profile at 85.375°E, 18.125°N from RcWIND for a) 10/16 12Z, b) 10/17 06Z, c) 10/18 00Z, d) 10/19 00Z and e) 10/20 00Z of 1999. The thick lines with triangle symbols are the potential temperature at the time, while thin black lines without symbols are the potential temperature in panel a (the earliest profile that is being shown). The triangle symbols are located at the center of each model layer, whose thickness may vary with time. The 30m depth and 26°C isotherm are also shown as thin black lines for reference purpose.

The effect of vertical mixing can also be seen in the time evolution of potential temperature profile (Fig. 5.4) from RcWIND at 85.375°E, 18.125°N – the location of strongest $T_{0\text{-}30m}$ cooling by vertical mixing during TC1. Before TC1 arrives, the cooling center has a 12m-deep ML (Fig. 5.4a). After TC1 arrives, the top layer loses some heat through surface heat flux; as TC1 induces strong turbulent mixing, the OHC above 50m quickly redistributes (Fig. 5.4b), which indicates the DOHP effect by TC1's winds in this region (Chapter 4). The maximum cooling rate of $T_{0\text{-}30m}$ by vertical mixing during TC1 is ~-3.81K/day on 10/17 offshore Orissa (Fig. 5.3d). Because the mixing cooling center is located in the upwelling zone, $T_{0\text{-}30m}$ there is also cooled by upwelling (compare Fig. 5.4c with 5.4b for temperature profile shift between 10/17 06Z and 10/18 00Z). Meanwhile, heat loss in the top 30m due to negative NetHF on 10/17 (~-143.18W/m^2; equivalent to lowering $T_{0\text{-}30m}$ by 0.10K) slightly lowers $T_{0\text{-}30m}$. After TC1's dissipation, vertical mixing in the thermocline persists and penetrates to ~100m by 10/20 00Z (Fig. 5.4d). The warm OHT in the deeper layer on 10/18 (~1.94K/day for the layer between 60m and 120m) together with the vertical mixing that is associated with inertial oscillation (see Section 5.1.3) increases the

temperature above (compare Fig. 5.4d with Fig. 5.4c for temperature increase between surface and 100m), while near surface regains heat through NetHF (~163.20W/m^2; equivalent to increasing $T_{0\text{-}30m}$ by 0.11K). On the other hand, there is cold OHT between 60m and 120m on 10/19 (~-1.57K/day), which decreases temperature between 30m and 90m and has little impact on $T_{0\text{-}30m}$ (compare Fig. 5.4e with 5.4d). The NetHF at this location on 10/19 is ~160.48W/m^2 10/19, equivalent to increasing $T_{0\text{-}30m}$ by ~0.23K.

5.1.3 Effects Inertial Oscillation on Upper Ocean Temperature

As discussed above, the $T_{0\text{-}30m}$ cooling/warming effect by OHT is primarily caused by Ekman transport divergence and horizontal advection by near surface currents. The surface currents consist of Ekman drift, geostropic current, and currents associated with TC-induced inertial oscillations. TC-induced near-inertial oscillations have been extensively investigated and discussed in the previous studies [e.g., Chang and Anthes, 1978; Price, 1981; Shay *et al.*, 1990; Shay *et al.*, 1992; Price *et al.*, 1994; Firing *et al.*, 1997; Dickey *et al.*, 1998; Jacob *et al.*, 2000; Zedler *et al.*, 2002; Sanford *et al.*, 2007; Shay *et al.*, 2008; Tsai *et al.*, 2008; Gierach *et al.*, 2009; Jaimes *et al.*, 2010; Sanford *et al.*, 2011]. Fig. 5.5 shows an example of TC1-induced near-inertial oscillation on the right of TC1's turning point (travel direction changing from west-northwestward to nearly northward). Surface currents to the right of TC1 rotate clockwisely from southeastward in Fig. 5.5a to northwestward in Fig. 5.5d. Note that the near-inertial currents near the coast in Fig. 5.5d are strongly deflected by the coastal geostrophic flow. The period of the near-inertial oscillation is found to be very close to the inertial period at 18.5°N (~1.57 days). The inertial currents overlap a large region of the cold $T_{0\text{-}30m}$, and span the area of vertical mixing-induced cooling (Fig. 5.3d), suggesting that the inertial oscillation induced by

TC winds may enhance mixing and thus the surface cooling by causing shear instabilities [e.g., Price, 1981]. Meanwhile, the strong currents associated with the inertial oscillation can also help to "shape the cooling area" via advection. For example, when the currents are mostly southeastward on the right of the turning point of TC1 (Figs 5.5a and 5.5b for 10/18 03Z and 09Z, respectively), the cold water is brought out of the low-$T_{0\text{-}30m}$ center and warm OHT from north reduces the magnitude and area of low-$T_{0\text{-}30m}$ anomaly. The low-$T_{0\text{-}30m}$ center then is shifted by the west-northwest flow (Fig. 5c for 10/18 15Z). The $T_{0\text{-}30m}$ gradients on the right of the turning point are further reduced when the currents turn to northwestward (Fig. 5d for 10/18 21Z). The currents associated with the near-inertial oscillation also weaken the SSH gradients (not shown).

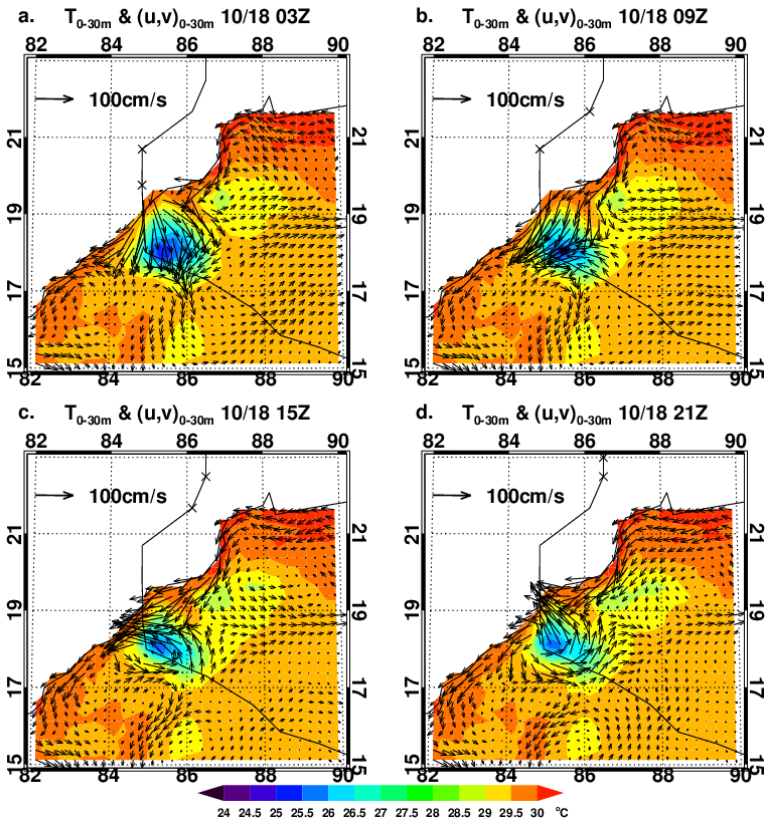

Fig. 5.5: An example of $T_{0\text{-}30m}$ (color shades) and currents in the top 30m (vectors) near the landfall location of TC1 from RcWIND experiment. The fields shown here are 6-hourly average centered at 03Z, 09Z, 15Z and 21Z on 10/18 of 1999.

Due to its influence on near surface temperature, the near-inertial oscillation can also be identified in temperature perturbations of the upper ocean. Fig. 5.6 shows an example of times series of the upper ocean temperature at 85.375°E, 18.125°N – the same location as for the vertical temperature profiles in Fig. 5.4. The initial temperature reduction at 15m starts at 10/16 18Z, when the temperature at 30m increases due to the homogenization of upper ocean temperature by vertical mixing. The temperature at 50m responds to vertical mixing with mild increase soon after the temperature reduction at 15m. The temperature above 100m starts to oscillate after the initial drop and has period of ~1.5 days, similar to the period of the near-inertial currents (~1.60 days at 18.125°N).

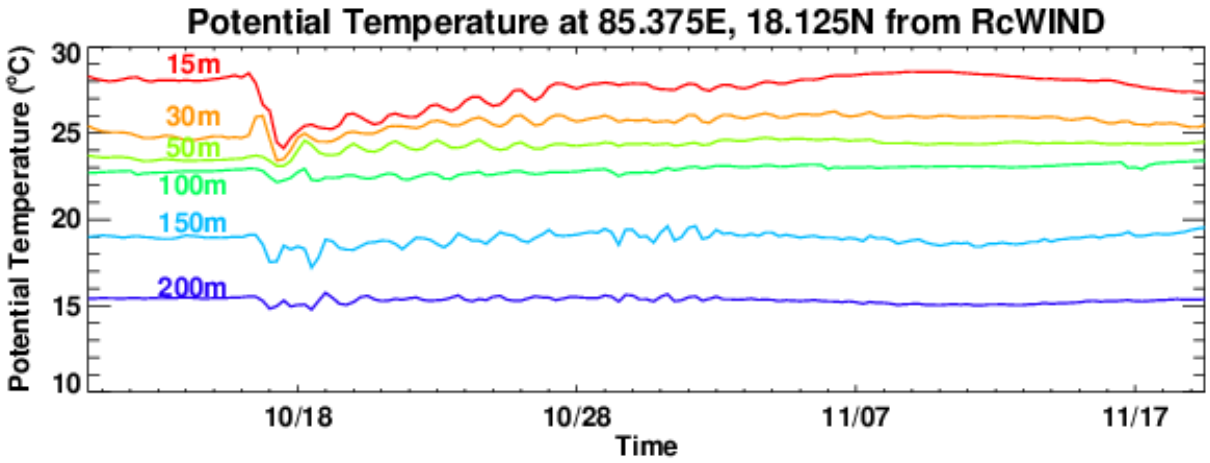

Fig. 5.6: Time Series of potential temperature from RcWIND at 85.375E, 18.125N for 15m, 30m, 50m, 100m, 150m, and 200m.

5.2 Impacts of TC2

5.2.1 Upper ocean dynamical response

Approximately 6 days after the dissipation of TC1, TC2 appears on 10/25, 1999. When it travels across the northern BoB, a weak low-SSH area along the track between 90°E and 94°E is

induced on 10/27 by surface Ekman divergence (Fig. 5.7b) that is caused by TC2's cyclonic winds (Fig. 5.7a; MSW: 60kt or ~31m/s at 10/27 00Z, and 100kt or ~51m/s at 10/28 00Z; strengthening from tropical storm to Category-3 TC). Due to the strong winds and slow translation speed from 10/27 12Z–10/27 18Z (3.68kt or ~1.89m/s according to IBTrACS), the negative SSHAs near the TC centers during that period (91°E, 17°N) are most significant in the temporal average of the following day (Fig. 5.8c). On 10/28, the oval-shaped low-SSH area is deepened and elongated when TC2 travels further northwestward and moves slowly along the track (Figs 5.8a-5.8c). However, the SST in the low-SSH area has mild temperature decrease of less than 0.3°C due to the weaker winds and deeper ML in that region (not shown).

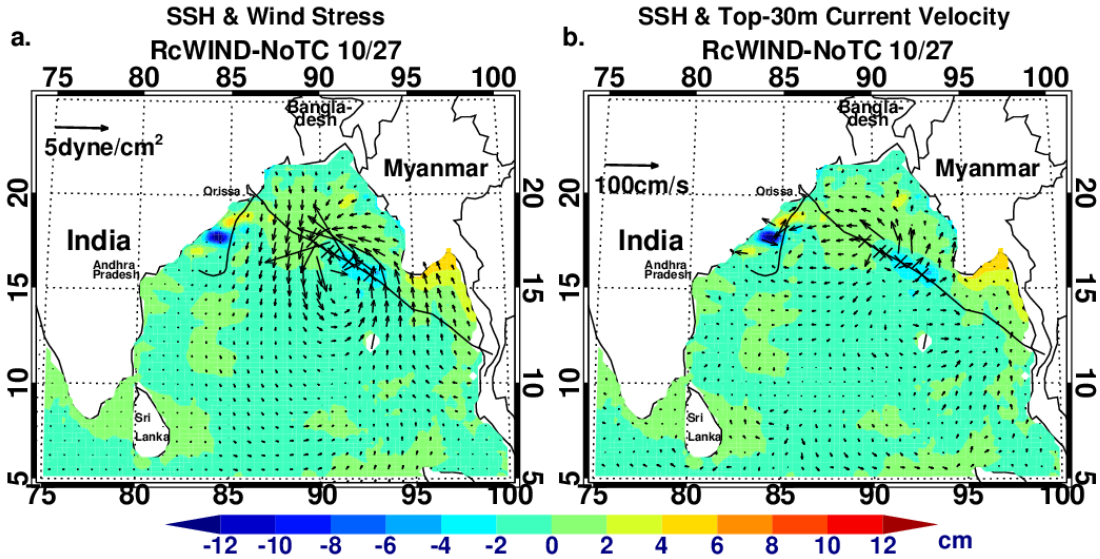

Fig. 5.7: (left) Differences of daily-averaged SSH (color shades) and 10m wind stress (vectors) between RcWIND and NoTC, and (right) differences of daily-averaged SSH (color shades) and current velocity in the top 30m (vectors) between RcWIND and NoTC for 10/27of 1999. The black line represent TC1's track, and the black crosses represent the locations of TC1 centers every 6 hours from 00Z to 24Z of the day.

Compared to that during TC1, the background wind of southwesterly during TC2 (Fig. 5.8a) induces stronger Ekman transport toward the coastline of the northern and eastern BoB and has

stronger effect on SSH fields along the perimeter of the Bay on 10/28 (Fig. 5.9a). The southerly wind in the Andaman Sea (Fig. 5.8a) piles up water to the coasts of southeastern Myanmar and raises SSH (Fig. 5.9a). The cyclonic winds of TC2, as a category-4 cyclone on 10/28, also force positive SSHAs in the northern tip of the BoB (Figs 5.8a-5.8c). Two other low-SSH areas are induced by surface Ekman divergence along the track between 10/28 18Z and 10/29 06Z with slightly rightward bias (Figs 5.9d-5.9f). The two low-SSH areas are also accompanied by two low-$T_{0\text{-}30m}$ areas that are induced by upwelling and vertical mixing. The low-SSH areas are associated with the slow translation speed (~4.65kt or ~2.39m/s according to IBTrACS) from 10/28 18Z – 10/29 00Z and the strong winds (137.5kt or ~70.7m/s at 10/28 18Z, and 140kt or ~72m/s at 10/29 00Z, respectively; Category 5). The low-$T_{0\text{-}30m}$ areas are somewhat shifted to the north of the low-SSH areas and will be discussed in more details below (Section 5.2.3).

The cross-shore SSH gradients along the coastline of northern BoB are intensified on 10/29 and 10/30 by the atmospheric background circulation and TC wind stress (Figs 5.8d and 5.8g). Associated with the SSH gradients, geostrophic currents flow counter-clockwisely along the coastline (Figs 5.9d and 5.9g). Note that the spatial range for wind reconstruction is only limited to two times of the radius of 35-kt (~18m/s) wind, which is always less than 4.5° in central angle for our TC cases, and therefore the large SSH variability in RcWIND is only evident near the track, compared to the NoWSTR or NoTC results (Figs 5.8e and 5.8f for 10/29, and Figs 5.8h and 5.8i 10/30). The negative SSHA areas along the track induce cyclonic geostrophic currents around them (Figs 5.9e and 5.9f for 10/29, and Figs 5.9h and 5.9i for 10/29). After TC2 makes landfall and is stalled inland, the SSH gradients along the coastline reduce (Fig. 5.8j for 11/3). Meanwhile, the negative SSHA areas along the track and their associated geostrophic current anomalies weaken (Figs 8k and 8l for 11/3).

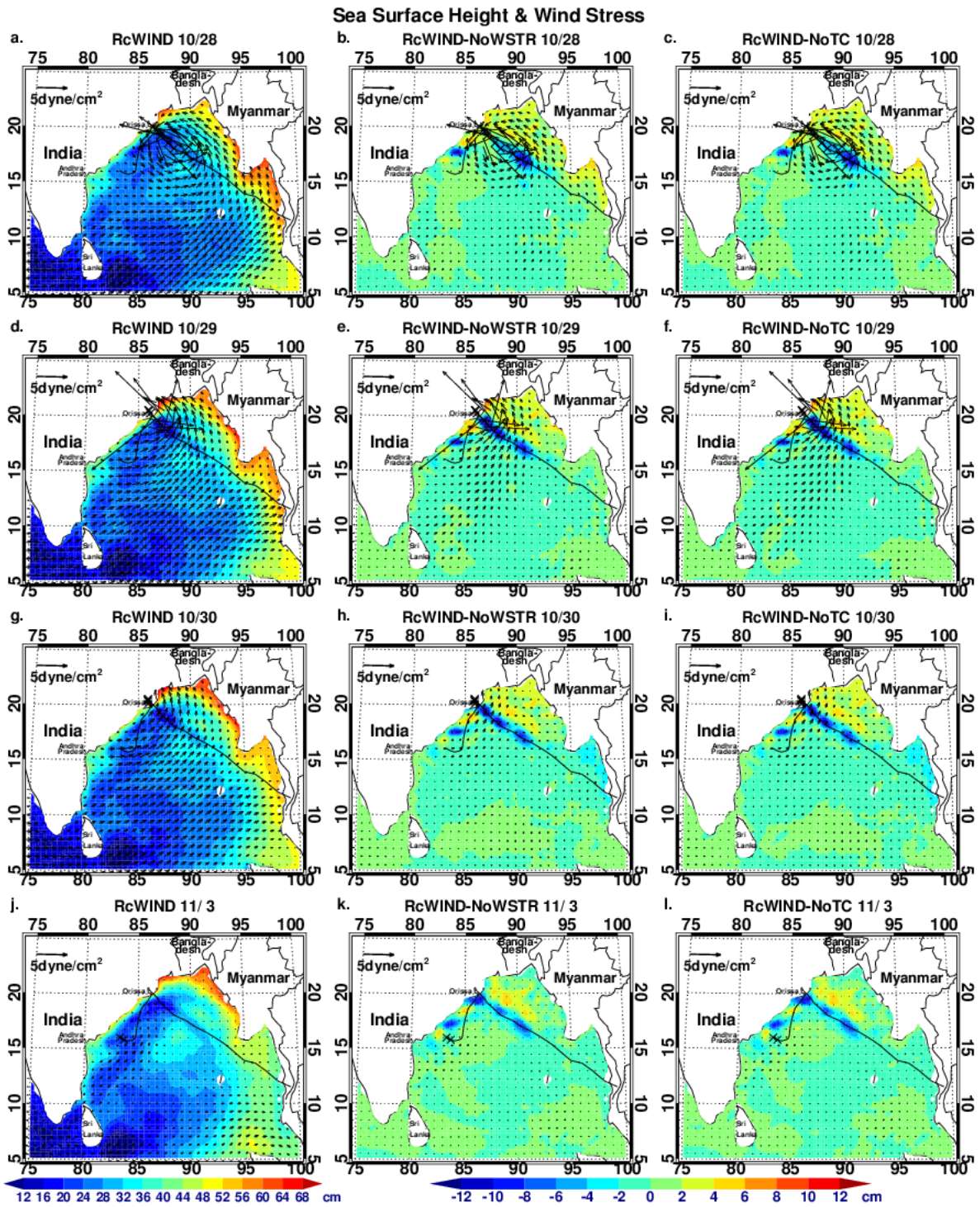

Fig. 5.8: Similar to Fig. 5.1, but for TC2 and 10/28, 10/29, 10/30, and 11/3.

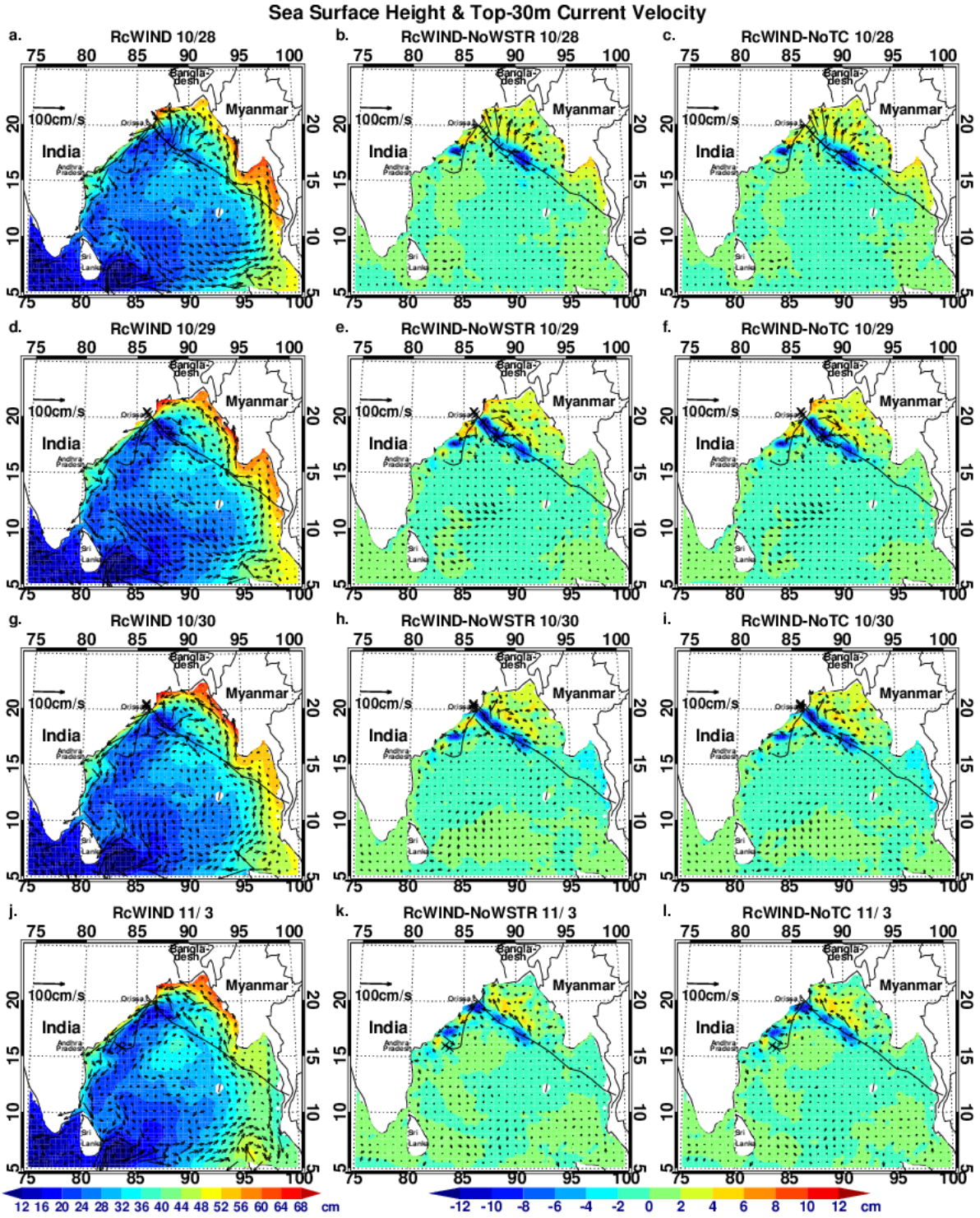

Fig. 5.9: Similar to Fig. 5.2, but for TC2 and 10/28, 10/29, 10/30, and 11/3.

5.2.2 Northwestern BoB Cooling: Processes

TC2 lingers across the BoB from Malaysia peninsula to Orissa, India from 10/25 to 10/29 in northwestward direction. The Ekman transports induced by the cyclonic winds of TC2 diverge from the TC2 track, and thus cause upwelling along the track in the RcWIND simulation (yellow and red shades of Fig. 5.10a). Simiar to TC1, the regions of Ekman divergence and upwelling are rightward-biased due to the stronger wind speed on the right of the track, which correspond well to the cooling areas due to OHT (Fig. 5.10b). In addition, downwelling areas exist near the upwelling zones due to the decrease of Ekman transport *strength* with the distance from the TC centers (blue shades in Fig. 5.10a). The strongest cooling effect by vertical mixing is ~-1.96K/day on 10/28 (Fig. 5.10b) and located (87.375°E, 19.625°N) to the northwest of the strongest upwelling center. The cooling by vertical mixing (centered at 87.875°E, 18.625°N) near the TC2 center at 10/28 12Z has relatively weak effect (maximum value ~-1.82K/day), compared to the mixing cooling during TC1, likely due to the decrease of vertical temperature gradient by TC1-induced vertical mixing earlier. The strongest cooling effect by OHT is ~-2.68K/day on 10/28 beside the TC center at 06Z. Advection by surface currents expands the cooling region, as can be seen by the larger negative OHT areas than the upwelling zones (compare the yellow and red areas of Fig. 5.10a with the blue regions of 5.10b).

As TC2 makes landfall on 10/29, the TC2-induced upwelling reaches the maximum intensity (~1.09mm/s) during the two TCs, with two weak downwelling areas on the north and south sides of the upwelling (Fig. 5.10c). The cooling effect by vertical mixing near TC2's track is weaker than the day before (Fig. 5.10d) The warm OHT in most of the region of 87.5°E-89.5°E 17.75°N-19.75°N on 10/29 compensates the cooling of the day before. From 10/30 onwards, the wind stress quickly weakens and the associated upwelling cooling basically disappears (Figs 9e-9h).Meanwhile, the $T_{0\text{-}30m}$ cooling effect by vertical mixing becomes very unobvious, while

the warm/cold OHT pattern becomes chaotic (Figs 5.10g and 5.10h).

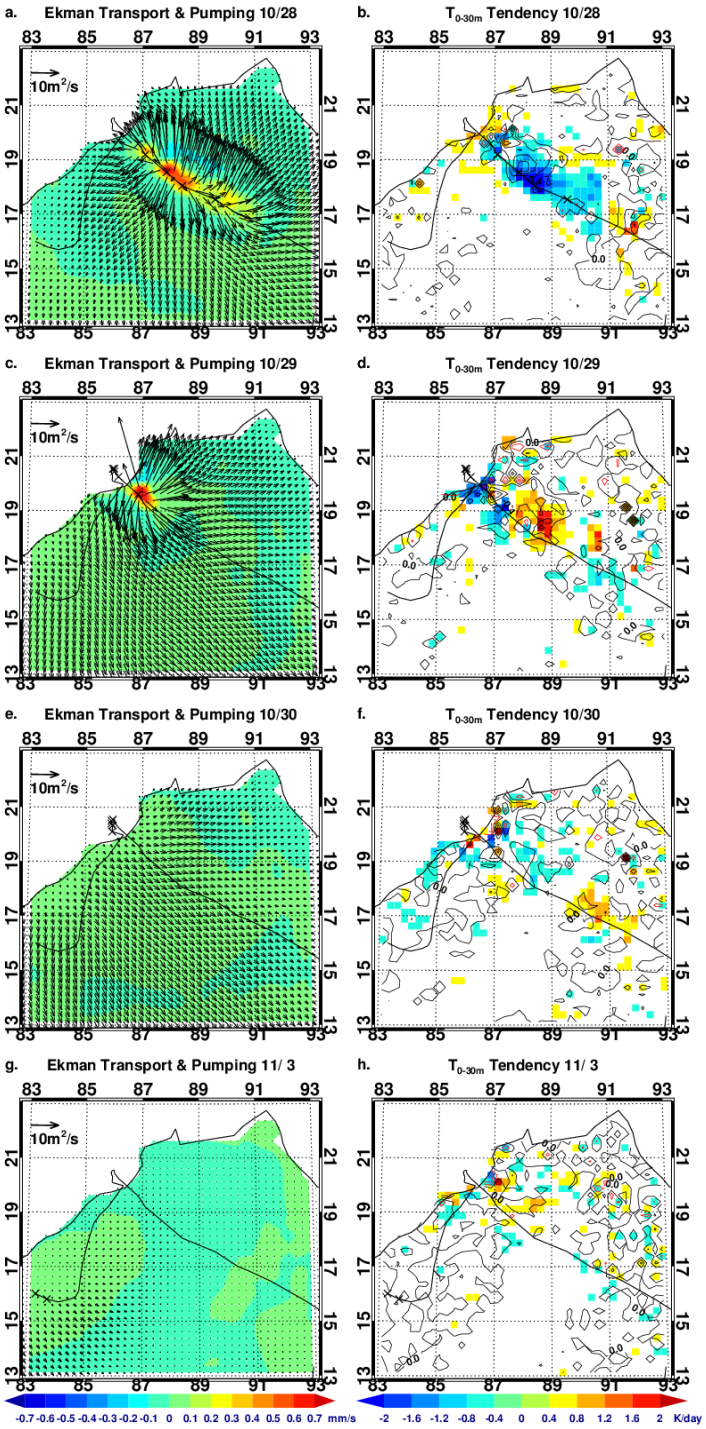

Fig. 5.10: Similar to Fig. 5.3, but for TC2 and for 10/28, 10/29, 10/30, and 11/3. The presenting domain is also enlarged and shifted.

Fig. 5.11 shows an example of vertical potential temperature profile from RcWIND at 87.875°E, 18.625°N, the location of lowest $T_{0\text{-}30m}$ in Fig. 5.12b. Unlike the temperature profile in Fig. 5.4, this example is located in an area with less cooling by vertical mixing and intended to demonstrate the importance of upwelling. Compared to the strong mixing cooling center that is induced by TC1 (Fig. 5.4), this low-$T_{0\text{-}30m}$ center has a deeper pre-existing ML (~25m; Fig. 5.11a). The initial response to TC2's cyclonic wind is mild mixing in the ML that lowers the SST by more than 0.5°C, and strong upwelling that lifts the ML to ~5m (Fig. 5.11b). Within 6 hours, significant temperature decrease over the top 40m occurs (SST decrease by ~3.1°C) primarily due to cyclonic winds-induced Ekman divergence and upwelling, instead of vertical mixing (Fig. 5.11c). The pre-existing near-surface warm water has been transported out of the $T_{0\text{-}30m}$ cooling area, and the cold water from below replaces the original warm seawater. This phenomenon can be identified by uniform cooling of the top 300m near the low-$T_{0\text{-}30m}$ center, without a significant sign of vertical OHC redistribution through mixing (not shown). This result demonstrates that the hypothesis of the ML cooling and thermocline warming caused by TC-induced turbulent mixing in Emanuel [2001] *cannot* be identified in the strong cooling area for this TC2 case, although near-inertial oscillation afterwards will be shown to still have mild DOHP effect (Section 5.2.3 below). Vertical mixing only plays a minor role in SST reduction in both the low-$T_{0\text{-}30m}$ regions of Figs 5.12c-5.12h. The low-$T_{0\text{-}30m}$ center closer to the coast (87.125°E, 19.375°N of Fig. 5.12c) has very similar temporal evolution pattern for vertical potential temperature profile as that shown in Fig. 5.11 (88.125°E, 18.625°N) due to their proximity (not shown).

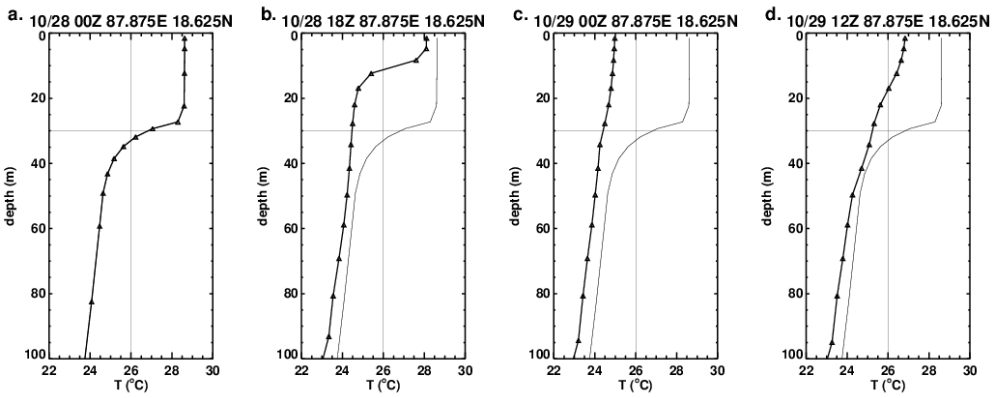

Fig. 5.11: Similar to Fig. 5.4, but at 87.875°E, 18.625°N and for 10/28 00Z, 10/28 18Z, 10/29 00Z, 10/29 12Z.

5.2.3 Effects of Inertial Oscillation on Upper Ocean Temperature

The currents and $T_{0\text{-}30m}$ in the northwestern BoB have richer structures than TC1 case when TC2 travels through the BoB and approaches the land (Fig. 5.12). As of 10/28 12Z, TC2 is classified as a category-4 TC (MSW=135kt or ~69m/s); however, the strong wind does not produce a strong low-$T_{0\text{-}30m}$ area near the TC center (87.85°E, 18.55°N) until 6 hours later when TC2's moving speed starts to slow down (Fig. 5.12b). The slow translation speed (~4.65kt or ~2.39m/s) from 10/28 18Z-10/29 00Z (black crosses for the TC centers in Fig. 5.12b) even produces a second low-$T_{0\text{-}30m}$ area near the TC center (87.1°E 19.2°N) of 10/28 18Z. The minimum SSH and $T_{0\text{-}30m}$ values occur slightly to the right of the track, which is closer to the track than TC1 with higher translation speed (Figs 5.8b-5.8c and Figs 5.12c-5.12h). This rightward-biased feature is consistent with previous studies [e.g., Price, 1981].

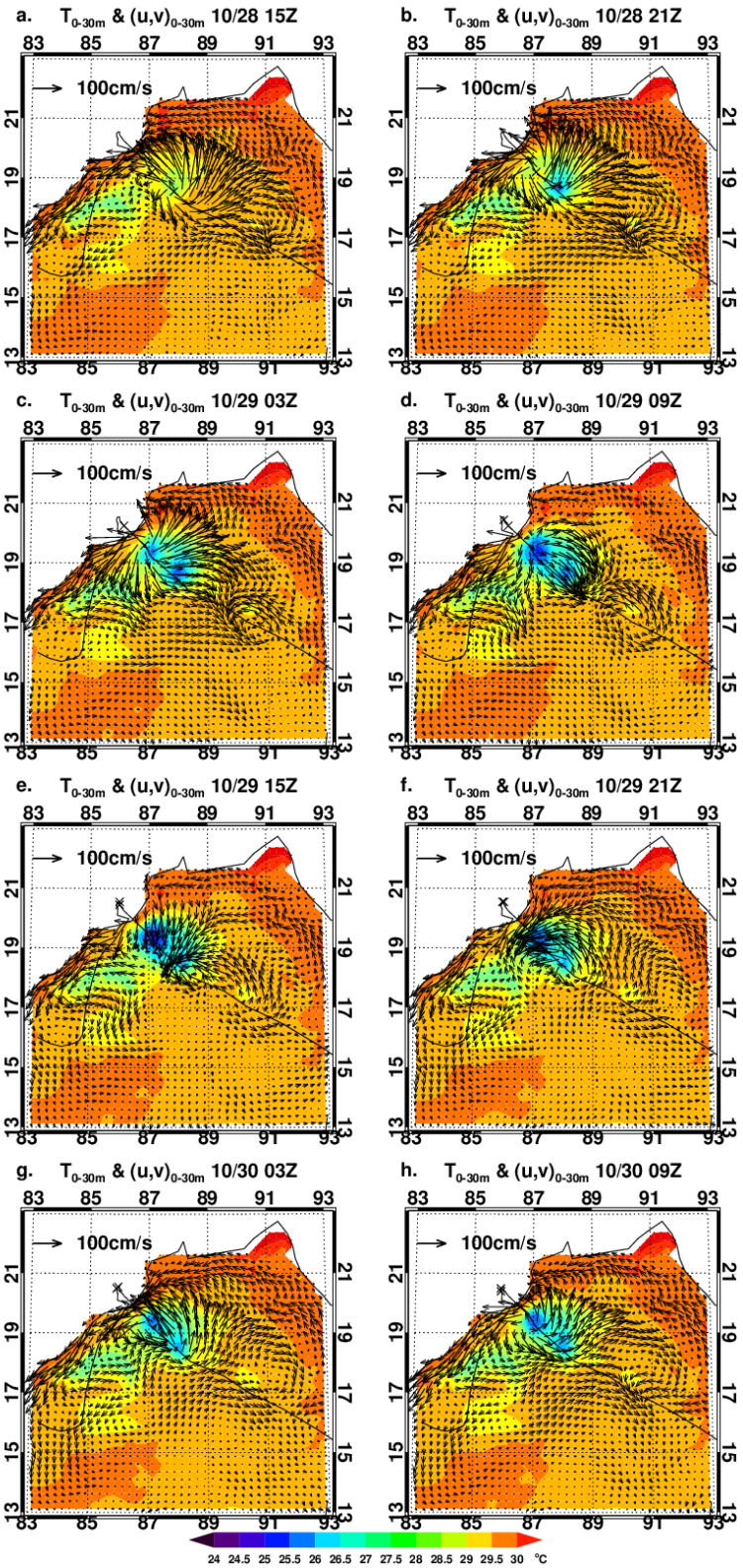

Fig. 5.12: Similar to Fig. 5.5, but for TC2 and 6-hour time-averaged centered at 03Z, 09Z, 15Z and 21Z for the period from 10/28 12Z to 10/30 12Z.

After TC2 makes landfall, the TC cyclonic winds weaken substantially, and the currents in the northwestern BoB become very complex, including the currents result from inertial oscillations and the geostrophic flow along the coasts and around the SSH anomalies near the TC track. The near-inertial oscillation on the right of the track dominates most of the area of the two connected low-SSH low-$T_{0\text{-}30m}$ regions since 10/29 06Z (Figs 5.12d-5.12h). The near-inertial oscillation of currents can be identified by the rotating of the current direction from southeastward at 10/29 09Z (Fig. 5.12d) to northeastward at 10/30 09Z (Fig. 5.12h), which advect $T_{0\text{-}30m}$ anomaly around on the right of the track.

Fig. 5.13 shows an example of time series of the upper ocean temperature at 87.875°E, 18.625°N – the same location as for the vertical temperature profiles in Fig. 5.11. This location is in a weak mixing cooling zone but characterized by its lowest $T_{0\text{-}30m}$. Different from Fig. 5.6 during TC1, the initial temperature drop at 15m starting at 10/18 12Z is not accompanied by a temperature rise at 30m or deeper, because the temperature decrease at 30m or deeper reflects the cooling by upwelling. The temperature from 15m to 250m responds to upwelling nearly simultaneously around 10/28 12Z, although the perturbation is less effective in the deeper ocean. The temperature above 100m appears to oscillate after the initial drop; however, the oscillation does not have a clear period except at 30m and 50m until 11/6. The period of oscillation at 30m and 50m from 11/6-11/17 is ~1.5 days, similar to the period of the near-inertial currents. The cooling induced by the near-inertial oscillation also appears to delay the upper ocean temperature recovery every ~1.5 days. The near-inertial oscillation induced by TC2 on the right of its track when TC2 has slow translation speed (~4.65kt or ~2.39m/s from 10/28 18Z-10/29 00Z) thus is found to have strong influence on the OHT in the top 30m, and weak influence on the temporal evolution of temperature in the top 50m via shear instability-associated vertical mixing.

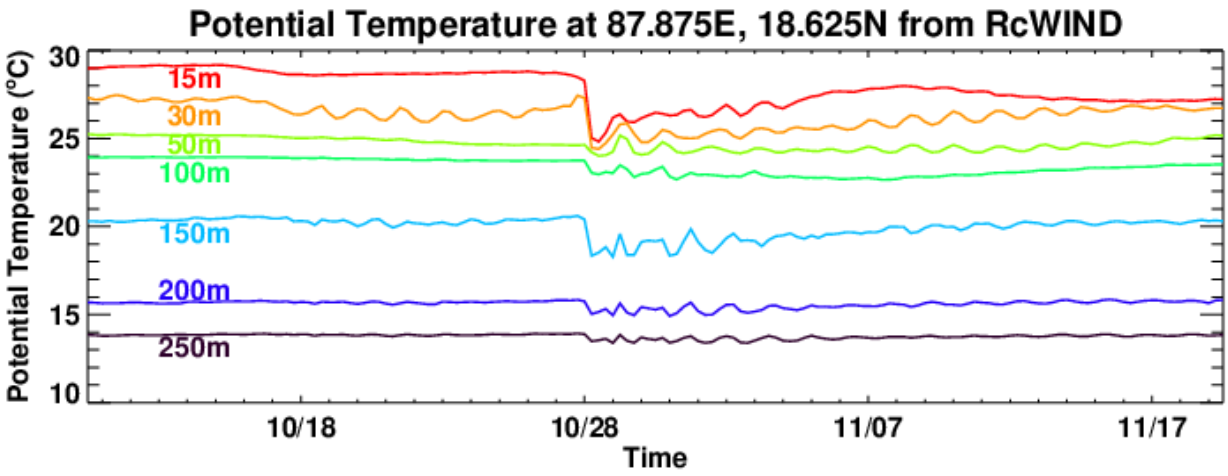

Fig. 5.13: Similar to Fig. 5.5, but at 85.625E, 18.375N for 15m, 30m, 50m, 100m, 150m, 200m, and 250m.

5.3 Coastal Kelvin Waves and Rossby Waves

The background winds during the two TC events substantially strengthen and raise sea level along the coastline in the northern BoB (Fig. 5.1 and 5.8). The positive SSHAs excite coastal Kelvin waves, which travel along the east India coastline and split to coastal Kelvin waves and Rossby waves after they go around Sri Lanka (Fig. 5.14a and 5.14b for 11/17). As the coastal Kelvin waves propagate counterclockwise along the west India coastline, the Rossby waves propagate westward along the latitude band of 2°N-10°N (Fig. 5.14c and 5.14d for 1/5). The positive SSHAs that are associated with the coastal Kelvin waves gradually dissipate when they circle around the Arabian Sea, and meanwhile the Rossby waves continue traveling westward and eventually arrive at Africa coast at the end of February, 2000 (Fig. 5.14e and 5.14f for 2/23). The coastal Kelvin waves-associated SSHAs induce alongshore geostrophic flows, while the Rossby waves carry the alternative meridional velocity signals (right column of Fig. 5.14) across the Indian Ocean.

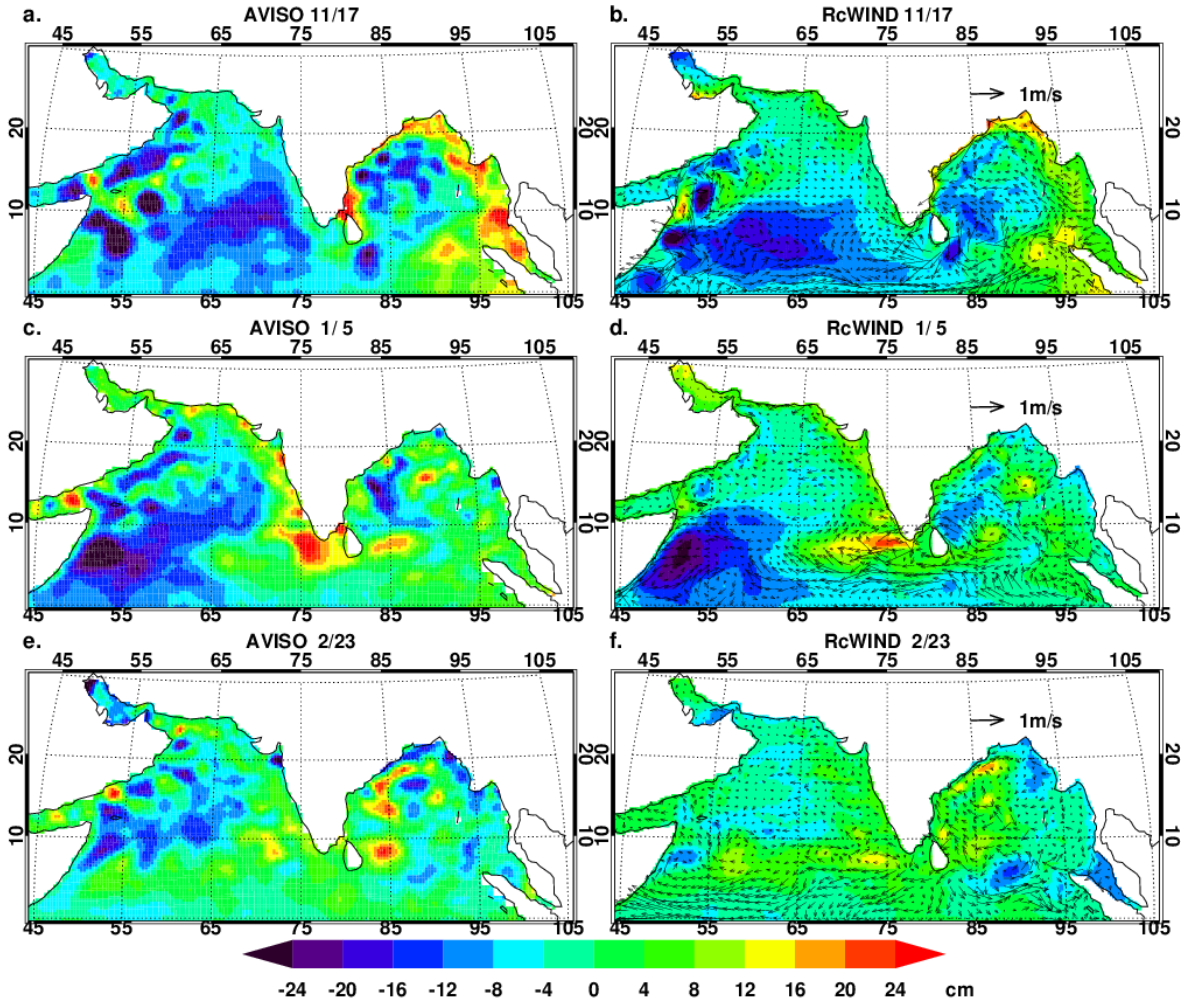

Fig. 5.14: Satellite-observed (left; AVISO) and model-simulated (right; RcWIND) SSHAs (color shades) at 00Z 11/17 of 1999, and at 00Z 1/5 and 2/23 of 2000. The ML current velocities from RcWIND are shown as arrows on the right column.

When the coastal Kelvin waves and Rossby waves travel around and across the Indian Ocean, respectively, the signals originated from the background winds during the TCs are carried out of the BoB. Because the associated positive SSHAs indicate more available ML heat content, they imply the potential change of regional climate on the seasonal scale. The alternative meridional currents that are associated with the Rossby waves may also induce meridional heat exchange between 2°N and 10°N. These findings are unique to the Indian Ocean due to its enclosed coastline and justifies the importance of regional TC events to the entire Indian Ocean

[Gerald Meehl, personal communication]. If an OGCM cannot resolve TCs' impacts in the BoB, the influence of model incapability is not confined to the Bay but would reach the western Indian Ocean in three to four months. The positive SSHAs that are associated with coastal Kelvin waves in the Arabian Sea are also speculated to be an additional heat source for intensifying another TC that is approaching the coast in the following season after a preceding TC in the BoB [Gerald Meehl, personal communication]. The related works may shape a future research direction.

5.4 Summary and Discussion

Results from the RcWIND, NoWSTR and NoTC experiments suggest that the SSH variations during TC1 and TC2 are primarily determined by wind stress. The atmospheric background flow of southeasterly at the ocean surface in the northern BoB produces large SSHAs during TC1 and TC2 via piling up water to the coasts as well as via Ekman transport, which may be intensified in the shallow topography. This can be seen from the SSH rise in the northern and eastern BoB during TC1 and TC2, which is especially prominent due to the southeasterly-induced Ekman transport and the northward currents accelerated by the winds. Along the coastline of the northwestern BoB, cross-shore SSH gradients are also built and induce counter-clockwise alongshore geostrophic currents when the two TCs approach the land. On the other hand, the southern BoB (near 10°N) is not in the effective range of TC1 and TC2, so the SSH fields in that region have little difference between RcWIND, NoWSTR and NoTC.

The magnitudes of SSH falling and $T_{0\text{-}30m}$ cooling by TC1 and TC2 depend on both wind stress strength and the time duration that wind stress acts on the ocean. The low-SSH and low-$T_{0\text{-}30m}$ area during TC1 forms on the right of the turning point within 12 hours after TC1 changes its moving direction from west-northwestward to northward, because TC1 has stronger

winds on the right and exerts longer effect. The wind-induced turbulent mixing and upwelling are the primary causes for cooling $T_{0\text{-}30m}$ on the right of the turning point. The near-inertial oscillation on the right of the turning point is simulated in RcWIND, and the associated rotating currents, together with the $T_{0\text{-}30m}$ distribution, have strong influence on the horizontal temperature advection. The near-inertial oscillation is also identified by the temporal variation of the upper ocean temperature, which has period close to the inertial oscillation (~1.57 days at 18.5 $^{\circ}$N).

TC2 produces three low-SSH regions along its track. The first low-SSH area is not accompanied by obvious low $T_{0\text{-}30m}$ because of the deeper ML in its location and the weaker cyclonic winds at that moment. When TC2 travels to the northwestern BoB, the strong winds (>72m/s) and slow travel speed (~4.65kt or ~2.39m/s) from 10/28 18Z – 10/29 00Z produce two other low-SSH regions that are accompanied by low $T_{0\text{-}30m}$ within 12 hours. The rightward bias of the low SSH and low $T_{0\text{-}30m}$ is again simulated, which is due to the stronger wind speed on the right of the track. The rightward bias is closer to the track than the case during TC1, possibly due to the slower translation of TC2. The impact of upwelling on the vertical potential temperature profile in the region of weak vertical mixing effect has been shown to demonstrate that the SST cooling may not represent DOHP effect of vertical mixing as hypothesized in some previous studies [e.g., Emanuel, 2001] for this case. The near-inertial oscillation induced by TC2 is obvious on the right of the track, and it affects mixing and horizontal temperature advection above 30m. The oscillation of current velocity and upper ocean temperature on the right of the track has a period close to the inertial oscillation (~1.52 days at 19°N).

Similar to previous research works [e.g., Chang and Anthes, 1978; Price, 1981; Shay *et al.*, 1992; Price *et al.*, 1994; Jacob *et al.*, 2000; Black *et al.*, 2007; Sanford *et al.*, 2007; D'Asaro *et*

al., 2007; Wada *et al.*, 2009; Sanford *et al.*, 2011], the HYCOM simulations in this study show clear rightward-biased oceanic responses to TC1 and TC2, which include stronger upper ocean cooling by mixing and upwelling, current velocities, and SSHAs. The near-inertial oscillations induced by TC1 and TC2 are also simulated on the right of the tracks as for the hurricanes in the Atlantic Ocean [e.g., Price, 1981; Shay and Uhlhorn, 2008] and for the typhoons in the Pacific Ocean [e.g., Jiang *et al.*, 2009; Tseng *et al.*, 2010]. Upwelling and vertical mixing are the main reasons for upper ocean cooling during TC1 and TC2, consistent with the studies of Price [1981], Jacob *et al.* [2000], Prasad and Hogan [2007], Gierach *et al.* [2009], Zedler *et al.* [2009]. As pointed out by Price [1981], D'Asaro et al. [2007], Huang et al. [2009], etc., horizontal advection may strongly affect the upper ocean heat balance during the several-day period following a TC passage; this study also shows that the surface currents associated with the near-inertial oscillations on the right of the tracks largely determine the temperature advection.

A small short-lived $T_{0\text{-}30m}$ warming area that is induced by vertical mixing after TC1 is discovered, whose heat source mainly comes from horizontal warm advection between 60m and 120m. Upwelling is an important mechanism for cooling the surface as expected; however, different from the hypothesis in Emanuel [2001] that surface heat is transferred downward during TCs (Fig. 1.2), the cooling by upwelling does not produce DOHP because the heat from the ML does not mix down to the thermocline layer. The author thus suggests further assessment in quantifying air-sea heat exchange induced by TCs using satellite-observed SSTs.

Chapter 6

Summary and Future Work

6.1 Summary

6.1.1 Background and Research Question – Downward Ocean Heat Pumping and Climate

Large-scale meridional heat transport is a crucial property of the climate system. In order to investigate its variations and its effect on climate change, scientists must quantify the oceanic component of meridional heat flux. While oceanic thermal diffusion in the lower latitudes under modest weather conditions is deemed insufficient to account for the source of poleward heat flux, TCs are hypothesized to induce DOHP and transfer significant amount of heat from the atmosphere into the ocean. Although many efforts have been devoted to quantify TCs' contribution to meridional heat transport [e.g., Emanuel, 2001; Sriver and Hubert, 2007; Sriver *et al.*, 2008; Manucharyan *et al.,* 2011; Hu and Meehl, 2009], large discrepancies still exist for the estimates of TC effect; therefore, the hypothesis needs further examinations.

This study focused on addressing one research question: how do TCs, such as TC1 and TC2, impact on the BoB heat budget? When previous research works emphasized on the Atlantic and Pacific basins, very few modeling works had been performed for the Indian basin. The BoB is unique by its strongest monsoon on Earth, having the only openness to its south, enormous freshwater input from river and precipitation, and very warm surface water. It is essential to investigate the oceanic response to TCs in this region because it may shape a new perspective for examining the TC-climate relationship.

6.1.2 Experiment Design and Model Results

The approach to answering the research question of this study was to design and perform a suite of diagnostic experiments so that the contrasts of the experiment results could show the impacts of individual forcings of TC1 and TC2. An eddy-permitting ocean general circulation model – HYCOM – was utilized to simulate the oceanic response to the two consecutive TCs. The original forcing fields included satellite-observed CCMP winds, TRMM precipitation, and ERA-Interim reanalysis radiative flux, air temperature and humidity (Section 2.2). The TC signals in these forcing fields might be retained or filtered out before being used to drive HYCOM, and the model results were compared to analyze the effects of the individual forcings. The CCMP winds significantly underestimated the maximum wind speed associated with the TCs (Section 2.1; Fig. 2.1), so a set of TC winds were reconstructed based on the modified Rankine vortex [Holland, 1980; section 2; Fig. 2.3], NRL TC warning reports and IBTrACS for one of the experimental runs (RcWIND).

Solutions from the HYCOM RcWIND run with enhanced TC winds had strongest SSH and SST response in the BoB. In RcWIND, the strong SST reduction (~ -3°C) was mainly due to TC wind-associated turbulent mixing and upwelling and located near the Orissa seashore along the tracks and on the right; Ekman divergence near the TC centers and onshore Ekman transport also created negative SSHAs (< -18cm) along the TC tracks and positive SSHAs (> 18cm) along the BoB coast. Although both the MR and RcWIND reasonably reproduced the upper ocean thermal structure to the south of 10°N compared with cruise observations, they exhibited weaker vertical temperature gradients in the thermocline layer, possibly due to a more diffusive thermocline in the model than in the observations. RcWIND produced weaker SST in the eastern and southwestern BoB during both the TCs; the TC wind reconstruction for the beginning and end of TC2 requires information beyond the NRL TC warning report to possibly resolve the problem of

weaker SST reduction in these two regions. The RcWIND results showed that, compared to TC1 (category 4), TC2 (category 5) produced more prominent onshore Ekman convergence because of the stronger winds and longer lifetime over the ocean, but less “Bay-wide” SST reduction, likely due to the initial SST depression by TC1.

6.1.3 Processes and Interpretations

By comparing the results from RcWIND and NoTC, TC1 and TC2 combined were found to significantly reduce the total BoB OHC when they passed the BoB, reaching a peak value in early November of 1999 after TC2 over -160 x 10^{18}J, which was comparable to the BoB OHC seasonal variation from October to mid-November during the monsoon transition period when the seasonal variation is weak. The reduced OHC slowly recovered in the following months of the winter monsoon, during which the background BoB OHC was dramatically increased by the positive northward OHT. The reduced BoB OHC during the TCs resulted from both the southward OHT and reduced downward NetHF. The downward solar radiation that was reduced by the blocking of the TC clouds dominated the wind-enhanced THF during the TCs in the negative NetHF anomalies, which contributed to the BoB OHC decrease, while the TC winds caused anomalous ocean circulation that transported heat out of the Bay. The radiation effect quickly decayed in November right after the TCs. Only when the reconstructed strong winds were used to drive the model simulations could TC1 and TC2 induce enough surface cooling for enhancing post-storm downward THF to compensate the negative radiation effect during TC1 and TC2 by the end of February, 2000.

The findings about the weak upward THF enhanced by the TC winds and the SST recovery after the TCs in the area of strong mixing and upwelling were consistent with previous studies

for the Atlantic Ocean. On the other hand, the model results showed that in the BoB the reduced amount of solar radiation by TC clouds offset a major portion of the NetHF recovery after the TCs, producing a much weaker DOHP effect. In addition, the effect of TC precipitation had negligible effect of the BoB OHC. These new findings were likely associated with the unique characteristics of the BoB – strong stratification due to monsoon rainfall and large amounts of freshwater input. The strong stratification favored the formation of barrier layer and temperature inversion; therefore, when the CCMP wind in the southeastern BoB was only strong enough to entrain warmer water from the barrier layer, it warmed SST in that region. The warmer SST in the southeastern BoB counteracted the colder SST in the northwestern BoB, causing a weaker BoB-averaged downward THF during the recovery period after the TCs.

The DOHP effect induced by TC1 and TC2 in the BoB was further quantified as the post-TC oceanic heat convergence described in Sriver and Hubert [2007] and Sriver *et al.* [2008], in which the satellite-observed SST and climatological mixing depth were replaced by the simulation results. The estimates for the oceanic heat convergence in this study largely agreed with the estimates from Sriver *et al.* However, if considering the NetHF loss during the TCs, which was neglected by the previous studies, the HYCOM simulated time-integrated NetHF suggested a much weaker DOHP effect in the BoB. In addition, the upper ocean temperature in the BoB never recovered to its pre-storm values between the TCs or afterwards as hypothesized in Emanuel [2001], Sriver and Hubert [2007] and Sriver *et al.* [2008] due to the short time period between the two TCs and the cool and dry atmospheric conditions of the winter monsoon following the TCs. Because the climatological seasonal variations of SST in the western Pacific and northwestern Atlantic can be as strong as in the northern Indian Ocean, the SST recovery in the wakes of TCs in late fall was also suspected to be less than storms occurring earlier in the

season. The amount of heat mixed irreversible into the seasonal thermocline rather than the oceanic heat convergence in cold wake recovery can be a more robust indicator of DOHP. However, estimating the vertical redistribution of heat through vertical mixing may be interfered with by the immediate response of heat transport and near-surface circulation caused by TC winds.

The TC winds induced both the entrainment and the upwelling at the bottom of the ML. The entrainment exchanged the mass between the ML and deeper ocean and caused mirrored variations in OHC. In the deeper ocean below 200m, the TC wind-induced OHT variations dominated the OHC changes. Although weak below 400m, the OHT effect kept accumulating to the bottom of the BoB. The TC-associated rain facilitated a shallower ML by adding freshwater on top, while the TC-associated radiation deepened the ML because the reduced solar radiation cooled the surface and increased mixing. The TC-associated radiative flux during the TCs and winds that drove OHT variations and affected NetHF were found to be the major causes for the BoB heat potential change.

Similar to the previous works for the Atlantic and Pacific Ocean, the TC-associated wind field was the most important forcing that induced DOHP and OHT anomaly in the BoB. Compared to the previous works, the TC wind-induced DOHP effect was significantly weaker for the BoB, likely due to its strong stratification and the onset of winter after the TCs. As has been shown in the numerical study of Jansen and Ferrari [2009], the TC wind-induced OHT caused ocean heat variability on the seasonal scale. In spite of traditionally being neglected based on the findings of Price [1981] and Black [1983], the impact of TC-associated radiation on ocean surface heat budget was emphasized in this study. The solar radiation reduction due to the blocking of the TC-associated clouds induced strong SST decrease and negative NetHF anomaly,

and its effect was comparable to the TC wind. The SST was decreased by the two TC events and never recovered back to its pre-storm value between or after the TCs, while the SST restoration was a fundamental assumption in the previous research works. The effect of strong stratification on DOHP in the BoB may not apply in other ocean basins. The author, however, would argue that cautions must be used if assuming that 1) SST decrease is solely due to vertical mixing, 2) upper ocean temperature always recovers back to its pre-storm value, and 3) radiation effect is negligible, when quantifying air-sea heat exchange induced by TCs for other ocean basins. This research has shown that DOHP from the ML to the permanent thermocline did *not* occur when the SST decrease was due to TC wind-induced upwelling and/or reduced incoming solar radiation; thus, the role of TCs in the global meridional heat transport may be less than previously thought and needs further investigation.

6.1.4 Upper Ocean Dynamical Response

The SSH variations during TC1 and TC2 were primarily determined by wind stress. From mid-October to early November of 1999, the atmospheric background flow of southeasterly at the ocean surface produced large positive SSHAs along the northern and eastern BoB boundary via piling up water to the coasts as well as via Ekman transport. TC1 and TC2 produced negative SSHAs along their tracks with rightward bias via Ekman divergence and surface cooling, especially when there was longer time duration that wind stress could act on the ocean. Along the coastline of the northwestern BoB, cross-shore SSH gradients were also built and induced counter-clockwise alongshore geostrophic currents when the two TCs approached the land.

The magnitudes of SSH falling and $T_{0\text{-}30m}$ cooling by TC1 and TC2 depended on both wind stress strength and the time duration that wind stress acted on the ocean. The wind-induced

turbulent mixing and upwelling were the primary causes for $T_{0\text{-}30m}$ cooling. Due to the stronger wind stress on the right of TC1's track and moving direction change from west-northwestward to northward, a low-SSH low-$T_{0\text{-}30m}$ area formed on the right of the turning point during TC1. TC2 produced three low-SSH regions along its track. The first low-SSH area was not accompanied by obvious low $T_{0\text{-}30m}$ because of the deeper ML and weaker cyclonic winds. When TC2 traveled to the northwestern BoB, the strong winds and slow travel speed from 10/28 18Z – 10/29 00Z produced two other low-SSH regions that were accompanied by low $T_{0\text{-}30m}$. The rightward bias of the low SSH and low $T_{0\text{-}30m}$ due to the stronger wind speed on the right of the track was again simulated. While vertical mixing during the TCs homogenized the upper ocean temperature and induced DOHP, a case of strong upwelling and weak mixing in the top 100m during TC2 had shown that surface cooling may not indicate DOHP as hypothesized in some previous studies [e.g., Emanuel, 2001]. Interestingly, a small short-lived $T_{0\text{-}30m}$ warming area by vertical mixing after TC1 was discovered, whose heat source mainly came from horizontal warm advection between 60m and 120m.

Similar to previous research works, the HYCOM simulations in this study showed clear rightward-biased oceanic responses (vertical mixing, upwelling, current velocities, and SSHAs) and near-inertial oscillations (current direction rotation and upper ocean temperature oscillation). The surface currents that were associated with the near-inertial oscillations, together with the $T_{0\text{-}30m}$ distribution, had strong influence on horizontal temperature advection. The near-inertial oscillations were identified by the rotating of the currents as well as by the temporal variations of the upper ocean temperature, which had period close to the inertial oscillation (~1.5 days).

6.2 Future Work

6.2.1 Rationale

Ocean models usually lack high-quality surface meteorological fields as their driving forces to reproduce TC effects on OHC and OHT, and to provide TC models with accurate surface boundary conditions. To tackle this problem, the first step is to separately create a TC-incorporated ocean surface forcing dataset, and create a TC-affected upper ocean state dataset. These two products are in critical need for evaluating the performance of a wide range of air-sea interaction schemes and long-term climate simulations.

No basin-wide multi-year high-resolution dataset exists that contains realistic TC intensity for the investigation of TC effects on the ocean. Increasing evidence shows that without appropriate ocean surface forcing fields, the DOHP and OHT estimates can be problematic [e.g., Sriver *et al.,* 2008; Wang *et al.,* 2012b]. While remote-sensing observations, such as CCMP wind components [Atlas *et al.,* 2008], or global reanalysis data, such as ERAI reanalysis products [Simmons *et al.,* 2007; Dee *et al.,* 2011], cannot resolve details within TC effective ranges, ocean surface forcing fields from case simulations or analyses (i.e., HWIND project of NOAA Hurricane Research Division) that may be able to resolve high winds of TCs currently cannot meet the need of long-term and basin-wide coverage. Fig. 2.1 and 2.3 have already shown that one of the most important TC features – strong winds – cannot be resolved by the satellite observations (CCMP winds) or medium-resolution reanalysis data (ERAI winds). Although CCMP ocean surface wind components has global coverage at 6-hour interval and 1/4-degree resolution, it is not able to resolve the category-5 wind speed of TC2, mostly due to the measurement interference by its strong rainfall. Therefore, in order to investigate TC effects on the climate variability, we must first acquire a set of basin-wide multi-year high-resolution ocean surface forcing fields that incorporate realistic TCs.

6.2.2 Objectives

The future work may focus on the Atlantic Ocean first. The long-term goal of future work is to seek an applicable procedure to investigate the TC-induced Atlantic OHC and OHT variability and their impacts on ocean feedback to climate. The objectives are as follows:

a) To provide the ocean science community with TC-incorporated gridded ocean surface forcing data at high resolution (12-km grid spacing, 3-hour interval) for the Atlantic Ocean from 2000-2011;

b) To provide the climate science and TC community with TC-affected gridded upper ocean states at high resolution (1/8-degree grid spacing, 3-hour interval) for the Atlantic Ocean from 2000-2011;

c) To evaluate the advanced air-sea interaction scheme with sea sprays under high wind conditions in an OGCM, and to investigate the influences of fast-evolving ocean surface forcings and upper ocean states on air-sea interactions;

d) To perform sensitivity tests on multi-year (2000-2011) DOHP and meridional OHT variations that are induced by TCs in the Atlantic Ocean;

6.2.3 Research Plan

Hurricane Weather Research and Forecasting model (HWRF) will be used to *analyze* the TCs from 1998-2011. The author does *not* intend to prognostically simulate TC details. Instead, the purpose of utilizing HWRF is to acquire the ocean surface forcing fields for HYCOM simulations in order to quantify TCs' impact on DOHP and meridional OHT. Fig. 6.1 shows the flow chart for the modeling part of this research.

Phase I: Incorporating Analyzed TC Intensity and Tracks into HWRF

The domain of analysis will cover the Atlantic Ocean from 20°S to 55°N. The grid spacing will be 12km, close to the grid spacing (1/8-degree) for HYCOM simulations in Phase II. NCEP GODAS (National Centers for Environmental Prediction - Global Ocean Data Assimilation System) 5-day SST will be used as HWRF's ocean surface boundary condition in Phase I. Pressure/geopotential height from ERAI (~0.7031252º and 6-hourly) will be utilized to nudge the entire domain throughout the HWRF run to avoid drifting, except within the TC effective ranges, where the TC-associated pressure fields will be smoothly nudged toward the reconstructed pressure fields based on the data from ERAI and IBTrACS (see Holland, 1980 and 2008 for TC wind-pressure relation model). This process enables medium-resolution global reanalysis data to be combined with best independently analyzed TC track and intensity. Sensitivity tests will be performed to examine the impacts of TC pressure nudging on air temperature, humidity, radiation, rain rate and wind velocities. The output from HWRF will be evaluated against existing independent TC observations. The product in this phase includes a set of TC-incorporated meteorological fields at high resolution in space and time from 1998-2011, which will be exported to drive HYCOM.

Phase II: HYCOM Simulation under TC Conditions

HYCOM will be set up for the Atlantic Ocean from 20°S-55°N at 1/8-degree resolution, initialized with the NCEP GODAS monthly product, and "spun up" for 100 years using ERAI surface fields. After the spin-up, HYCOM will be driven by the ocean surface forcing fields from Phase I from 1998-2011. The lateral boundary in the HYCOM simulations will be relaxed

toward GODAS 5-day product throughout the HYCOM run. Note that the product of TC-incorporated ocean surface forcing fields in Phase I and TC-affected upper ocean states in Phase II will be further improved in Phase III by repetitive model simulations.

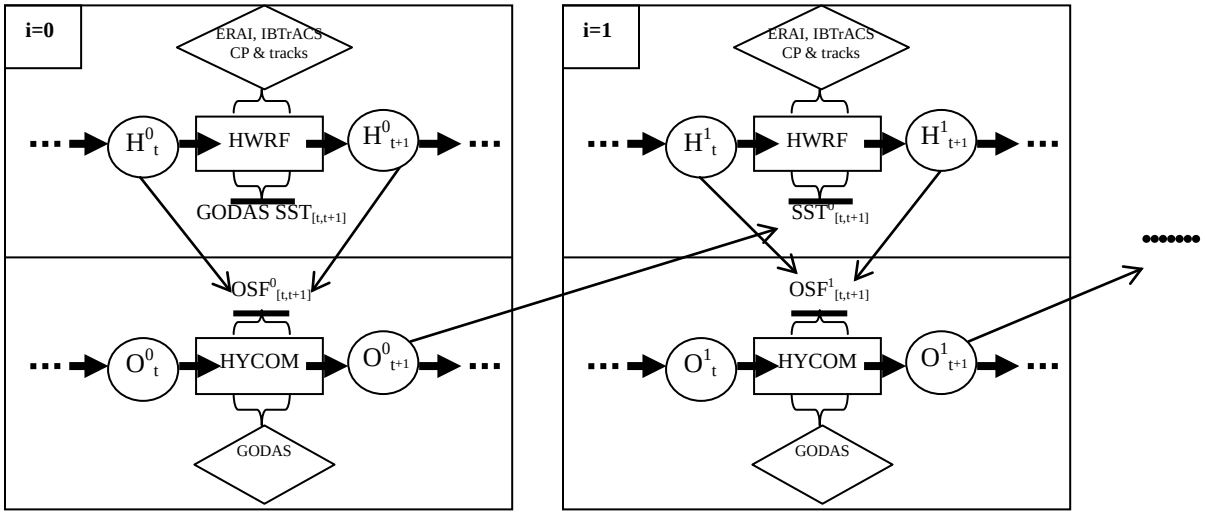

Fig. 6.1: The flow chart for producing ocean surface forcing fields for HYCOM and producing SST for HWRF. *H* represents hurricane states, *O* ocean states, *OSF* ocean surface forcing fields, and *CP* TC central pressure. The black thick arrows indicate the data stream flow, and thin long arrows show the OSF and SST extracted from *H* and *O* from one step feeding into the next. The reanalysis data and other observations in the diamonds are used to nudge the model runs.

Phase III: Process Repetition for Modeling Consistency

To produce high-resolution TC-incorporated ocean surface forcing fields and TC-affected upper ocean states, the procedure in Phase I and II will be repeated, with the SST for HWRF and the ocean surface forcing fields for HYCOM being replaced by the results from Phase II and I of the previous iteration (see Fig. 6.1). The procedure may be executed more times if the evolving SST and ocean surface forcings still alter each other to a certain prescribed threshold. The output from the first two years will be discarded for its transition state from the spin-up to the 3-hourly simulation, and the following 12 years will be archived for future uses.

Phase IV: Analysis of Model Results

The 12-year (2000-2011) HYCOM output includes hydrographic variables and velocities in the mixed layer and interior, sea surface height, and SST. The output will be compared with other reanalysis data and independent observations, especially within TC effective ranges. The relationship between the upper OHC and TC activities will be investigated. Other ocean parameters, such as mixed-layer depth, SST, salinity transport will also be analyzed to investigate the influence of TCs on both the short and long time scales. To study the influences of TCs on air-sea interactions – heat, momentum, and moisture fluxes specifically, the fluxes output from HWRF and HYCOM will be compared with each other under the conditions of fast-evolving ocean surface forcing fields and upper ocean states. The performance of the new air-sea interaction scheme in HYCOM will be evaluated.

Phase V: Study of Long-term OHT and DOHP Variability Induced by TCs

HYCOM will be run freely (without nudging in the interior) using two different sets of forcing fields – analysis output from Phase I-III (TC-incorporated gridded ocean surface forcing fields) and ERAI reanalysis data. The sensitivity tests on multi-year (2000-2011) DOHP and meridional OHT variations that are induced by TCs in the Atlantic Ocean will be performed. The long-term OHC and meridional overturning circulation variations will also be compared with other model results and used to quantify the energy budget of the Earth system.

6.2.4 Expected Outcomes and impacts

The expected outcomes include but are not limited to:

a. A TC-incorporated meteorological fields dataset and a TC-affected upper ocean states dataset for the air-sea interaction study;
b. The application of the datasets in HYCOM simulations and analyses.
c. Statistical and time series analysis of the upper OHC, SST, and other parameters and their relationship with TC intensity, frequency, and tracks.

The ocean science community will be impacted by the TC effect analysis under a TC-resolved framework. The products of OGCM forcing fields will also provide a definitive dataset for testing air-sea interaction schemes under high wind conditions.

Bibliography

Atlas, R., J. Ardizzone, R. N. Hoffman, 2008: Application of satellite surface wind data to ocean wind analysis, *Proc. SPIE*, Vol. **7087**, 70870B, doi:10.1117/12.795371.

Atlas, R., R. N. Hoffman, J. Ardizzone, S. M. Leidner, J. C. Jusem, 2009: Development of a new cross-calibrated, multi-platform (CCMP) ocean surface wind product. AMS 13th Conference on Integrated Observing and Assimilation Systems for Atmosphere, Oceans, and Land Surface (IOAS-AOLS).

Black, P. G., 1983: Ocean temperature changes induced by tropical cyclones. Ph.D. dissertation, 278 pp., Pa. State Univ., State College.

Black, P. G., E. A. D'Asaro, W. M. Drennan, J. R. French, P. P. Niller, T. B. Sanford, E. J. Terrill, E. J. Walsh, and J. A. Zhang, 2007: Air-sea exchange in hurricanes, *Bull. Am. Meteorol. Soc.*, **88**, 357– 374.

R. Bleck, 2002: An oceanic general circulation model framed in hybrid isopycnic-cartesian coordinates. *Ocean Modeling*, **4**, 55-88.

Bongirwar, V., V. Rakesh, C. M. Kishtawal, and P. C. Joshi, 2011: Impact of satellite observed microwave SST on the simulation of tropical cyclones. *Natural Hazards*, **58**(3), 929-944.

Chang, S. W., and Anthes, R. A., 1978: Numerical Simulations of Oceans Non-linear, Baroclinic Response to Translating Hurricanes. *J. Phys. Oceanogr.*, **8**(3), 468-480, DOI: 10.1175/1520-0485(1978)0080468.

Chinthalu, G. R., P. Seetaramayya, M. Ravindran, and P. N. Mahajan, 2001: Response of the Bay of Bengal to Gopalpur and Paradip Super Cyclones during 15–31 October, 1999, *Curr. Sci.*, **81**(5), 283–291.

D'Asaro, E. A., T. B. Sanford, P. P. Niiler, and E. J. Terrill, 2007: Cold wake of Hurricane Frances. *Geophys. Res. Lett.*, **34**(15), L15609, doi:10.1029/2007GL030160.

Dai, A. D., T. Qian, K. E. Trenberth, J. D. Milliman, 2009: Changes in Continental Freshwater Discharge from 1948 to 2004. *J. Climate*, **22**, 2773-2792, doi: 10.1175/2008JCLI2592.1.

Dee, D.P., with 35 co-authors., 2011: The ERA-Interim reanalysis: configuration and performance of the data assimilation system. *Quart. J. R. Meteorol. Soc.*, **137**, 553-597 (DOI: 10.1002/qj.828).

Dickey, T., *et al.*, 1998: Upper-ocean temperature response to Hurricane Felix as measured by the Bermuda testbed mooring. *Mon. Weather Rev.*, **126**, 1195-1201.

Duchon, C., 1979: Lanczos filtering in one and two dimensions. *J. Appl. Meteor.,* **18**, 1016–1022.

Duncan B. and W. Han, 2009: Indian Ocean intraseasonal SST variability during boreal summer: Madden-Julian Oscillation versus submonthly forcing and processes. *J. Geophys. Res.*, **114**, C05002, doi:10.1029/2008JC004958.

Dvorak, V.F., 1975: "Tropical cyclone intensity analysis and forecasting from satellite imagery" *Mon. Wea. Rev.*, **103**, pp.420-430

Dvorak, V.F., 1984: "Tropical cyclone intensity analysis using satellite data". *NOAA Tech. Rep. NESDIS 11*, 47pp

K. Emanuel, 2001: Contribution of tropical cyclones to meridional heat transport by the oceans. *J. Geophys. Res.*, **106**(D14), 14771-14781.

Fairall, C. W., E. F. Bradley, J. E. Hare, A. A. Grachev, and J. B. Edson, 2003: Bulk parameterization of air-sea fluxes: Updates and verification for the COARE algorithm. *J. Climate,* **16**, 571-591.

Fedorov, A. V., C. M. Brierley, K. Emanuel, 2010: Tropical cyclones and permanent El Niño in the early Pliocene epoch. *Nature,* **463**(7284), 1066-U84, doi:10.1038/nature08831.

Firing, E., R. C. Lien, and P. Muller, 1997: Observations of strong inertial oscillations after the passage of tropical cyclone Ofa. *J. Geophys. Res. - Oceans*, **102**(C2), 3317-3322, DOI: 10.1029/96JC03497.

Fritz, H. M., C. D. Blount, S. Thwin, M. K. Thu, and N, Chan, 2009: Cyclone Nargis storm surge in Myanmar. *Nature Geoscience,* **2**(7), 448-449.

Gierach, M. M., B. Subrahmanyam, and P. G. Thoppil, 2009: Physical and biological responses to Hurricane Katrina (2005) in a 1/25 degrees nested Gulf of Mexico HYCOM. *Journal of Marine Systems,* **78**(1), 168-179, DOI: 10.1016/j.jmarsys.2009.05.002.

Gopala Krishna, V. V., V. S. N. Murty, M. S. S. SARMA, and J. S. SASTRY, 1993: Thermal Response of Upper Layers of Bay of Bengal to Forcing of a Severe Cyclonic Storm: A Case Study. *Indian J. Mar. Sci.*, **22**, 8–11.

Gordon, C., C. Cooper, C. A. Senior, H. Banks, J. M. Gregory, T. C. Johns, J. F. B. Mitchell and R. A. Wood, 2000: The simulation of SST, sea ice extents and ocean heat transports in a version of the Hadley Centre coupled model without flux adjustments. *Climate Dynamics,* **16**, 147-168, doi:10.1007/s003820050010.

Gray, M., 1979, Hurricanes: their formation, structure, and likely role in the tropical circulation. In *Meteorology Over the Tropical Oceans*, D. B. Shaw (Ed.), pp. 155-218 (Bracknell: Royal Meteorological Society).

Gregg, M. C., T. B. Sanford, T. B., D. P. Winkel, 2003: Reduced mixing from the breaking of internal waves in equatorial waters. *Nature,* **422**, 513–515.

Halliwell, G.R., 1998: Simulation of North Atlantic decadal/multi-decadal winter SST anomalies driven by basin-scale atmospheric circulation anomalies. *J. Phys. Oceanogr.,* **28**, 5-21.

Halliwell, G.R., 2004: Evaluation of Vertical Coordinate and Vertical Mixing Algorithms in the HYbrid Coordinate Ocean Model (HYCOM). *Ocean Modeling,* **7**, 285-322.

Han, W., J. P. McCreary, and K.E. Kohler, 2001: Influence of P-E and Bay-of-Bengal rivers on dynamics, thermodynamics, and mixed-layer physics in the Indian Ocean. *J. Geophys. Res.*, **106**, 6895-6916.

Han, W., and P.J. Webster, 2002: Forcing Mechanisms of Sea-Level Interannual Variability in the Bay of Bengal. *J. Phys. Oceanogr.,* **32**, 216-239.

Han, W., 2005: Origins and dynamics of the 90-day and 30-60 day variations in the equatorial Indian Ocean. *J. Phys. Oceanogr.,* **35**, 708-728.

Han, W., G.A. Meehl, and A. Hu, 2006: Interpretation of tropical thermocline cooling in the Indian and Pacific Oceans during recent decades. *Geophys. Res. Lett.,* **33**, L23615, doi:10.1029/2006GL027982.

Han, W., T. Shinoda, L.-L. Fu, and J. P. McCreary, 2006: Impact of atmospheric intraseasonal oscillations on the Indian Ocean dipole during the 1990s. *J. Phys. Oceanogr.,* **36**, 670-690.

Han, W., D. Yuan, W.Timothy Liu, and D.J. Halkides, 2007: Intraseasonal variability of Indian Ocean sea surface temperatre during boreal winter: MJO versus submonthly forcing and processes. *J. Geophys. Res.,* **112**, C04001, doi:10.1029/2006JC003791.

Han W., P.J. Webster, J. Lin, W.T. Liu, R. Fu, D. Yuan and A. Hu, 2008: Dynamics of intraseasonal sea level and thermocline variability in the equatorial Atlantic during 2002-2003. *J. Phys. Oceanogr.,* **38**, 945-967.

Holland, G. J., 1980: An analytic model of the wind and pressure profiles in hurricanes. *Mon. Wea. Rev.*, **108**, 1212-1218.

Holland, G. J., 2008: A revised hurricane pressure-wind model. *Mon. Wea. Rev.*, **136**, 3432-3445.

Howden, S. D., and Murtugudde, R., 2001: Effects of river inputs into the Bay of Bengal. *J. Geophys. Res. – Oceans*, **106**(C9), 19825-19843.

Huang, P., T. B. Sanford, and J. Imberger, 2009: Heat and turbulent kinetic energy budgets for surface layer cooling induced by the passage of Hurricane Frances (2004). *J. Geophy. Res. – Oceans*, 114, Article No. C12023, doi:10.1029/2009JC005603.

Howden, S. D., and Murtugudde, R., 2001: Effects of river inputs into the Bay of Bengal. *J. Geophys. Res. – Oceans*, **106**(C9), 19825-19843.

Hu A. and G.A. Meehl, 2009: Effect of the Atlantic hurricanes on the oceanic meridional overturning circulation and heat transport, *Geophys. Res. Letts.*, **36**, L03702, doi:10.1029/2008GL036680.

Huang, P. S., T. B. Sanford, and J. Imberger, 2009: Heat and turbulent kinetic energy budgets for surface layer cooling induced by the passage of Hurricane Frances (2004). *J. Geophys. Res. – Oceans*, **114**, C12023, doi:10.1029/2009JC005603.

Ingleby, B., and M. Huddleston, 2007: Quality control of ocean temperature and salinity profiles - historical and real-time data. *Journal of Marine Systems*, **65**, 158-175 10.1016/j.jmarsys.2005.11.019

International Federation of Red Cross and Red Crescent Societies, 2001: Situation Report - India: Orissa Cyclone. Appeal no. 28/99, Situation report no. 17.

Isaac M. Held, 2001: The partitioning of the Poleward Energy Transport between the Tropical Ocean and Atmosphere. *J. Atmos. Sci.*, **58**, 943-948.

Jacob, S. D., L. K. Shay, A. J. Mariano, and P. G. Black, 2000: The 3D oceanic mixed layer response to Hurricane Gilbert. *J. Phys. Oceanogr.*, **30**(6), 1407-1429.

Jaimes, B., and Shay, L. K., 2010: Near-Inertial Wave Wake of Hurricanes Katrina and Rita over Mesoscale Oceanic Eddies. *J. Phys. Oceanogr.*, **40**(6), 1320-1337, DOI: 10.1175/2010JPO4309.1.

Jansen, M. F., and R. Ferrari, 2009: Impact of the latitudinal distribution of tropical cyclones on ocean heat transport. *Geophys. Res. Lett.*, **36**, L06604, doi:10.1029/2008GL036796.

Jansen, M. F., R. Ferrari, and T. A. Mooring, 2010: Seasonal versus permanent thermocline warming by tropical cyclones. *Geophys. Res. Lett.*, **37**, L03602, doi:10.1029/2009GL041808.

Kalnay, E., M. Kanamitsu, R. Kistler, W. Collins, D. Deaven, L. Gandin, M. Iredell, S. Saha, G. White, J. Woollen, Y. Zhu, M. Chelliah, W. Ebisuzaki, W. Higgins, J. Janowiak, K. C. Mo, C. Ropelewski, J. Wang, A. Leetmaa, R. Reynolds, R. Jenne, and D. Joseph, 1996: The NMC/NCAR 40-Year Reanalysis Project". *Bull. Amer. Meteor. Soc.*, **77**, 437-471.

Kara, A. B., A. J. Wallcraft, and H. E. Hurlburt, 2005: A new solar radiation penetration scheme for use in ocean mixed layer studies: An application to the Black Sea using a fine-resolution Hybrid Coordinate Ocean Model (HYCOM). *J. Phys. Oceanogr.*, **35**(1), 13-32.

-, 2005: Sea surface temperature sensitivity to water turbidity from simulations of turbid Black Sea using HYCOM. *J. Phys. Oceanogr.*, **35**, 33-54.

Kikuchi, K., B. Wang, and H. Fudeyasu, 2009: Genesis of tropical cyclone Nargis revealed by multiple satellite observations. *Geophys. Res. Lett.*, **36**, L06811, doi:10.1029/2009GL037296.

Kummerow, C., Barnes, W., T. Kozu, J. Shiue, and J. Simpson, 1998: The tropical rainfall measuring mission (TRMM) sensor package, *J. Atmos. Oceanic Technol.*, **15**, 809-817.

Kummerow C., J. Simpson, O. Thiele, W. Barnes, A. T. C. Chang, et al., 2000: The status of the Tropical Rainfall Measuring Mission (TRMM) after two years in orbit. *J. Appl. Meteor.*, **39**(12), 1965-1982.

Jacob, S. D., L. K. Shay, A. J. Mariano, and P. G. Black, 2000: The 3D oceanic mixed layer response to Hurricane Gilbert. *J. Phys. Oceanogr.*, **30**(6), 1407-1429.

Jacob, S. D. and Shay L. K., 2003: The role of oceanic mesoscale features on the tropical cyclone-induced mixed layer response: A case study. *J. Phys. Oceanogr.*, **33**(4), 649-676.

Jiang, X., Z. Zhong, and J. Jiang, 2009: Upper ocean response of the South China Sea to Typhoon Krovanh (2003). *Dynamics of Atmospheres and Oceans*, **47**(1-3), 165-175.

Kikuchi, K., B. Wang, and H. Fudeyasu, 2009: Genesis of tropical cyclone Nargis revealed by multiple satellite observations. *Geophys. Res. Lett.*, **36**, L06811, doi:10.1029/2009GL037296.

Large, W. G., and S. Pond, 1981: Open Ocean Momentum Flux Measurements in Moderate to Strong Winds. *J. Phys. Oceanogr.*, **11**, 324-336.

Large, W. G., J. C. McWilliams, and S. C. Doney, 1994: Ocean vertical mixing: A review and a model with a nonlocal boundary layer parameterization. *Rev. Geophys.*, **32**, 363-403.

Large, W. G., G. Danabasoglu, S. C. Doney, J. C. McWilliams, 1997: Sensitivity to surface forcing and boundary layer mixing in a global ocean model: Annual-mean climatology. *J. Phys. Oceanogr.*, **27**, 2418-2447.

G. Latha and E. P. Rama Rao, 2007: Surge simulations for 1999 Orissa super cyclone using a finite element model. *Natural Hazards*, **40**, 615-625, doi:10.1007/s11069-006-9012-2.

Ledwell, J. R., A. J. Watson and C. S. Law, 1993: Evidence for slow mixing across the pycnocline from an open-ocean tracer-release experiment. *Nature*, **364**, 701–703.

Lee, T., and J. Marotzke (1998), Seasonal cycles of meridional overturning and heat transport of the Indian Ocean, *J. Phys. Oceanogr.*, **28**, 923– 943.

I-I Lin, Chi-Hong Chen, Iam-Fei Pun, W. Timothy Liu, and Chun-Chieh Wu, 2009: Warm Ocean Anomaly, Air Sea Fluxes, and the Rapid Intensification of Tropical Cyclone Nargis (2008), *Geophys. Res. Lett.*, **36**, L03817, doi: 10.1029/2008GL035815.

Lukas, R. and Lindstrom, E., 1991: The mixed layer of the western equatorial Pacific Ocean. *J. Geophys. Res. – Oceans,* **96**, 3343-3357.

Alison M. Macdonald and Carl Wunsch, 1996: An estimate of global ocean circulation and heat fluxes. *Nature*, **382**, 436-439.

Mahapatra, D. K., A. D. Rao, S. V. Babu, and C. Srinivas, 2007: Influence of coast line on upper ocean's response to the tropical cyclone. *Geophys. Res. Lett.,* **34**(17), L17603, doi:10.1029/2007GL030410.

Mandal, M., U. C. Mohanty, P. Sinha, M. M. Ali, 2007: Impact of sea surface temperature in modulating movement and intensity of tropical cyclones. *Natural Hazards,* **41**(3), 413-427.

Manucharyan, G. E., C. M. Brierley, and A. V. Fedorov, 2011: Climate impacts of intermittent upper ocean mixing induced by tropical cyclones. *J. Geophys. Res. – Oceans,* **116**, C11038, doi:10.1029/2011JC007295.

Masson, S., P. Delecluse, J. P. Boulanger, and C. Menkes, 2002: A model study of the seasonal variability and formation mechanisms of the barrier layer in the eastern equatorial Indian Ocean. *J. Geophys. Res. – Oceans,* **107**(C12), 8017, doi:10.1029/2001JC000832.

Meehl, G. A., W. M. Washington, W. D. Collins, J. M. Arblaster, A. Hu, L. E. Buja, W. G. Strand, and H. Teng, 2005: How Much More Global Warming and Sea Level Rise? *Science,* **307**, 1769, doi:10.1126/science.1106663.

Meehl, G. A., J. M. Arblaster, J. T. Fasullo, A. Hu, and K. E. Trenberth, 2011: Model-based evidence of deep-ocean heat uptake during surface-temperature hiatus periods. *Nature Climate Change,* **1**, 360-364, doi:10.1038/nclimate1229.

Murty, V. S. N., Y. V. B. Sarma and D. P. Rao, 1996: Variability of the Oceanic Boundary Layer Characteristics in the Northern Bay of Bengal during MONTBLEX-90, *Proc. Indian Acad. Sci. (Earth Planet. Sci.),* **105**, 41–61.

NOAA, 1979: Meteorlolgical criteria for standard project hurricane and probable maximum hurricane wind fields, Gulf of Mexico and east coast of the United States. NOAA Tech. Rep. NWS 23, Washington DC, 320 pp.

Oey, L. Y., T. Ezer, D. P. Wang, X. Q. Yin, and S.-J. Fan, 2007: Hurricane-induced motions and interaction with ocean currents. *Continental Shelf Research,* **27**(9), 1249-1263.

Powell, M. D., P. J. Vickery, and T. A. Reinhold, 2003: Reduced drag coefficient for high wind speeds in tropical cyclones. *Nature*, Vol. **422**, 279-283.

Prasad, T. G., and P. J. Hogan, 2007: Upper-ocean response to Hurricane Ivan in a 1/25 degrees nested Gulf of Mexico HYCOM. *J. Geophys. Res. – Oceans,* **112**(C4), C04013, doi:10.1029/2006JC003695.

J. F. Price, 1981: Upper Ocean Response to a Hurricane. *J. Phys. Oceanogr.,* **11**, 153-175.

Price, J. F., T. B. Sanford, and G. Z. Forristall, 1994: Forced Stage Response to A Moving Hurricane. *J. Phys. Oceanogr.*, **24**(2), 233-260, DOI: 10.1175/1520-0485(1994)0240233.

Rao, R. R., M. S. G. Kumar, M. Ravichandran, B. K. Samala, and N. Sreedevi, 2006: Observed mini-cold pool off the southern tip of India and its intrusion into the south central Bay of Bengal during summer monsoon season. *Geophys. Res. Lett.,* **33**(6), L06607, doi:10.1029/2005GL025382.

Rao, R. R., M. S. G. Kumar, M. Ravichandran, B. K. Samala, and G. Anitha, 2006: Observed intraseasonal variability of mini-cold pool off the southern tip of India and its intrusion into the south central Bay of Bengal during summer monsoon season. *Geophys. Res. Lett.,* **33**(15), L15606, doi:10.1029/2006GL026086.

Sanford, T. B., J. F. Price, J. B. Girton, and D. C. Webb, 2007: Highly resolved observations and simulations of the ocean response to a hurricane. *Geophys. Res. Lett.,* **34**(13), L13604, doi:10.1029/2007GL029679.

Sanford, T. B, J. F. Price, J. B. Girton, 2011: Upper-Ocean Response to Hurricane Frances (2004) Observed by Profiling EM-APEX Floats. *J. Phys. Oceanogr.*, **41**(6), 1041-1056, DOI: 10.1175/2010JPO4313.1.

Sengupta, D., B. Goddalehundi, and D. S. Anitha, 2008: Cyclone-induced mixing does not cool SST in the post-monsoon north Bay of Bengal. *Atmospheric Science Letters,* **9**(1), 1-6.

Shaji, C., C. Wang, G. R. Halliwell, and A. Wallcraft, 2005: Simulation of tropical Pacific and Atlantic Oceans using a hybrid coordinate ocean model. *Ocean modeling*, **9**(3), 253-282.

Shay, L. K., S. W. Chang, and R. L. Elsberry, 1990: Free-surface effects on the near-inertial ocean current response to a hurricane. *J. Phys. Oceanogr.,* **20**(9), 1405-1424, DOI: 10.1175/1520-0485(1990)0201405

Shay, L. K., et al., 1992: Upper Ocean Response to Hurricane Gilbert. *J. Geophys. Res. – Oceans*, **97**(C12), 20227-20248, DOI: 10.1029/92JC01586.

Shay, L. K., and Uhlhorn, E. W., 2008: Loop current response to Hurricanes Isidore and Lili. *Mon. Weather Rev.*, **136**(9), 3248-3274, DOI: 10.1175/2007MWR2169.1.

Shetye, S. R., et al., 1996: Hydrography and circulation in the western Bay of Bengal during the northeast monsoon. *J. Geophys. Res. – Oceans,* **101**(C6), 14011-14025.

Shi, W. and Wang M., 2008: Three-dimensional observations from MODIS and CALIPSO for ocean responses to cyclone Nargis in the Gulf of Martaban. *Geophys. Res. Lett.*, **35**(21), L21603, doi:10.1029/2008GL035279.

Simmons, A, S. Uppala, D. Dee, and S. Kobayashi, 2007: *ERA-Interim: New ECMWF reanalysis products from 1989 onwards.* Newsletter 110 - Winter 2006/07, ECMWF, 11 pp.

Siswanto, E., J. Ishizaka, A. Morimoto, K. Tanaka, K. Okamura, A. Kristijono, and T. Saino, 2008: Ocean physical and biogeochemical responses to the passage of Typhoon Meari in the East China Sea observed from Argo float and multiplatform satellites. *Geophys. Res. Lett.*, **35**(15), L15604, doi:10.1029/2008GL035040.

Sprintall, J. and M. Tomczak, 1992: Evidence of the barrier layer in the surface-layer of the tropics. *J. Geophys. Res. – Oceans,* **97**(C5), 7305-7316.f

Sriver, R.L. and M. Huber, 2007: Observational evidence for an ocean heat pump induced by tropical cyclones. *Nature*, **447**, doi:10.1038/nature05785, 577-580.

Sriver, R. L., M. Huber, and J. Nusbaumer, 2008: Investigating tropical cyclone-climate feedbacks using the TRMM Microwave Imagerand the Quick Scatterometer. *Geochemistry Geophysics Geosystems,* **9**, Q09V11, doi:10.1029/2007GC001842.

- , 2010: Modeled sensitivity of upper thermocline properties to tropical cyclone winds and possible feedbacks on the Hadley circulation. *Geophys. Res. Lett.*, **37**, Article No. L08704, doi:10.1029/2010GL042836.

Sriver, R. L., M. Goes, M. E. Mann, K. Keller, 2010: Climate response to tropical cyclone-induced ocean mixing in an Earth system model of intermediate complexity. *J. Geophys. Res*. – Oceans, **115**, Article No. C10042, doi:10.1029/2010JC006106.

Subrahmanyam, B., V. S. N. Murty, R. J. Sharp, and J. J. O'Brien, 2005: Air-sea Coupling During the Tropical Cyclones in the Indian Ocean: A Case Study Using Satellite Observations. *Pure Appl. Geophys.*, **162**, 1643-1672.

K. E. Trenberth and J. M. Caron, 2001: Estimates of Meridional Atmosphere and Ocean Heat Transports. *J. Climate*, **14**, 3433-3443.

Tsai, Y. L., C. S. Chern, and J. Wang, 2008: The upper ocean response to a moving typhoon. *J. Phys. Oceanogr.*, **64**(1), 115-130, DOI: 10.1007/s10872-008-0009-1.

Tseng, Y. H., S. Jan, D. E. Dietrich, I.-I. Lin, Y. T. Chang, and T. Y. Tang, 2010: Modeled Oceanic Response and Sea Surface Cooling to Typhoon Kai-Tak. *Terrestrial Atmospheric and Oceanic Sciences*, **21**(1), Special Issue, 85-98, doi:10.3319/TAO.2009.06.08.02.

U.S. Navy 1999 Annual Tropical Cyclone Report, U.S. Naval Pacific Meteorology and

Oceanography Center/Joint Typhoon Warning Center, Pearl Harbor, Hawaii. http://www.usno.navy.mil/NOOC/nmfc-ph/RSS/jtwc/atcr/1999atcr.pdf

Vinaychandran, P. N., V. S. N. Murty, and V. RAMESH BABU, 2002: Observations of Barrier Layer Formation in the Bay of Bengal during Southwest Monsoon, *J. Geophys. Res.*, **107**, 8018, doi:10.1029/ 2001JC000831. SRF 19-1 to SRF 19-9.

Wacongne, S. and R. C. Pacanowski, 1996: Seasonal heat transport in a primitive equation model of the tropical Indian Ocean, *J. Phys. Oceanogr.*, **26**, 2666–2699.

Wada, A., H. Nino, and H. Nakano, 2009: Roles of Vertical Turbulent Mixing in the Ocean Response to Typhoon Rex (1998). *J. Oceanogr,* **65**, 373-396.

Wang, J.-W., W. Han, and R. L. Sriver, 2012: Impact of Tropical Cyclones on the Ocean Heat Budget in the Bay of Bengal during 1999. Part I: Model Configuration and Evaluation. *J. Geophys. Res. – Oceans, in press*

Wang, J.-W., W. Han, and R. L. Sriver, 2012: Impact of Tropical Cyclones on the Ocean Heat Budget in the Bay of Bengal during 1999. Part II: Processes and Interpretations. *J. Geophys. Res. – Oceans, in press*

Webster, P. J., C. Clark, G. Chirokova, J. Fasullo, W. Han, J. Loschnigg, and K. Sahami, 2002: The monsoon as a self-regulating coupled ocean-atmosphere system. *Meteorology at the Millenium*, Eds., R. Pierce, Academic press, 198-219, 333 pp.

Webster, P. J., 2008: Myanmar's deadly daffodil. *Nature Geoscience*, 1(8), 488-490, doi:10.1038/ngeo257.

Yin, X, Z. Wang, Y. G. Liu, Y. Xu, 2007: Ocean response to Typhoon Ketsana traveling over Northwest Pacific and a numerical model approach. *Geophys. Res. Lett.,* **34**(21), L21606, doi:10.1029/2007GL031477.

Yu, L., and McPhaden, M. J., 2011: Ocean Preconditioning of Cyclone Nargis in the Bay of Bengal: Interaction between Rossby Waves, Surface Fresh Waters, and Sea Surface Temperatures. *J. Phys. Oceanogr.,* **41**(9), 1741-1755.

Yuan, D., W. Han, and D. Hu, 2006: Surface Kuroshio path in the Luzon Strait area derived from satellite remote sensing data. *J. Geophys. Res. – Oceans,* **111**, C11007, doi:10.1029/2005JC003412.

Zhang, Y., W. B. Rossow, A. A. Lacis, V. Oinas, and M. I. Mishchenko, 2004: Calculation of radiative fluxes from the surface to top of atmosphere based on ISCCP and other global data sets: Refinements of the radiative transfer model and the input data, *J. Geophys. Res.*, **109**, D19105, doi:10.1029/2003JD004457.

Zedler, S. E. et al., 2002: Analyses and simulations of the upper ocean's response to Hurricane

Felix at the Bermuda Testbed Mooring site: 13-23 August 1995. *J. Geophys. Res. – Oceans*, **107**(C12), 3232, doi:10.1029/2001JC000969.

Sarah E. Zedler, 2009: Simulations of the Ocean Response to a Hurricane Nonlinear Processes. *J. Phys. Oceanogr.*, **39**, 2618-2634, doi:10.1175/2009JPO4062.1.

Zheng, Z., C. Ho, Q. Zheng, Y. Lo, N. Kuo, and G. Gopalakrishnan, 2010: Effects of preexisting cyclonic eddies on upper ocean responses to Category 5 typhoons in the western North Pacific. *J. Geophys. Res. – Oceans*, **115**, C09013, doi:10.1029/2009JC005562.